COMPUTER-ASSISTED FEMORAL AUGMENTATION FOR OSTEOPOROTIC HIP FRACTURE PREVENTION

by

Ehsan Basafa

A dissertation submitted to The Johns Hopkins University in conformity with the requirements for the degree of Doctor of Philosophy.

Baltimore, Maryland

October, 2013

Abstract

Osteoporosis is the severe reduction in bone mineral density and load bearing capabilities. Individuals with osteoporosis, especially the elderly, are at a higher risk of bone fracture as a result of trauma, with hip fractures being the most prevalent and life threatening. There are currently a number of preventive treatments available; however the side effects, long delays in restoring bone strength or other issues associated with these treatments inhibit their efficacy. A promising new approach to preventing fracture is augmentation of the mechanical properties of the femur by injecting it with acrylic bone cement—femoroplasty. There are risks and limitations associated with femoroplasty, however, that need to be addressed through pre-operative planning and careful execution as well as experimental validation before it finds its way to the operating room. This thesis describes the methods and tools developed for effectively planning and performing femoroplasty. To this end, computational models were developed to simulate various augmentation scenarios and to predict how those affect the mechanical strength of the femur. Those tools were then used to plan femoroplasty for paired cadaveric osteoporotic femur specimens. Experimental tests

ABSTRACT

performed on those specimens showed significant improvements in the load and energy absorbed to fracture the augmented specimens compared to those left intact. We therefore conclude that effective femoroplasty is possible by using computer planning and controlled execution. Although geared towards femoroplasty, these methods and tools can be extended to other types of augmentation surgeries using bone cement including vertebral body augmentation (vertebroplasty) or augmentation of distal radius for prevention of osteoporotic wrist fractures.

Advisor: Mehran Armand, PhD

Principal Research Staff of Johns Hopkins Applied Physics Laboratory

Johns Hopkins University

Readers: Russell H. Taylor, PhD

Professor of Computer Science

Johns Hopkins University

James K. Guest, PhD

Associate Professor of Civil Engineering

Johns Hopkins University

Acknowledgments

First and foremost, I'd like to express my gratitude to Dr. Mehran Armand, my advisor and mentor throughout my journey of graduate school. It was for him that I had the opportunity to work among some of the most brilliant minds around and experience a unique environment of research in the area of computer-assisted surgery. He has been very enthusiastic and supportive of my research and I'm privileged to have worked in his group.

Many thanks also go to Dr. Russell Taylor of Computer Science and Dr. James Guest of Civil Engineering at Johns Hopkins University from whom I learned a lot, either via classes, qualification exams or personal communications, and who helped enhance my research and presentation skills. They have also graciously taken the time to read this dissertation and be on my defense committee.

Only one name appears on the title of this writing, but it wouldn't have been possible without close collaboration with many other people. Among this endless list are Robert Armiger, Ryan Murphy and Dr. Michael Kutzer of Johns Hopkins University Applied Physics Laboratory and Dr. Yoshito Otake of Computer Science,

who carried along many aspects of this project including hardware design and control software and provided me with help and invaluable feedback. I'd also like to thank Dr. Stephen Belkoff, Dr. Simon Mears, Evan Langdale and Demetries Boston of Johns Hopkins Bayview Medical Center. They were extremely helpful by providing feedback for my work and helping me run the experiments.

Mike Bernard of Mechanical Engineering deserves many thanks for taking care of the substantial load of administrative work, especially during my transition to the United States. So do Alison Morrow and Jamie Meehan of the Laboratory for Computational Sensing and Robotics.

I also like to thank the many wonderful friends I met during my stay in Baltimore and whose names will span many pages. I truly enjoyed their company and support.

Last but absolutely not the least, I thank my wonderful family for their unconditional love and support. Nothing I have accomplished in life would be possible without them.

Dedication

For two real-life superheroes, Ali and Behjat ...

Contents

List of Tables

List of Figures

Chapter 1

Introduction

1.1 Motivation

Hip fractures in the elderly with osteoporosis, mainly due to falls to their side on the greater trochanter, constitute a major health problem worldwide. Solely in the United States, they are responsible for $20 billion of annual hospitalization and treatment costs [1, 2]. Current preventive treatments include hip protectors, special diets and drugs and bone strengthening exercises [2,3]. But the side effects, long delay in restoring bone strength, or other issues associated with these treatments inhibit their efficacy. Femoroplasty—augmentation of bone mechanical properties by use of polymethylmethacrylate (PMMA) bone cement injection inside proximal femur—has been proposed as an effective alternative near-term measure [2–4]. The procedure, however, is not part of clinical practice because of its unknown complications. Injec-

tion of a large amount of cement, which has an exothermic curing process, can lead to osteonecrosis i.e. death of bone tissue as a result of poor blood supply [4, 5]. Also suboptimal injection can result in bone weakening or stress concentration and render the augmentation unsuccessful [5]. Therefore the operation requires detailed planning and careful execution. Unlike its counterpart procedure for treating osteoporotic vertebral bodies (vertebroplasty) [6–10], and despite its importance, optimization of bone cement placement in femoroplasty has received minimal attention in the literature. In most of the reported experimental studies of femoral augmentation, significant increases in the fracture loads and energies have been achieved [2–4]. However, gross fillings of femoral neck and trochanter were used in those studies, resulting in a significant increase of bone surface temperature [3]. In those studies where the cement volume was limited the augmentation was partially successful or not successful at all [5, 11–13]. Femoroplasty can largely benefit from computer planning and controlled execution. An effective biomechanical planning strategy has the potential to provide an immediate benefit to patients at the highest risk for hip fracture.

1.2 Objectives and Scope

The goal of the research discussed in this document can be summarized as an attempt in finding the answer to the question "Can the outcome of femoroplasty be improved through computer-assisted planning and execution?" In this work we aim

to develop a framework for pre-operative planning and post-operative assessment of femoroplasty. To this end, the first aim is to develop a computational model for biomechanical analysis of femoroplasty and its effect on mechanical properties of osteoporotic bones. The next aim is to develop a model for prediction of cement diffusion inside osteoporotic trabecular bone. This work then integrates these models, with the addition of optimization techniques and taking into consideration the intra-operative limitations of the surgery, to plan the femoral augmentation. The final objective is to evaluate, through biomechanical tests, the effect of augmentation and compare the experimental results with those planned pre-operatively.

1.3 Thesis Overview

Chapter 2 provides a brief background about osteoporosis and hip fractures and the current clinical routines to prevent those fractures, including femoroplasty and its current shortcomings. It then provides an overview of the framework developed in this work.

Chapter 3 describes development and validation of a finite element (FE) modeling scheme that is used to evaluate the biomechanics of femora and the effect of femoroplasty on mechanical properties of femur bone.

Chapter 4 introduces an evolutionary algorithm, built upon the FE model, that is employed to optimize the distribution of cement inside the femur in order to achieve

the desired femoroplasty outcome.

Chapter 5 is dedicated to describing a particle-based method for modeling the diffusion of viscous bone cement inside the porous medium of cancellous bone.

Chapter 6 details the planning approach we took for femoroplasty, which combines the FE, optimization and cement diffusion prediction methods described in the previous chapters.

Chapter 7 continues to describing the augmentation and mechanical tests that were performed on cadaveric femur specimens, based on pre-operative plans, and lays out the results that were obtained from those experiments.

Chapter 8 offers a summary and conclusion of this work as well as some limitations and future areas of research.

1.4 Contributions

The author's contributions in the presented work include:

- Development of an FE modeling module for patient-specific model generation of femora based on CT scans and validation of the module based on previously acquired experimental data. The modeling scheme could capture the experimental results and predict the stiffness and yield of osteoporotic femora, either intact or augmented with cement, with good accuracy.

- Implementation of an evolutionary algorithm to optimize the cement pattern in-

side osteoporotic femur models that were created using the FE modeling scheme. Results of these optimizations provide insight on the locations inside the femur that are most vulnerable to failure when loaded and the amount of cement needed to augment those regions.

- Development of a particle-based computational model to simulate the bone cement diffusion inside osteoporotic cancellous bone and to predict the assumed end shape of the cement under various viscosity levels. Simulation results showed close agreement with those of experimental tests that involved controlled cement injections.

- Combining the evolutionary optimization results and particle simulations, while taking into account the surgical limitations, to provide specimen-specific plans of femoral augmentation.

- Performing of augmentation tests, based on pre-operative plans, on cadaveric osteoporotic femora and evaluation of the results. The augmentations were successful in restoring the deteriorated mechanical properties of femora by injecting minimal, and hence safe, amounts of cement inside the bones.

Chapter 2

Background

2.1 Osteoporosis and Hip Fracture

Osteoporosis is a condition associated with low bone mineral density (BMD) and deterioration of bone microarchitecture. Hip fractures are the most debilitating problems in individuals with osteoporosis. With the ever increasing life expectancy of the world population, osteoporotic hip fractures are becoming more and more challenging. The rate of mortality after osteoporotic hip fracture in patients is reported to be as high as 20% within one year [14]. It has been shown that women with osteoporosis have a 15 fold increase in the risk of hip fracture [15]. It is estimated that 35% of women older than 65 years of age have osteoporosis; additionally, as many as 50% of women have some degree of low bone density in the hip. There is also a risk, although lower, for men to sustain osteoporotic fractures [16]. Previous hip fracture is a signif-

icant risk factor for subsequent hip fracture—contralateral hip fracture occurs 6-10 times more frequently in patients who have already suffered an osteoporotic hip fracture [17, 18]. Osteoporotic fractures result in more than 300,000 hospital admissions per year [19]. The World Health Organization (WHO) defines osteoporosis as a BMD of 2.5 standard deviations or more below that of average of young, healthy adults (T-score of -2.5 or less), determined by scanning the bone using Dual-Energy X-ray Absorptiometry (DEXA) [20]. Figure 2.1 compares representative cross sections of healthy and osteoporotic femur bone samples. One can notice the loss in the bone tissue volume in the neck and trochanter of the osteoporotic specimen as well as the reduced thickness of the cortical shell.

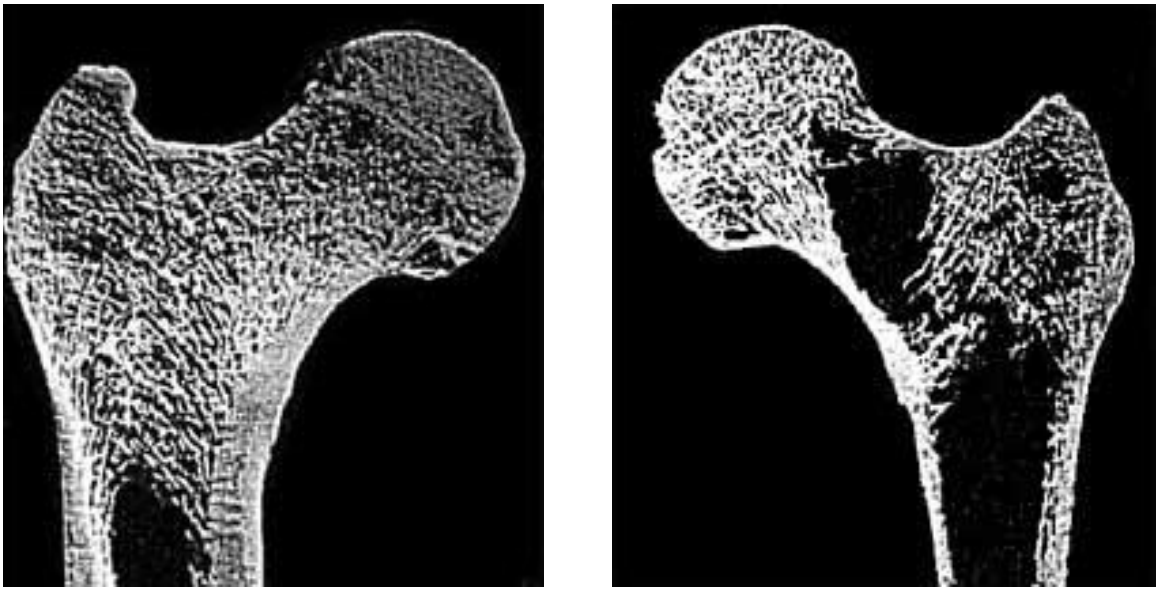

Figure 2.1: Healthy (left) vs. osteoporotic (right) femur. The loss of bone density is evident in the neck and trochanter of the osteoporotic femur. Images from `http://www.osteoporosis-surgery.com/english/osteo_evidence.htm`.

2.2 Fracture Mechanics and Risk Assessment

Femur fracture is a complicated phenomenon and depends on a number of parameters. These include bone geometry, loading conditions and the degree of bone loss as a result of osteoporosis. The mid section of the long femur bone has a relatively simple geometry and is essentially a thick-wall tube, best adapted to carry large bending loads while having a small structural mass [21]. The proximal femur, however, is more complex and carries a variety of loads during everyday activities. A number of muscles exert forces on the femur at various attachment points. A substantial amount of body weight load also gets transferred to the femur through its connection to the acetabulum in the pelvis. A healthy bone adapts its structural density to best carry the loads while keeping its weight at a minimum—a phenomenon called bone remodeling [21]. With osteoporosis, bone loses its density severely and is unable to withstand the loads by remodeling. Severe osteoporosis can cause some bones, e.g. vertebral segments, to sustain fracture even during normal daily activities such as standing up [22]. Femur fracture, on the other hand, usually happens as a result of trauma, such as falling backwards or to the side on the greater trochanter [22]. Fracture patterns and locations in proximal femur vary for different specimens or patients, depending on the parameters mentioned above, and can be categorized as head and neck (subcapital or transcervical), intertrochateric, and subtrochantric fractures [23].

Figure 2.2 illustrates the different types of hip fractures. All types of the illustrated fractures can happen as a result of a fall to the side, with the head and neck and intertrochanteric fractures being the most prevalent. Fixation methods depend on the type of fracture and include fixation by hip screws or total hip replacement, where the acetabular cup and the femoral head are replaced by prostheses.[1]

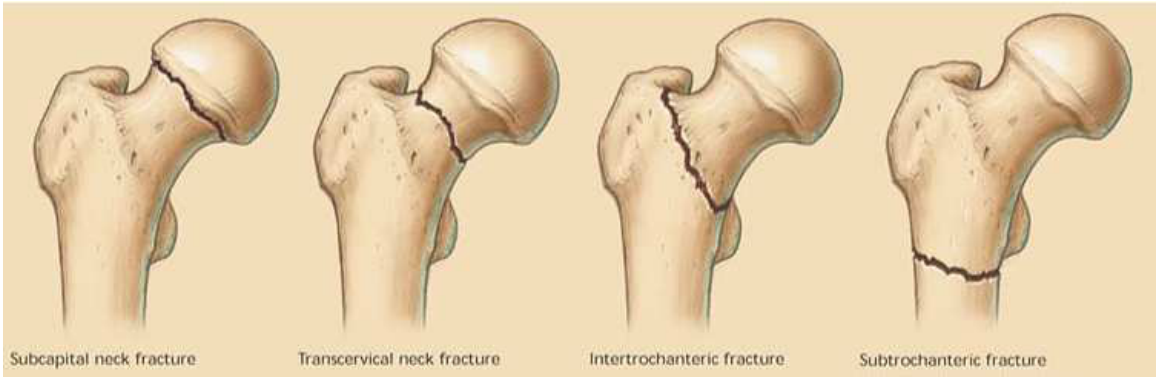

Figure 2.2: Various types of femur fracture. Images from `http://www.aafp.org/afp/2003/0201/p537.html`.

Even under controlled loading conditions, various fracture patterns are observed, mainly due to variability among femur samples [2–5]. One must note, however, that the complete fracture of the bone occurs after a local region of the trabecular bone fails which in turn results in a crack initiating at the cortex and then propagating along the line of fracture. There have been attempts at locating the site of first failure on the surface of the femur under controlled loading conditions, using high speed videography. Dragomir-Daescu et al. [24] and de Bakker et al. [25] concluded that,

[1] An instructive video describing patterns of hip fracture and possible repair treatments can be found at `http://www.youtube.com/watch?v=6wok5JGEpTQ`

under loading conditions simulating fall to the side, superior aspect of the neck cortex yields in compression first and that propagates through and over to the inferior aspect, where a tensile fracture completes the failure. Although it is understood that the dense cortical bone is a brittle material, stronger in compression than tension, initial compressive yielding of the superior cortex has been related to the reduced thickness of the cortical shell in the superior aspect, compared to the inferior aspect [25]. This reduction in thickness is more prominent in the elderly and osteoporotic patients and that makes them more vulnerable to hip fractures due to falls to the side [25].

Few factors determine bone "quality" in the context of strength against applied loads. Fracture tests using loading machines usually result in a load-displacement curve that shows an initially linear increase in the load until the first point of yielding, followed by a plateau until final fracture, which is evident as a sharp drop in the load. From these curves one can measure the yield load (first inflection point or point of deviation from linear behavior), maximum load, and the corresponding areas under the curve that represent the absorbed energies. The slope of the linear portion of the curve is also defined as bone stiffness. Figure 2.3 shows a typical such load-displacement curve. With aging and osteoporosis both the strength and energy absorbing capability of the femur deteriorate drastically.

Risk of fracture can roughly be defined as the probability of sustaining a fracture during daily activities. As the risk is dependent on a number of parameters including bone strength, age, precedence of a previous fracture and probability of trauma, there

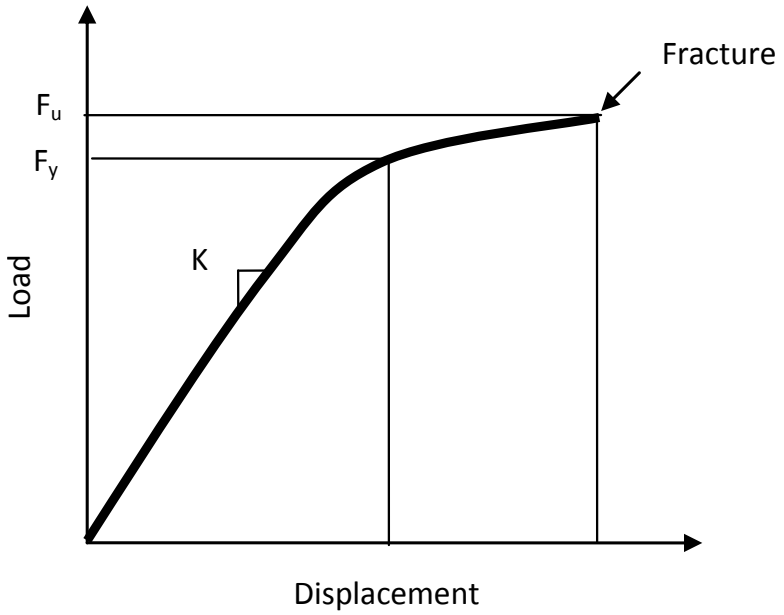

Figure 2.3: Typical load-displacement curve of a femur fracture. F_y and F_u denote yield and ultimate fracture loads, respectively, and K represents stiffness.

is still no standard way of quantifying it. Some studies have found BMD (determined from 2D DEXA scans) or quantitative CT (QCT) values to be moderately powerful in predicting the strength or energy absorption capability of the femur for certain loading conditions [4, 12, 26]. But, as mentioned, strength only partially determines the risk of fracture. Furthermore, to predict the outcome of treatments involving introduction of augmenting material inside the bone (e.g. femoroplasty—see Section 2.4), standard density measures fail because the effect of the out of range densities of such materials on standard measures is unknown. Customized computational models must therefore be provided to best predict the strength of femur specimens.

2.3 Current Treatments

In the past thirty years significant research has been performed in the treatment of osteoporosis and numerous agents and devices have been developed, some of which have been shown to reduce fracture rates. The drugs include antiresorptive agents such as estrogens and selective estrogen receptor modulators, calcitonin, and bisphosphonates [27–31]. Issues inhibiting the efficacy of these drugs include cost, regimen, and time requirements. Some patients are not compliant with medicine usage, experience side effects, or require multiple medications for co-morbidities. More recently, medicines such as parathyroid hormone are being studied as treatments for osteoporosis but current guidelines for usage, especially when combined with bisphosphonates, do not exist [32]. Studies show that a 20% increase in the average BMD of the femur is required to restore mechanical strength of osteoporotic bone, but drugs can only increase BMD by a few percent [33]. It must also be noted that in the case of drug prescription, patient is not usually identified as at "high fracture risk" until they sustain a fracture in one femur, and that further limits the drugs efficacy [4]. None of these treatments have a substantial effect in short term and that is most crucial for the elderly, especially the ones who have already sustained a fracture in one hip and need an immediate near-term preventive treatment for the contralateral hip.

The major problem with use of mechanical devices such as hip protectors is patient's non-compliance and failure in continued use, not to mention the costs and discomfort associated with them [34]. Still, direct financial expenditures for treat-

ment of osteoporotic fracture are estimated at $10 to $15 billion annually [1].

2.4 Femoroplasty

Femoroplasty is a potential treatment for prevention of osteoporotic hip fractures. The procedure involves augmentation of femoral neck and / or trochanter by injecting augmentation material such as polymethylmethacrylate (PMMA) bone cement into those weakened areas of the bone [35]. The material, first in the form of a viscous dough, polymerizes within a few minutes of application and creates a solid region inside the bone tissue, presumably restoring its mechanical strength. Conventionally, the procedure is performed by drilling a cannula path through the greater trochanter and along the femoral neck and injecting the material while retracting the cannula. Enough cement is injected, usually about 40-50ml, that some parts of the head, the entire neck, and most of the greater trochanter are filled [2–4]. Figure 2.4 shows a radiograph of the cannula path for a conventional augmentation along with a sample computed tomography (CT) section of a conventionally augmented femur and its contralateral non-augmented counterpart.

Several studies employing the conventional gross filling method have reported success in increasing the strength and fracture energy of paired sample osteoporotic specimens [2–4]. In such studies, paired femora are harvested from cadavers and care is taken to ensure similarity between the two specimens. One is then chosen

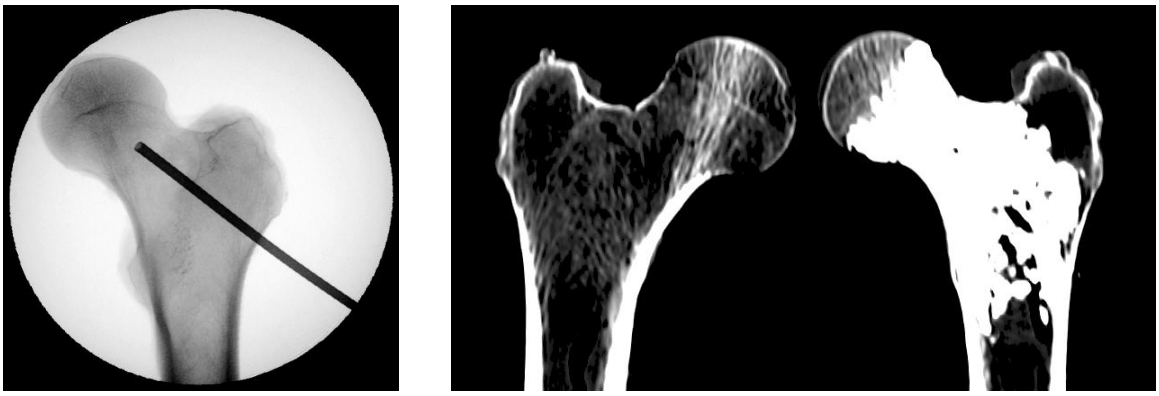

Figure 2.4: Radiograph of cannula path for a conventional augmentation (left) and CT slice of a pair of osteoporotic femora (right), one intact and one augmented with the conventional gross filling method.

at random as the control and the contralateral specimen is augmented with cement. Mechanical tests, simulating either a fall to the side or stance loading, are performed and fracture load and energy values are recorded.

Although seemingly successful, femoroplasty is not yet approved for clinical practice in the US, because of concerns and issues regarding the gross filling pattern. The curing process of the PMMA bone cement is vastly exothermic; namely it generates a substantial amount of heat that can potentially damage the bone tissue cells as well as the arteries and nerves. Osteonecrosis, i.e. tissue death as a result of poor blood supply, can occur if the arteries feeding the proximal femur are compromised. Heini et al. [3] injected, on average, $36ml$ of PMMA inside femora and recorded an average increase in the surface temperature of $22.1°C$. One expects that the temperature rise inside the specimens would be much higher. In a later study [4], they injected $40ml$

of a different cement and recorded $10.9°C$ and $11.4°C$ increase in the temperature on the posterior and anterior surfaces of the femur, respectively. They argue that if this method results in such increases in the surface temperature *in vitro*, one would encounter even higher temperature rises *in vivo*, which will likely damage the peripheral femoral arteries [3, 4]. Besides the issue of the temperature, poor cement placement can result in creating regions of stress concentration and premature fracture in the femur, which defeats the purpose of augmentation. The issue has been studied for vertebroplasty before [6, 36], but femoral augmentation lacks such literature. Introducing a large volume of cement inside femur also interferes with bone regrowth, it can cause fat embolism, and poses the risk of leakage into unwanted regions including surrounding arteries and nerves, not to mention the toxic nature of the cement monomer [12]. Therefore effective femoroplasty must employ limited cement volumes.

2.4.1 "Non-Conventional" Augmentation

Femoroplasty is still in its research stages and, with the exception of a few studies with the goal of pain reduction in patients with metastatic bone tumors in their hips [35, 37, 38], is not performed clinically. Therefore there is no established, "conventional" way of performing the procedure. Gross filling has been the method of choice in most studies, which has the limitations and risks discussed above. There have been attempts at achieving significant improvements in the mechanical properties of osteoporotic femora by using limited amounts of cement injection. However,

without planning, the most efficient placement of the cement is not known. Sutter et al. [11] limited their augmentations to $15ml$ of cement and targeted the neck and the grater trochanter separately. However, neither of the two cement placements resulted in a substantial increase in the strength or fracture energy of the femora. Beckmann et al. [5] achieved improvements in the biomechanics of the femora when they used single drilling paths, but observed lower fracture load and energy, or a non-significant increase, when double drilled paths were used. In a recent study, Fliri et al. [12] employed a "V-shape" augmentation approach by drilling two paths starting from the lateral cortex in the greater trochanter, one directed to the superior and one to the inferior aspect of the neck. They then injected, on average, $10.8ml$ of cement that increased the fracture energy of the specimens, but did not affect the yield or fracture loads. van der Steenhoven et al. [13] used a slightly different technique where they pre-drilled a cavity inside the femoral neck, either using an inflatable balloon or an eccentric drill, and then filled the cavity with Elastomer material ($18.5ml$ in the first group and $14.5ml$ in the second group on average). The augmentation resulted in less fracture displacement. However, neither techniques affected the fracture load of the specimens. Studies of Struss et al. [39] and Kaneko et al. [40] were aimed at repairing artificial defects in the femur using cement augmentation. In the former study, lag screws were inserted and subsequently removed from pairs of osteoporotic femora and one from each pair was augmented with cement. Fracture tests showed that augmented specimens had a larger fracture load. In the latter study, a metastatic lesion

was simulated in one femur from each pair by drilling a sphere out of the femoral neck. The defect was then augmented with 8-12ml of cement and mechanical tests showed that the loss of strength was restored by the augmentation. Table 2.1 provides a summary of previous femoroplasty experimental studies.

It seems that femoroplasty is a promising alternative to the conventional preventive measures of osteoporotic hip fractures. However, to be effective and pose minimum risk, femoroplasty needs to be precisely planned and carefully executed. Unfortunately planning of femoroplasty has received minimal attention in the literature, unlike its counterpart procedure performed on the vertebral bodies (vertebroplasty) [6–10]. Similar to vertebroplasty, femoroplasty can benefit from computer planning using computational models of bone biomechanics and cement infiltration of cancellous bone, as well as optimization of cement placement and intra-operative navigation for precise delivery of the plans.

2.5 System Overview

This thesis describes parts of the work that has been done for developing a computer-assisted framework of pre-operative planning, intra-operative execution / evaluation and post-operative assessment of femoroplasty. The long term objective of this research is to develop a technology that helps the orthopaedic surgeon determine the risk of fracture in an osteoporotic femur and obtain an optimized augmentation

Table 2.1: Summary of published experimental studies on femoroplasty, compiled from the studies of Heini et al. [3], Beckmann et al. (1) [4], Strauss et al. [39], Kaneko et al. [40], Sutter et al. (1) [2], Sutter et al. (2) [11], van der Steenhoven et al. [13], Beckmann et al. (2) [5], and Fliri et al. [12]

Study	# Pairs	Load Configuration	Cement Volume (ml)	Temperature Increase (°C)	%Yield Load	%Fracture Load	%Yield Energy	%Fracture Energy
Heini et al.	10	Stance	34	+20.9	-	+21*	-	+48*
Heini et al.	10	Fall	38	+23.3	-	+82*	-	+188*
Beckmann et al. (1)	9	Fall	40	+10.9	-	+43*	-	+187*
Strauss et al.[ł]	8	Stance	-	-	-	+21*	-	-
Kaneko et al.[Δ]	12	Stance	8-12	-	-	-5	-	-
Sutter et al. (1)	10	Fall	47	-	+22*	+37*	+80*	+154*
Sutter et al. (2)	18	Fall	15	+5	+9	+8	+7	+53
van der Steenhoven et al.	16	Fall	17	-	-	-5	-	-
Beckmann et al. (2)[□]	7	Fall	12[◊]	-	-	+23*	-	+160*
Beckmann et al. (2) [□□]	7	Fall	12[◊]	-	-	+35*	-	+164*
Beckmann et al. (2) [□□□]	7	Fall	12[◊]	-	-	+12*	-	+12
Beckmann et al. (2) [□□□□]	7	Fall	12[◊]	-	-	-26*	-	-19
Fliri et al.	5	Fall	11	-	+23[•]	-18[•]	-	+229*[•]

* Difference is significant.
ł Simulated defect by inserting and removing lag screws.
Δ Simulated lesion by drilling out a sphere from the neck. Only one femur from each pair was damaged and augmented.
□ Single central augmentation.
□□ Single centrodorsal augmentation.
□□□ Double ventrodorsal augmentation.
□□□□ Double craniocaudal augmentation.
◊ Mean for all the four methods.
• Difference in medians.

plan based on computerized models and biomechanical analyses. The technology is also intended to enable the surgeon perform a rapid and minimally-invasive hip augmentation based on the plan with near-real-time feedback, and finally verify the outcome in a few patient visits. Figure 2.5 illustrates the different components of the system that is envisioned to be used for such plan-based surgical operation.

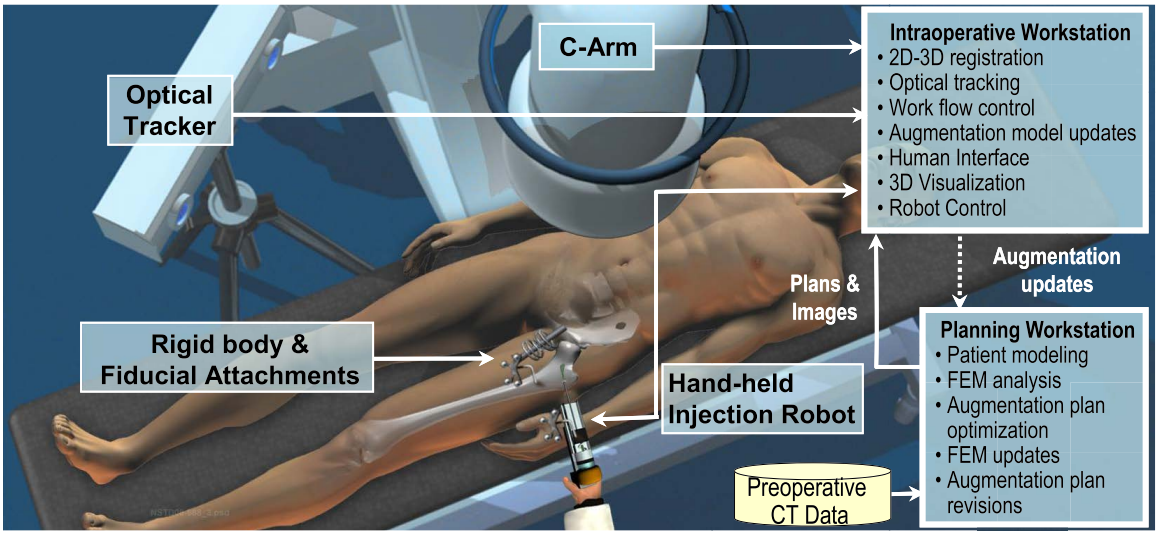

Figure 2.5: System setup and information flow. Taken from [41], with permission.

The planning module provides the surgeon with an optimized pattern of injection on the basis of mechanical analysis and optimization performed on a patient-specific 3D model created from CT data before the surgery. During the operation, the injection will be performed using an automatic injection device that can be used in either a hand-held or a fixed-base mode. The surgeon guides the device to the desired point(s) of injection with the aid of an infrared camera and real-time navigation. At some intermittent points during the augmentation, multiple X-ray images are taken and

the 3D pattern of injection is updated thanks to real-time 2D / 3D registration techniques [42]. The progress of injection is fed back to the planning module for analysis and, if needed, plan update.

This document describes the different components of the planning module, as well as parts of the intra-operative workstation. For the purpose of experimental tests (Chapters 5 and 7), we used a subset of the entire system, as described below.

An overview of the sub-system is shown in Figure 2.6. This framework shares some components with a previously developed system of Biomechanical Guidance System (BGS) for Peri-Acetabular Osteotomy (PAO) [43–47].

CT scans acquired from cadaveric specimens are used to create patient-specific models for biomechanical evaluation and planning of augmentation. Planning consists of the following main modules: after biomechanical evaluation of the intact model, an optimization technique is used to determine the optimum cement placement inside the femur. Next, a cement diffusion prediction model is used to determine a practical augmentation strategy that most closely matches the optimally found cement pattern. The plan is then sent to the intra-operative execution workstation which uses registration and navigation tools to help the surgeon guide the drill, followed by the automatic injection device, to the pre-determined location for injection. After the augmentation CT scans are taken and the injected cement is compared with the planned pattern. Finally, fracture tests are performed to determine the biomechanical outcome of the surgery and to compare that with the planned augmentation outcome.

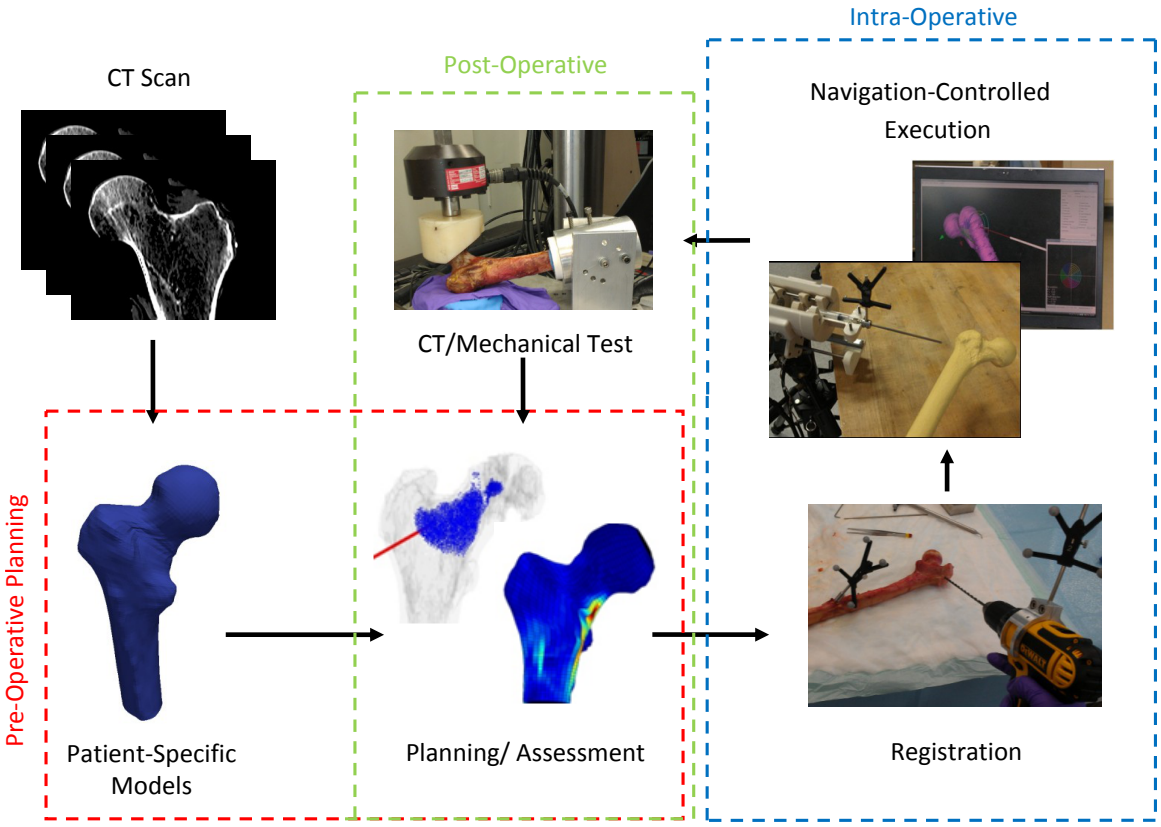

Figure 2.6: Main components of the framework we used for computer-assisted femoral augmentation on cadaveric specimens.

Chapter 3

Finite Element Analysis of Femoroplasty

3.1 Introduction

Modeling mechanical properties of the bone has been the topic of research in the biomechanics community for several years. Finite Element Analysis (FEA) has proved to be a powerful tool in modeling and predicting the mechanical behavior of bone tissue under various loading conditions. However, reliable FE modeling of the bone requires precise geometry formation and material assignment which are challenging due to the nonlinear and inhomogeneous structure of the bone.

With the increasing power of imaging techniques such as CT scanning, high resolution 3D images of the living tissues are possible at relatively low costs. Converting

those images to appropriate FE models, however, is not a trivial task. Voxel-based and geometry-based models are the two main categories of FE models existing in the literature [48]. The former involves directly converting the CT image voxel data to hexahedral brick elements whereas the latter involves first extracting the surface geometry of the bone and then converting the surface to a volumetric mesh, usually using tetrahedral elements. Examples of the two methods are presented in the works of Keyak et al. [49] and Gomez-Benito et al. [50], respectively. Voxel-based models have the obvious advantage of ease of creation, but they produce jagged surfaces and hence erroneous results at the surface of the models [48]. Furthermore those models involve hundreds of thousands of elements and require substantial computational resources and timing. Creating geometry-based models, on the other hand, requires more manual operation time and is not as trivial, but those models are generally more accurate and require less computational times [51]. In the context of geometry-based modeling, there are two popular types of elements used for meshing: tetrahedral and hexahedral (brick) elements, both of which can be implemented with linear or non-linear shape functions. Most commercial meshing software have built-in modules for creating tetrahedral meshes, given a surface model of the desired object. In general, at equal mesh density, quadratic elements generate more accurate results than linear elements, with the added cost of CPU time. They also do not suffer from a phenomenon called "shear-locking", which is large, unphysical shear strains produced in bent elements. Shear-locking in linear meshes can be resolved by refining the mesh

in the bent area of the model, which increases the CPU time substantially. In general, with enough resolution, tetrahedral and hexahedral elements seemingly bring the same performance [52]. Studies, however, have shown that femur models that employ hexahedral elements are less sensitive to the number of degrees of freedom (DOFs) in the model than the ones made of tetrahedral elements [53].

Assigning material properties to the elements of the models also plays a pivotal role in the finite element analyses. Some studies consider a uniform distribution of isotropic elastic modulus for the entire cortical or trabecular regions of the bone [54], but it is well established that bone stiffness varies significantly for various sites of the bone [55, 56]. Several research studies with the goal of relating elastic modulus and strength to density and / or CT voxel intensity values have been performed (e.g. [56–59]). However, to date, there is no consensus regarding this issue [60]. Furthermore it is well known that the bone tissue is, in contrast to the common isotropic behavior assumption for most FE models, highly anisotropic. However, there is little literature about relating density measures to orthogonal mechanical properties of the bone [60]. Transverse isotropy is usually assumed for simplification. The challenge here is to determine the axis of anisotropy from CT voxel data. A first step in addressing this issue was taken by Lenaerts et al. [61], but the results were not validated. Peng et al. [62] compared isotropic and transversely isotropic FE models of femur bone, and concluded that the results are not significantly different. However, the fact that the direction of the main axis of anisotropy changes throughout the

bone was not considered [63]. Furthermore, only loading conditions corresponding to stance were studied, leaving open the question for other loading conditions.

Failure prediction poses another major challenge. Researchers have tried to apply common engineering yield and failure criteria to bone tissue. However, similar to the previous issue, there is no general agreement on the most appropriate criteria to use. Keyak and Rossi, through a comparative study [64], concluded that using the distortion energy theory, i.e. employing von Mises stress as the yield criterion for elements, results in the best agreement between simulations and experimental data. More recent studies [65, 66], however, showed that maximum principal strain is the better criterion to use for this purpose. Failure prediction methods can also be divided into static and dynamic methods. The former involves a single static analysis of the FE model and then scaling the results to determine the onset of yielding (e.g. [66,67]), while the latter requires updating material properties of the failed or yielded elements and running the FE analysis in each step, e.g. [24]. Keyak et al. compared static [68] and dynamic [69] failure predictions and concluded that the latter outperforms the former in agreeing with experimental results. Juszczyka et al. [70], however, pointed out that the femur behaves linearly up to the point of failure, justifying the static yield load prediction. A good review on the current state-of-the-art in FE modeling of bones can be found in the work of Poelert et al. [71].

As described in the previous chapters, we propose a precise planning and execution routine for femoroplasty, which is still in pre-clinical stages. Modeling of the

mechanical behavior of the femur bone under different augmentation scenarios is of crucial importance to the success of this procedure. The model will be used for pre-operative optimization of the bone cement injection specifically aimed at minimizing the required injection volume while reducing or eliminating the likelihood of fracture under standard loading conditions (Chapter 4). The optimization requires several iterations of the FEA, within a loop, in order to achieve the optimum plan. During the surgical procedure, it is also desirable that the model be used for intra-operative assessment and to update the augmentation plan. For this to be viable, the finite element model must be solved and analyzed in relatively short amounts of time.

The objective of this study was to develop a patient-specific finite element modeling framework for the proximal femur, investigate the sensitivity of the model to mesh resolution, and to validate its capability of predicting stiffness and yield load using results of previously performed mechanical tests on human cadaveric femora. [1]

3.2 Methods

A customized user interface [2] (MATLAB, Mathworks Inc., Natick, MA) allowed the author to manipulate the CT scan data of the study of Sutter et al. [11], obtained from nine pairs of osteoporotic femora prior to mechanical fracture tests, before and after one femur of each pair was augmented by PMMA bone cement, and to perform

[1] This chapter is published as [72].

[2] The interface was first developed by Mr. Robert Armiger and Dr. Michael Kutzer of the Johns Hopkins Applied Physics Laboratory and further expanded by the author.

pre-processing steps for the finite element solver. These steps included creating a patient-specific finite element mesh, assigning material properties and defining loading and boundary conditions. First, the isosurface of the image volume was used to estimate (with manual refinement) the main geometrical features of the bone including the long bone axis and head center to establish a local coordinate frame. Using the graphical interface, slices of the 3D model were created orthogonal to the defined path along the femoral long axis and up through the head of the femur as shown in Figure 3.1. An arc was used to smoothly connect the femoral long axis with the axis traveling through the neck and head of the femur. The arc helped change the orientation of the slices so that features of the proximal part of the femur were captured more effectively. The user was free to change the control points to refine slicing including the diameter of the connecting arc and / or the number / spacing of slices along the path to ensure that critical features of the femur are captured. For each slice, an estimated section of the femur was created from the CT by interpolating intersecting voxel data. This interpolated section was then automatically processed using intensity based segmentation, followed by manual refinement, to estimate the outer geometry of the bone. A radial grid was then defined about the center axis of the path orthogonal to the slice, with concentric grid lines laid out. The number of discrete circumferential points aligned in each section was constant, therefore the grids could be easily combined to form a finite element mesh of quadratic 15-node wedge and 20-node brick elements [73] (Figure 3.2). Smoothing splines were finally

applied to the resulting model to create a smooth outer surface.

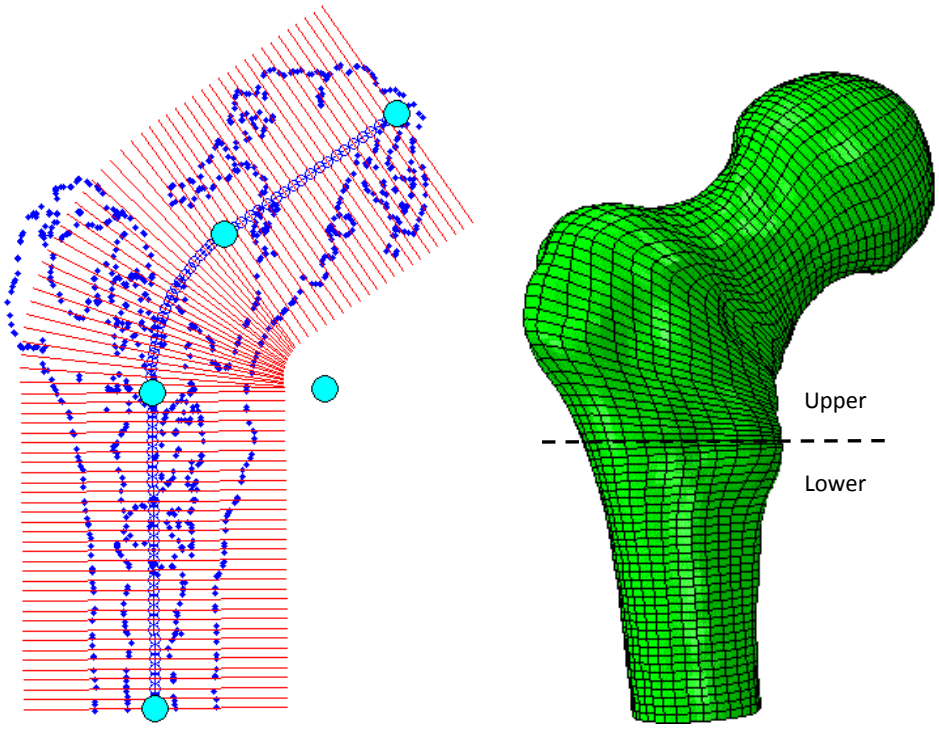

Figure 3.1: Oblique user-defined slices (left) and the corresponding finite element mesh (right). The cyan circles represent the control points that determine the properties of the curve of the slices.

In order to estimate the structural response of the osteoporotic femora, inhomogeneous material properties were assigned to the elements based on the bone density observed from CT scan. First, we calculated the average radiodensity in Hounsfield Unit (HU) intensity values for each element. This was done using 3 sampling points along each of the edges of the element, which resulted in 21 and 27 points for the wedge and brick elements, respectively. The HU value was sampled at these points and, to only take into account the bone tissue, the average of the non-negative values

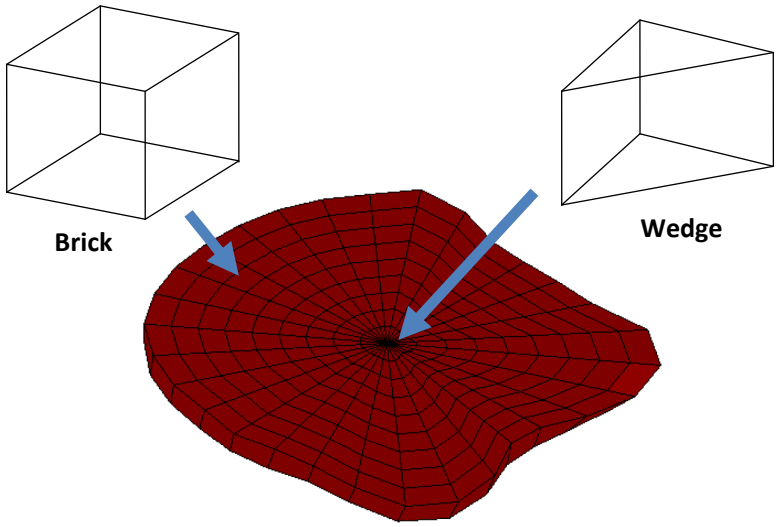

Figure 3.2: A representative "layer" of a bone model and its comprising elements.

was considered as the element intensity number. The next step involved converting the intensity values to elastic modulus constants. For this purpose, we divided the bone into two main regions (Figure 3.1): the $90mm$ upper part of the proximal femur (the "upper" region) and the rest of the bone (the "lower" region). We considered the upper region as mostly trabecular bone and the lower region to be mostly cortical bone. To account for the bone marrow, elements of $HU_{mean} < 100$ were added to the marrow material group. Individual HU_{mean} values of bone elements were converted to ash densities (the ratio of weight of bone ash over the ash volume) using linear interpolation of the known data for plastic phantoms that were placed next to the femora at the time of CT scanning. The ash densities were finally converted to apparent densities (weight of wet bone over its entire sample volume) using Eq. 3.1 [74],

$$\rho_{app} = 1.79\rho_{ash} + 0.0119 \tag{3.1}$$

where ρ_{app} and ρ_{ash} denote the apparent and ash densities in gr/cm^3, respectively. The last step was to convert the density values to isotropic elastic modulus. Eq. 3.2 was used for this purpose [75, 76]:

$$\begin{aligned} E &= 10500\ \rho_{ash}^{2.29} \text{ Cortical Bone} \\ E &= 6850\ \rho_{app}^{1.49} \text{ Trabecular Bone} \end{aligned} \tag{3.2}$$

where E is the elastic modulus in MPa and a Poisson's ratio of 0.4 was assumed for all the bone elements [77, 78]. The "Cortical" equation was used for the distal part and the "Trabecular" equation was used for the proximal part. Bone elements elastic moduli ranged from $187MPa$ to $28.4GPa$. For bone marrow elements, the elastic modulus was set to 20 MPa with a Poisson's ratio of 0.499 [62]. To account for the high radiodensity of bone cement injected in the femoral neck and prevent an artificial increase in the intensities of the bone tissues surrounding the cement, we co-registered and re-sampled the augmented femora before and after injection of cement. The co-registration was performed using an affine transformation based on mutual image intensity information (Analyze, Mayo Clinic, Rochester, MN). We then calculated the mean HU intensity for each element based on both image volumes, namely HU_{nonaug}, HU_{aug} and if the difference was larger than a threshold for any of

the elements, we added the element to the bone cement material group. We then assigned to this material group an isotropic elastic modulus of $1.2GPa$ [79] and a Poisson's ratio of 0.4. Figure 3.3 shows an example cement distribution in the model and compares it with the corresponding CT image rendering.

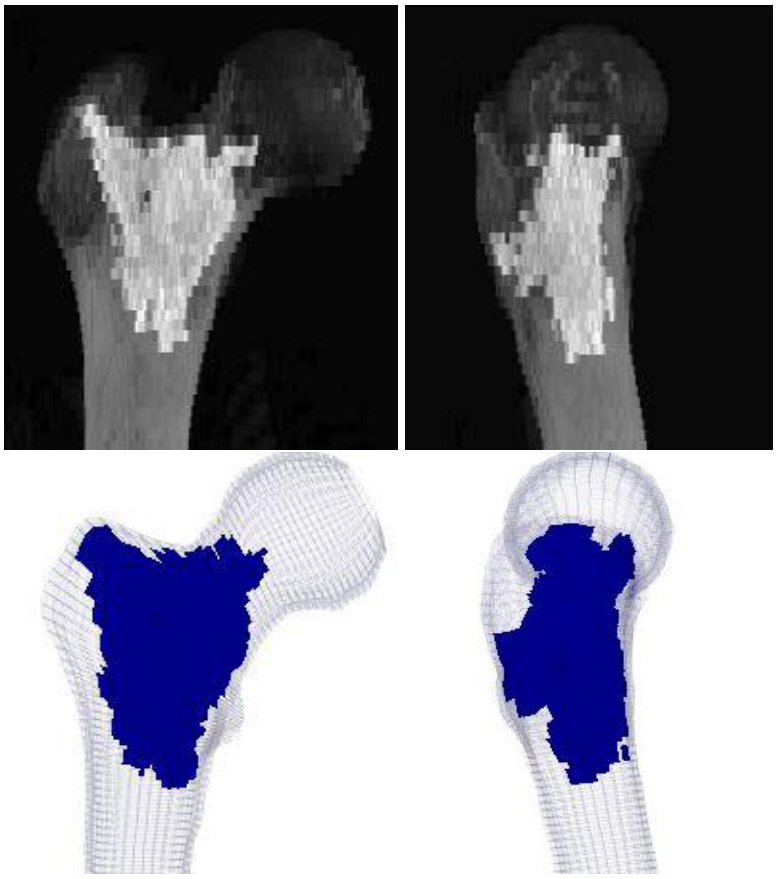

Figure 3.3: Sample cement distribution as seen in the CT projection image (top) and the corresponding cement element distribution in the FE model (bottom).

Boundary conditions replicating the mechanical tests were applied to the finite element models (Figure 3.4). The bone model was first reoriented according to the rotations applied for the mechanical test [11]. The distal vertices were then fixed in

all three directions and the surface vertices on the $10mm$ lateral side of the greater trochanter were restricted to move only in the $y-z$ plane (perpendicular to the plane of Figure 3.4). Finally, load was applied on the surface vertices of the medial part of the femoral head. Loaded vertices were allowed to move in all three directions. Load magnitude was set to an arbitrary value of $500N$ and it was evenly distributed among the loaded nodes.

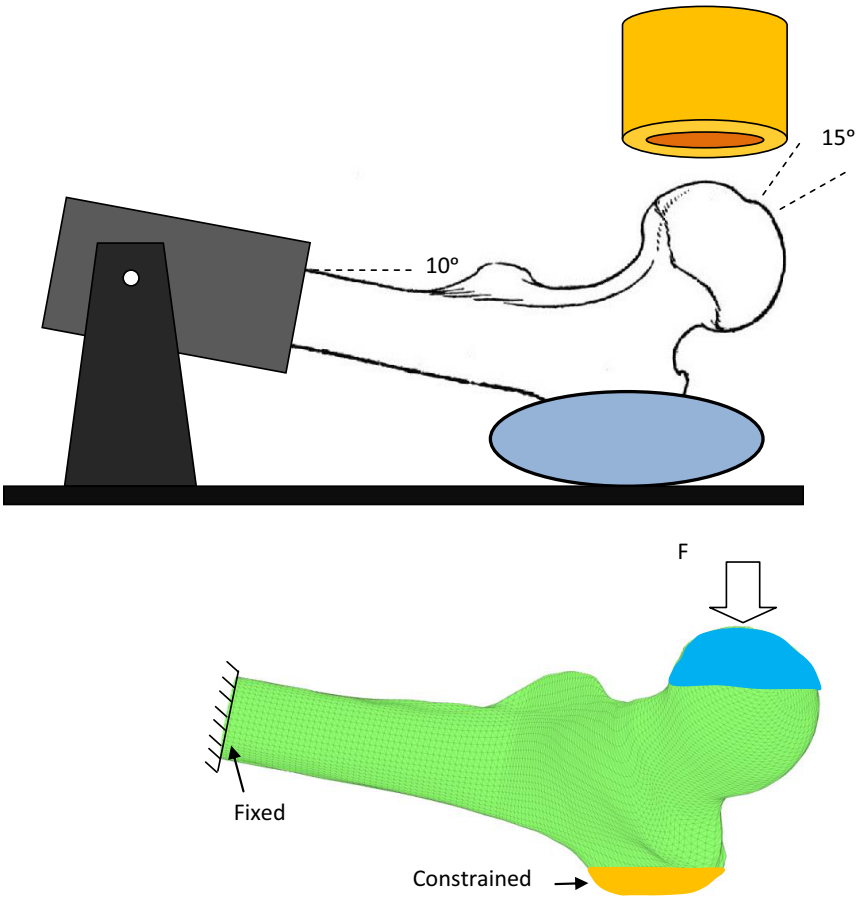

Figure 3.4: Schematic of the mechanical tests (top) and boundary conditions representation (bottom).

A static FE analysis was performed on the model using ABAQUS (ABAQUS / Standard v6.8, SIMULIA, Providence, RI). Output parameters from the FE solver included the displacement component of the loaded nodes in the direction of the load and maximum and minimum principal strain values, reported at the centroid of each element. Bone stiffness was calculated as the ratio of the load to the average displacement of the loaded nodes in the direction of loading. Maximum (ϵ_{max}) and minimum (ϵ_{min}) principal strain values of the elements were used to determine element yield. Using the FEA results at the load of $500N$ and assuming linearity, ϵ_{max} and ϵ_{min} could be scaled for any desired load. For each element the greater value of $|\epsilon_{max}|$ and $|\epsilon_{min}|$ was chosen as the element strain and it was compared with the appropriate (compressive ϵ_{yC} or tensile ϵ_{yT} ($= 0.7\epsilon_{yC}$ [66])) yield strain. If the element strain exceeded its yield value, its volume was added to the volume of the failed elements. We increased the load until the total volume of the failed elements reached 1% of the total volume of the specimen [67]. The load at that point was the assumed yield load of the femur. We varied the yield strains, using the data and models for the two pairs of specimens with the lowest and highest yield loads (the "training" set), to determine the values of ϵ_{yC} and ϵ_{yT} that resulted in the best agreement between the FEA and experimental yield loads. For the rest of the models, we used those values for estimation of the yield load. For PMMA cement elements, yield strain was set to a symmetric value of 2% [80]. This method of predicting the yield load had shown to be comparable with dynamic yield load prediction, detailed in Appendix A.

We performed correlation and error analyses on the experimental and FE simulation results for stiffness and yield load. We also performed paired sample t-tests on stiffness and yield load values obtained from non-augmented and augmented specimens, both for experiments and FE simulation results.

To verify model convergence, we varied the mesh element density for one randomly chosen femur bone and applied the same boundary conditions on them as mentioned before. The FE results were then recorded for the models, with one additional output of the sum of the stored strain energy values in all the elements. Assuming the densest model as the reference, the model with minimum number of elements and stiffness and energy within less than 2% of the reference values was considered the optimum model. We then created the rest of the models with the same number of elements found for the optimum model. This was done to avoid unnecessary calculation overhead resulting from overly fine meshes. Simulations were performed on a machine with $3.2GHz$ Core2^{TM} Duo processor and $8GB$ of physical memory under 64-bit Windows^{TM} 7 operating system.

3.3 Results

Results of the sensitivity of the finite element analysis to the density of the mesh are depicted in Figure 3.5. Each of the two plots shows a plateau when the number of degrees of freedom (DOF) in the model increases beyond $\sim 250,000$ and the last

three dense models produce closely similar results. Assuming that the densest model analyzed (with 528,081 DOFs) has the most accurate results, we see that the model with 244,671 DOFs produces a stiffness and absorbed energy within 1.23% and 1.15% of the dense model, respectively. The time associated with solving these models was $950s$ for the dense and only $180s$ for the less dense model. Based on the nominal anticipated increase in accuracy associated with increasing the DOFs beyond 250,000 and because of the excessive increase in computation time, we selected 250,000 (20,000 elements) as the target DOF for creating the models. Similar convergence trends can be found in the literature [6].

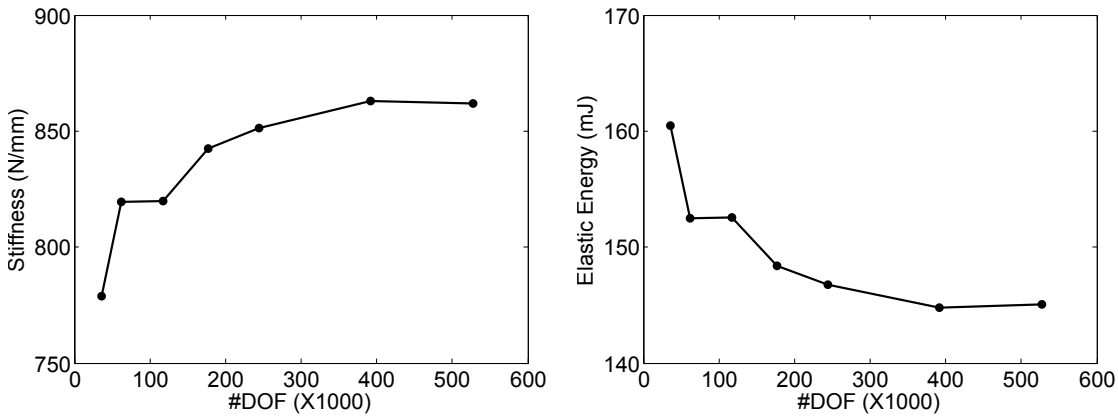

Figure 3.5: Stiffness (left) and absorbed energy (right) as a function of mesh density.

The value of ϵ_{yC} that produced the closest agreement between the FEA and experimental data of the yield loads for the "training" specimens was found to be 0.0427 (with the corresponding value of ϵ_{yT} of 0.0299). Figure 3.6 compares the results of FE simulations with the data gathered from the experiments. Table 3.1 also shows a

comparison between the experimental and simulation results. The average errors in predicting the stiffness were 17.2% and 17.7% for control and augmented specimens, respectively. The corresponding errors for yield load were 9.8% and 15.6%. For seven out of the nine pair comparisons, FEA predicted correctly whether the augmentation increased or decreased the yield load.

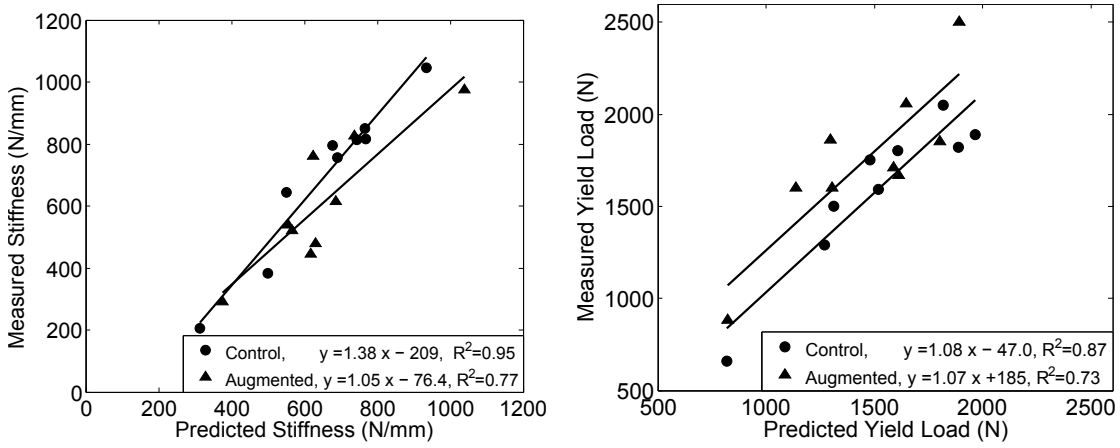

Figure 3.6: Comparison of stiffness (left) and yield load (right) values between experiments and FEA analyses.

Similar to the experiments [11], FEA showed no significant difference ($P > 0.05$) in stiffness or yield load between augmented and control specimens. An evaluation of the distribution of the failed elements before and at the onset of yielding showed that, for all the non-augmented specimens, FEA predicts the yielding to start at the superior aspect of the femoral neck. For the augmented specimens, the yielding region was slightly shifted, either towards the proximal part of the neck or the trochanteric area, and there was always a region of concentrated failed elements at the cement-

Table 3.1: Summary of experimental and FEA results.

Specimen	Stiffness (N/mm)				Yield Load (N)			
	Measured Control	Predicted Control	Measured Augmented	Predicted Augmented	Measured Control	Predicted Control	Measured Augmented	Predicted Augmented
1	851	767	616	688	1820	1890	1600	1305
2	815	746	446	618	1800	1610	1710	1590
3	797	678	828	740	1750	1480	1860	1300
4	206	314	290	377	660	820	880	825
5	644	551	539	557	1500	1315	1600	1140
6	818	770	480	633	2050	1820	2500	1895
7	1047	936	763	625	1890	1970	1670	1615
8	756	693	520	568	1590	1520	1850	1805
9	383	500	976	1042	1290	1270	2060	1650
Mean (±SD)	702 (±257)	662 (±182)	607 (±213)	650 (±179)	1594 (±416)	1522 (±359)	1748 (±432)	1458 (±343)

bone boundary. None of the augmented models had yielded cement elements up to the onset of predicted yielding.

3.4 Discussion

Results of our study support the original hypothesis that patient-specific FEA can accurately predict femoral stiffness and yield load for both augmented and non-augmented specimens. The models showed slightly lower accuracy in predicting the properties of augmented specimens compared to the intact bone models. This could be due to the added assumptions regarding the mechanical behavior of the bone cement, including its stiffness and its bond with the bone tissue, which was assumed perfectly rigid in the current study. Also the neglected effects of volume fraction information obtained from CT data could have affected the element properties at the

boundary between the bone and the cement.

In order for the model to predict the yield loads accurately, tuning of the failure strain of the elements was inevitable. There is a wide range of reported values for experimental yield and ultimate compressive and tensile strains for human cancellous bone, e.g. 0.003-0.03 [81], with some studies reporting values as large as 11.6% [82]. Furthermore, individual elements of the model generally contain several trabeculae as well as soft tissue and marrow, and we hypothesize that the combination of the yielding of those will result in the total element failure. Therefore total element failure is likely to happen at a larger apparent strain [6, 24]. In addition, it is likely that the trabecular structure acts differently within the bone structure compared to when tested as excised specimens in mechanical tests. It is also well documented that bone fails at lower strains in tension than in compression [66], hence our assumption of $\epsilon_{yT} = 0.7\epsilon_{yC}$.

The simulated load was increased until 1% of the volume of the elements within the model failed. This value is grounded in experimental testing of distal radius failure [67]. Due to the substantial structural and geometrical differences in the femur and the radius bone, the 1% failure criterion may not be most suitable for the femur. It is not precisely known what percentage of the elements fail at the onset of yielding and the 1% yield criterion is somewhat arbitrary [67]. However, with the 1% criterion, failed elements populated a relatively small area inside the bone which helped identify the region of initial failure. Because of our strain-based yield criteria,

errors can also propagate when converting loads to stress and subsequently to strain values. It must be emphasized that the main purpose of developing the proposed finite element modeling scheme was to evaluate various cement augmentation scenarios and therefore the effects of augmentation on yield loads are of more importance than absolute load values [71].

For two pairs of specimens (#3 and #5), FEA predicted a decrease (-12% and -13%) in the yield load of augmented vs. control specimen, while in practice an increase (+6% and +7%) was measured. The measured changes were within error margins of the simulation which could partially explain the deviation of FEA from experiment. On average, as shown in both experiments and simulations, augmentation did not improve the mechanical strength of the femora. This was mainly due to the relatively small injection volume of cement ($15ml$) as opposed to the conventional gross filling patterns [2–4]. The injection volume was kept small to reduce thermal damage to the bone tissue. However, for most of the specimens, a major portion of the cement volume was populated in the trochanteric area, while the target augmentation region was the femoral neck. Therefore femoral neck, and especially the superior aspect of the neck where there is a stress concentration, was not properly supported by the cement.

Discrepancies between the models and experiments stem from simplifications in the models as well as imperfections in performing the experiments. More specifically, errors in applying the rotations when positioning the bone under the loading device

can affect the stiffness and yield load of the bone, as found in other studies [83, 84]. These errors can be reduced or eliminated by adding information regarding the orientation of the bones in experiments to the simulations, e.g. using tracking information at the time of tests.

The time to solve the static finite element model and estimate the stiffness and yield load was about 3 minutes total. This is orders of magnitude less than the times reported in similar studies, especially ones for which dynamic or quasi-dynamic analyses are employed [24,67,85], due to the quasi-static nature of our FEA and use of limited number of necessary elements. For our application, as also noted by Yosibash et al. [66] and shown in Appendix A, static yield prediction is sufficient to predict the onset of bone tissue failure in a near-real time environment. Therefore more time consuming dynamic FEA are prohibitive and seem to be unnecessary for this effort. The proposed model can be conveniently incorporated in an optimization framework for finding optimum cement placement with the best outcome (Chapters 4 and 6).

Since the original experiments did not include high speed video capture data, in this study we were not able to directly compare the simulations and experiments for the location of first yielding. Similar experimental studies by Dragomir-Daescu et al. [24] and de Bakker et al. [25] have shown that, under similar loading conditions, there is often a local compressive yielding at the superior aspect of the femoral neck prior to final fracture. This is the same pattern that was observed in the current study for non-augmented models. During a fall to the side, compressive stress acts on the

superior neck, while tensile stress is applied on the inferior side [25]. Although bone is stronger in compression than in tension, it is suggested that the reduced thickness of the cortical bone in the superior aspect compared to the inferior aspect is responsible for this yielding [25].

The current study assesses the feasibility of creating a patient-specific finite element model of the proximal femur for predicting the onset of bone failure and assessing the effect of mitigating interventions (bone augmentation with bone cement). This analysis approach has the potential to be used in a system for pre-operative planning and intra-operative assessment of bone augmentation surgery. A crucial step in the planning process is to determine the optimum volume and filling pattern of the cement so that the best outcome is achieved. For this purpose, numerous augmentation scenarios and cement placements, within an optimization loop, must be simulated, and this can only be practical if the finite element analysis can be performed in a relatively short amount of time. In this chapter, we presented a framework for patient-specific femur finite element model generation and analysis. Our FE simulations showed acceptable errors and correlated well with the experimental data of previously tested femora, while being solved in relatively short times.

3.5 Recapitulation of Contributions

The author developed a patient-specific finite element model generation and analysis user interface based on CT scan data. Semi-automatic segmentation and model generation was facilitated through the program. The modeling approach was validated against previously augmented and tested femur specimens in a fall to the side loading configuration. This provides a baseline for optimization and planning of femoroplasty, which is discussed in the forthcoming chapters.

Chapter 4

Cement Placement Optimization

4.1 Introduction

Compared to femoroplasty, there is a rather substantial body of literature regarding the effect of cement injection in restoring mechanical properties of vertebral bodies in vertebroplasty, both experimental and simulated [7, 86–89]. Research has been done on the dependence of augmentation on the volume and placement as well as material properties of the cement itself. Belkoff et al. [90] tested three different commercial PMMA cements and found that two out of three restored the stiffness of compromised vertebral bodies and all three increased the fracture strength. Heini et al. [8], through experimental tests, found that both PMMA- and calciumphosphate (CaP)-based cements could be useful in restoring mechanical properties of osteoporotic vertebral bodies. They also concluded that the lower the initial BMD, the

more pronounced is the effect of augmentation. Sun and Liebschner [7] varied cement properties in their FE simulations to find optimum cement material characteristics. They concluded that increasing the cement strength increases the strength of the augmented vertebral body but this effect plateaus beyond a certain threshold. Also they found that increasing the stiffness of the cement increases the stiffness and strength of the bodies but strength plateaus as, beyond some threshold, fracture always happens at the weakest point at the bone-cement interface. In another simulation study [6], they reported that a rather "dispersed" cement filling pattern can be beneficial to the vertebral body for it creates a more uniform stress distribution while augmenting the strength, as opposed to stress concentration in compact filling patterns that can affect the adjacent vertebral bodies and cause premature fractures. Similar conclusion about the load transfer of compact filling was made by Polikeit et al. [36]. There is a general agreement that increasing the volume of the cement increases the stiffness and strength of the vertebral bodies [6, 7, 9, 10, 86].

Although findings about vertebroplasty and its optimization could, to some extent, be generalized to femoroplasty, there are fundamental differences between the two procedures. These include the much smaller volumes of cement needed for vertebroplasty—it is reported that as little as $2ml$ and up to $8ml$ of cement is enough to restore strength and stiffness of the vertebral segments that are compromised as a result of osteoporosis [9, 87]. Furthermore, compared with femora, vertebral bodies have less complicated geometries and experience less varied loading conditions. Nev-

ertheless, there hasn't been, to the author's knowledge, any attempt in optimizing the cement volume and placement in a systematic way for either procedure.

In this chapter, we set out to optimize the volume and placement of bone cement in femoroplasty using finite element (FE) modeling. The method of choice is Bi-directional Evolutionary Structural Optimization (BESO). A simple form of the method was introduced by Xie and Steven [91] for the purpose of shape and layout optimization of structures. Simply put, the entire domain of interest is populated with finite elements and then elements are removed from low stress regions progressively as the model is solved in each iteration. It is possible, however, in the process of evolving the structure, for regions of high stress to appear for which reinforcement is necessary. An alternative way of approaching the problem, i.e. Additive Evolutionary Structural Optimization (AESO), would be to start with the minimum needed number of elements, typically connecting the loads to the boundary regions, and progressively add elements to the regions of high stress [92]. Similarly, this method can create regions of low stress where unnecessary material is used. It is only natural to combine the two methods in a bi-directional way, taking advantage of the benefits of both [93, 94].

When the method was introduced in 1993, it was regarded by the authors as an entirely new method that seemed to create results similar to gradient-based methods of optimization, despite the relatively simpler setup and execution. They used stress-based rejection / addition criteria initially. However, simple calculations reveal

that if strain energy-based criteria are employed, BESO acts similar to a typical stiffness maximization problem with an overall mass constraint [95, 96]. Take a typical structural optimization problem, formulated as Eq. 4.1:

$$\begin{aligned} min\ C &= \frac{1}{2} F^T u \\ Subject\ to\ Ku &= F \end{aligned} \tag{4.1}$$

where C is the so-called structural compliance, F is the external load vector, u is the nodal displacement vector and K is the stiffness matrix. Minimizing the overall structural compliance is equivalent to maximizing the stiffness of the structure. Assume we remove element i from the structure in order to reduce its mass. The change in the stiffness matrix could be represented by Eq. 4.2:

$$\Delta K = K^* - K = -K^i \tag{4.2}$$

Here K^* is the new stiffness matrix and K^i is the contribution of the element to the overall stiffness matrix K. Assuming the external load vector remains the same, the change in the displacement vector can be estimated as Eq. 4.3

$$\Delta u = -K^{-1} \Delta K u \tag{4.3}$$

Therefore one can calculate the change (increase) in the compliance:

$$\Delta C = \frac{1}{2} F^T \Delta u = -\frac{1}{2} F^T K^{-1} \Delta K u = \frac{1}{2} u^{iT} K^i u^i \tag{4.4}$$

which is the strain energy stored in the removed element. Since the objective is to keep the compliance below some predefined threshold ($C < C^*$), it is most effective to remove the element with the smallest strain energy so that the increase in compliance is minimal.

Since BESO does not directly use the gradient information, it is less complex and not as sensitive to the discontinuity in the solution space. Therefore, we used the method of BESO to optimize geometry and placement of the bone cement inside osteoporotic femora. [1]

4.2 Methods

In the first step, finite element models for three osteoporotic femur samples were created as the base models for cement placement optimization. The models were created from CT scans according to the procedure described earlier in Chapter 3 [72]. Number of degrees of freedom (elements) varied between 224,697-239,727 (18,500-19,750) for the models. Models consisted of layers of elements, each made of concentric rings of quadratic 20-node brick, completed with 15-node wedge elements at the center [73]. Heterogeneous material properties, based on each element's average

[1] This chapter is presented as [97].

HU intensity, were assigned to the models' elements. To this end, first each element's average HU value was converted to ash density using linear interpolation of known values for plastic phantoms that were placed near the specimens at the time of scanning. Apparent density was computed using $\rho_{app} = 1.79\rho_{ash} + 0.0119$ where ρ_{ash} and ρ_{app} are the ash and apparent density in gr/cm^3, respectively [74]. Finally elastic modulus for each element (in MPa) was found using Eq. 4.5 [75, 76]. The upper $90mm$ of the bone model was considered mainly trabecular and the distal part, cortical bone. Also, for each element, if the HU value was less than 100, an elastic modulus of $20MPa$ and Poisson's ratio of 0.499 was assigned, resembling marrow [72].

$$\begin{aligned} E &= 10500\ \rho_{ash}^{2.29} \text{ Cortical Bone} \\ E &= 6850\ \rho_{app}^{1.49} \text{ Trabecular Bone} \end{aligned} \tag{4.5}$$

Boundary conditions similar to a fall to the side on the greater trochanter [2] were applied to the models and a $500N$ force was evenly distributed on the surface nodes of the head of the femur.

The BESO algorithm that we implemented on the models can be summarized as the following:

- Define the "domain" of interest. The domain, in this context, is the region where the optimizer can add or remove PMMMA cement elements. In our simulations, the domain was assumed to be the entire proximal part of the bone model except

the outer-most elements. It must be noted that the complete bone model—the optimization domain as well as the rest of the model—was solved for at each FEA iteration.

- Populate the domain with "0" and "1" elements. In the current study, two initializations for the distribution of cemented elements ("1" elements) were examined: fill the entire domain with cement elements ("FULL") or start with no cement elements ("ZERO"). It must be noted that the "0" elements were assigned their original bone properties and the "1" elements were assigned an elastic modulus of $1200MPa$ and a Poisson's ratio of 0.4, representing the bone cement [79].

- Choose the optimization criterion. Here strain energy of the elements of the entire bone model was used which, as described earlier, is useful in stiffness maximization problems [96].

- Run a linear static finite element analysis.

- Find the elements that satisfy Eq. 4.6 or Eq. 4.7:

$$\sigma_e \leq RR\sigma_{max} \tag{4.6}$$

$$\sigma_e \geq IR\sigma_{max} \tag{4.7}$$

where σ_e is the element strain energy and σ_{max} is the maximum strain energy in the domain. The Rejection Ratio (RR) and Inclusion Ratio (IR) can be computed using Eq. 4.8 and Eq. 4.9 [93]:

$$RR = r_0 + r_1 SS + a_{RR} ON \tag{4.8}$$

$$IR = i_0 - i_1 SS - a_{IR} ON \tag{4.9}$$

Here $r_0 = 0$, $r_1 = 0.01$, $a_{RR} = 0.01$, $i_0 = 1$, $i_1 = 0.1$ and $a_{IR} = 0.1$. Those values were obtained experimentally to yield the best results. The Steady State number (SS) starts with 1 and is increased by one whenever no element satisfies Eq. 4.6 or Eq. 4.7. The Oscillation Number (ON) starts with 0 and is increased by one where an "oscillation" is reached where same group of PMMA elements are added in one step and are removed in the next one. If a "1" element satisfies Eq. 4.6 it will be "0" for the next step. If any of the elements satisfies Eq. 4.6, its neighboring elements and the element itself will be "1" for the next step.

- Repeat the two previous steps until the stopping criterion is reached. For the case "FULL", the procedure stopped when the predicted yield load of the model fell below twice its value for the original bone model and for the "ZERO" case it stopped when the yield load exceeded twice the yield load of the original bone model or the model reached an oscillation near that target load.

Throughout the simulations, we tracked the evolution of the structure by recording cement volume, bone stiffness and bone yield load for each iteration. Stiffness was calculated as the load over the average vertical displacement of the loaded nodes. Yield load was predicted by assuming linearity between strains and scaling the force up until 1% volume of the bone elements reached the yield maximum or minimum principal strain (-0.0427 for compression (minimum) and 0.0299 for tension (maximum) [72]). It must be noted that we were interested in predicting and increasing the *yield* load of the bone and not the final fracture load. While a majority of bone fractures occur as a result of dynamic loadings, the onset of failure can be well predicted using static FE analyses and scaling of the resulting strains [66, 68, 72]. At the end of the simulations, we took record of the final cement volume and pattern and the stress distribution among the cement elements. The hypothesis was that the evolutionary optimization algorithm seeks a solution in which there is a uniform stress distribution among the cemented elements hence all contribute to the overall structural stiffness equally.

4.3 Results

Results of the optimizations are summarized in Table 4.1. With "ZERO" initialization, we had to stop the optimization at an oscillation phase below the target yield load, as increasing the oscillation number further would cause $RR = 0$. Figure 4.1

shows the evolution of the cement pattern for a representative model. Similar end patterns were observed for the rest of the models. "FULL" initialization shows a rapid removal of the elements from the femoral head, as their contribution to the structure is minimal. Also "ZERO" initialization shows that reinforcement of the greater trochanter occurs before that of the neck. The average optimum cement volume (that yields a 100% larger yield load compared to the non-cemented model) was $19.5ml$ for "FULL" initialization. The volume needed for achieving the goal of optimization was proportional to the initial yield load of the femur model.

Table 4.1: Summary of optimizations and models' parameters.

Model No. (Initialization)	# Iterations	Final Cement Volume (cm^3)	Intact Yield Load (N)	Final Yield Load (N)
1 (ZERO)	49	14.8	2250	4225
1 (FULL)	19	11.8		4470
2 (ZERO)	72	18.8	3420	5525
2 (FULL)	12	20.5		6510
3 (ZERO)	42	20.3	3915	6670
3 (FULL)	2	26.2		7460

From the final cement distributions, it can be inferred that optimization suggests the following as optimum cement placement for the applied loading conditions: reinforce the neck area by adding cement around the superior and inferior aspects of the neck close to the cortex and reinforce the greater trochanter by placing cement in the supero-posterior and the lateral parts of the trochanter. With "FULL" initialization, neck augmentation took the form of a "ring" of cement around the neck and cement

elements are rapidly removed from the central areas of the neck. Figure 4.2 shows the cross section of a sample model for a better inside view of the optimized pattern. With "ZERO" initialization, the "ring" was not completely formed and the superior and inferior aspects of the neck were augmented separately.

Figure 4.3 illustrates the evolution of cement volume and yield load of a sample model. With "FULL" initialization, there is a large drop in those quantities in the first step, as there are a large number of unnecessarily cemented elements being discarded.

We also investigated the relationship between the amount of the cement introduced in the femoral structure and its yield load. Figure 4.4 shows those data pooled for the two initializations for a sample specimen. Load initially increases linearly as the volume increases and eventually reaches a plateau as the cement volume reaches its maximum allowable amount, i.e. the entire volume of the proximal femur.

Finally Figure 4.5 shows stress distribution among the cemented elements for "FULL" initialization at the beginning and at the end of the optimization. A large portion of cement elements undergo very small stress at the beginning, while the majority of those elements are under a relatively large stress in the optimized model.

4.4 Discussion

Femoroplasty is a potential treatment for preventing hip fracture in osteoporotic femur, but is still far from clinical application. Cement placement requires precise

planning to achieve the desired outcome, if small amounts of cement are to be used. We used available finite element models of osteoporotic femur specimens and a modified version of the evolutionary structural optimization technique to optimize cement placement in femur models.

The three optimization simulations "sculpted" the cement in the same qualitative manner. They suggest augmentation of the postero-superior part of the greater trochanter and the neck area close to the cortical shell. By closer examination, one can notice the thicker augmentation in the superior aspect of the neck, compared to the inferior aspect. This is in agreement with the experimental studies on femur [24, 25] that found the initial failure happens at the superior aspect of the femoral neck when loaded in a fall to the side loading configuration.

"FULL" initialization could achieve the yield load while the simulations with "ZERO" initial condition had to be terminated slightly below the target load. This suggest that the "FULL" initialization should be preferred over "ZERO" for our application, as there can be more control over the former compared to the latter. If, for instance, a lower target yield load is considered, one can let the "FULL" initialization evolve for more iterations until it reaches its goal.

There was a uniform stress distribution among the cemented elements of the final optimization result. This validates the hypothesis that the optimization seeks a solution in which all the cement elements contribute to the overall load bearing capability of the bone structure equally. The volume found using the optimizations,

therefore, is the smallest possible that can achieve the optimization goal. It must be noted that the method of BESO, however successful for our application, is a heuristic method and its results are sensitive to the chosen parameters. To tune the parameters—r_0, r_1,a_{RR}, i_0, i_1, and a_{IR}—, several pilot simulations had to be performed to acquire enough experience about this technique. Although we noted the similarity between strain energy-based BESO and gradient-descent algorithms, in the context of the current study, these two haven't been compared. Future work involves using gradient-based optimization techniques for more rigorous results and investigating the similarity between those and the current findings. It is also possible, with other structural optimization techniques, to impose other constraints on the optimizer in order to find a more clinically feasible result. For instance, the optimizer can be prevented from creating a cement pattern with voids inside or a pattern that has too many fragmented cement parts.

Another limitation of the current study is the loading and boundary conditions simulating a mere fall onto the greater trochanter. Stance and walking loads as well as backward falls, although responsible for a smaller portion of hip fractures [98], are other conditions that occur during everyday activities and it is not clear to what results the optimizations would converge under those loading conditions. Furthermore, falls to the side can occur in a number of other orientations and varying internal rotation angles [83, 84, 99]. Our hypothesis, however, is that the qualitative results of the optimizations would be the same, for we predict that yielding starts in

the same area during a fall to the side, also simulated by Ford et al. [84]. This should be verified in the future.

Since the models were subject-specific, there were differences in details of the final cement distribution including the volume of cement. The larger the initial yield load, the more cement was needed to increase that load by 100%. The goal of 100% increase in the yield load to, supposedly, restore bone strength to its original value was set based on the findings of Courtney et al. [33, 100] who suggested that, on average, bone strength reduces in half due to osteoporosis and aging. However, this does not guarantee a zero risk of fracture, as fracture depends on several other factors than yield load as well, including height of fall, floor covering, body weight etc. [101, 102]. To improve the optimizations, simulating falls on a patient-specific model of the body can provide estimates of actual loads exerted on the femur during said falls and those can be used as optimization goals instead.

Simulations showed that relatively small amounts of cement (less than $20ml$) can increase the yield load by as much as 100%. More than twice this amount of cement was used in previous experiments [2–4] and only 30-40% increase in the fracture load was observed. Our results suggest that it is possible to optimize the augmentation in order to reduce the cement volume. However, there were no constraints imposed on the BESO simulations for placement of the cement and, in practice, the optimized plan cannot necessarily be achieved. Among the limiting factors are the fact that cement should be delivered through drilled hole(s) and too many drilled

paths can lead to excessive cortical weakening, reducing the femur fracture load [5]. Furthermore, diffusion of cement through the porous medium of cancellous bone is a complex phenomenon which depends on many factors including cement viscosity and delivery rate [103]. In the following chapters we describe our cement diffusion prediction model and the planning framework that combines the diffusion model with the proposed optimization method for planning of femoroplasty.

4.5 Recapitulation of Contributions

We used a modified version of the method of BESO to optimize the cement placement pattern inside FE models of osteoporotic femur specimens. Results suggest augmentation of the superior and inferior aspects of the neck as well as the lateral and posterior parts of the greater trochanter, which agree with the previous findings regarding regions of first failure in femora due to falls to the side. Differences in the final patterns for different specimens emphasize the need for subject-specific models. Cement elements exhibited a uniform stress distribution which validates the hypothesis that the optimization seeks a solution where all the elements contribute to the structural capacity of the femur equally.

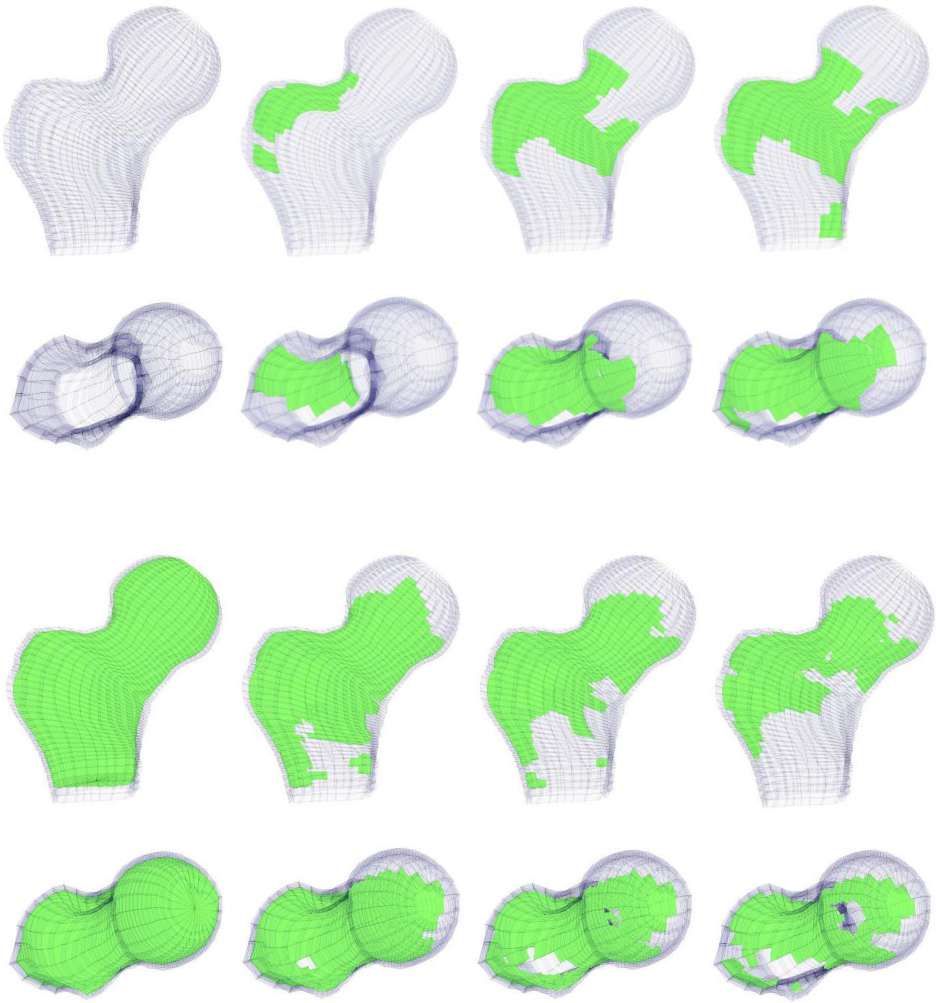

Figure 4.1: From left to right: evolution of the cement placement for "ZERO" (top) and "FULL" (bottom) initializations.

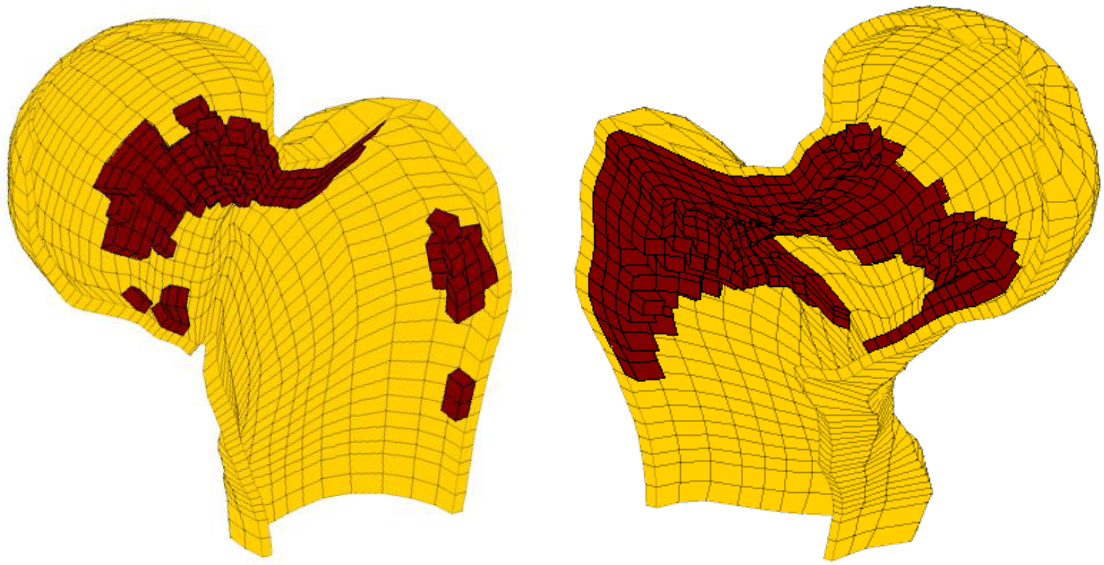

Figure 4.2: Cross section of a representative optimized model. Only the cemented and the outer most bone elements are shown for clarity.

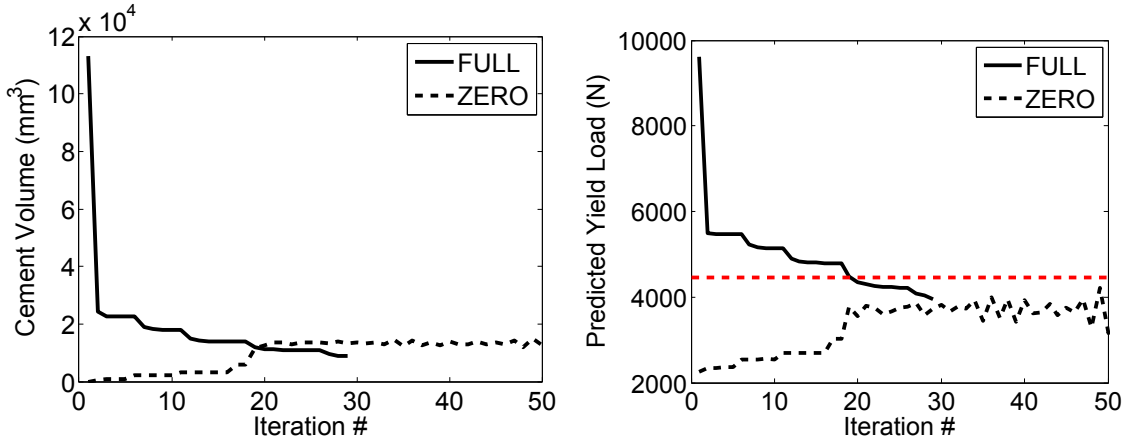

Figure 4.3: Evolution of cement volume (left) and yield load (right) of a sample model with two different initializations. The red dashed line in the second plot represents the target yield load.

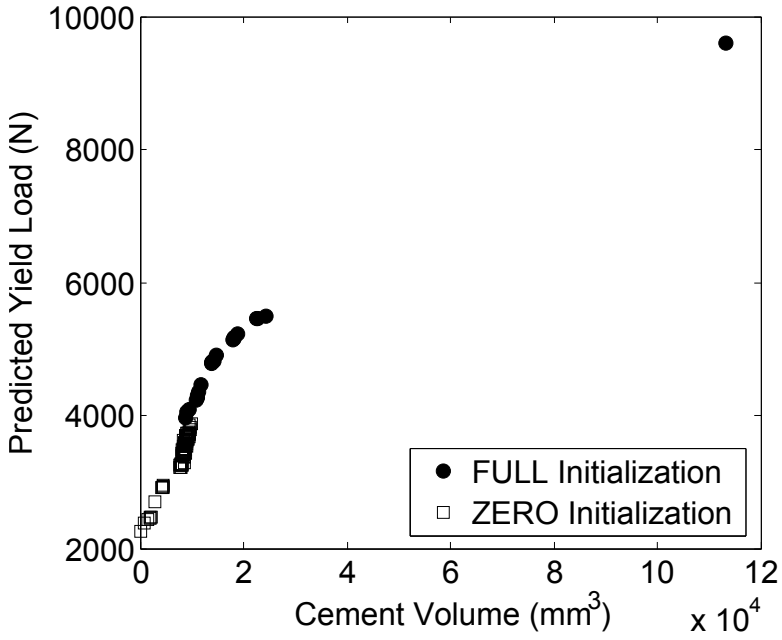

Figure 4.4: Yield load as a function of cement volume for a sample model.

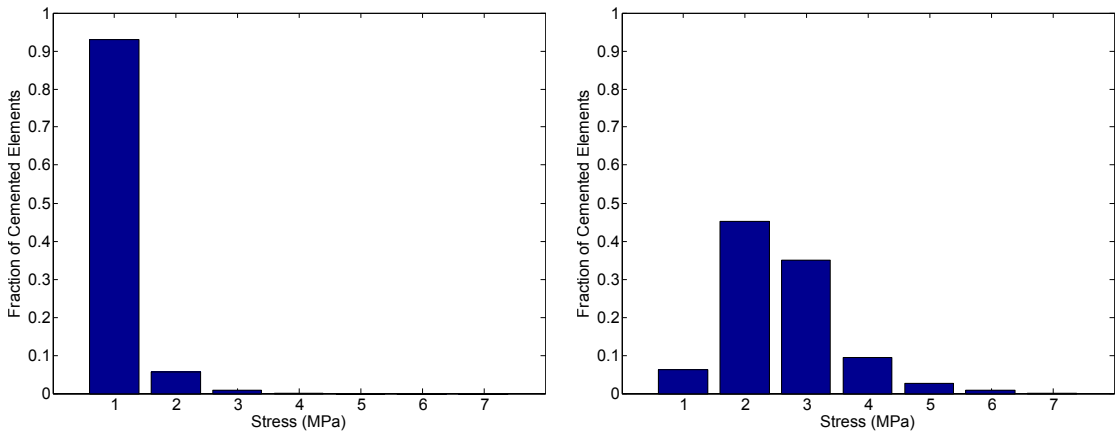

Figure 4.5: Normalized distribution of stress among the cemented elements for "FULL" initialization of a sample model in the first (left) and last (right) iterations.

Chapter 5

Modeling of Cement Diffusion in Osteoporotic Cancellous Bone

5.1 Introduction

Modeling of rheological properties and flow of bone cement has been the topic of research for the past two decades. Among the approaches are finite element [104,105], analytical [106] and heuristic models [107]. In the more recent years, particle models have gained popularity for modeling fluid flows. These models provide a Lagrangian view of the flow, where the simulation (observer) tracks the motion of fluid particles, as opposed to tracking the change of variables inside fixed grid cells in space as in the Eulerian view. Among these models' advantages over grid-based methods are the inherent conservation of mass, no need for creating and maintaining a grid structure

and fast computations of equations of motion. Because of their superior simulation speeds, particle models are of utmost interest in the graphics community and they have been used to model fluids and flow of colloids such as sand [108–111]. Heuristic approaches are taken in these methods to model the particle-particle and particle-environment interactions that best serve the specific application of interest.

An alternative to the empirical particle models is the method of Smoothed Particle Hydrodynamics (SPH), which is a way of approximating continuum field quantities by several discrete particles. First introduced by Lucy [112] and Gingold and Monaghan [113], SPH saw its first application in modeling astrophysical phenomena. Several other SPH applications have been realized since, including modeling of fluid flows such as free surface water simulation [114, 115], melting and viscoplastic objects [116, 117] and porous flow realization [118–121]. In most of the aforementioned works visual aesthetics take precedence over physical realism of the flow and there is usually no quantitative validation using experimental data.

We are interested in predicting the dispersion of viscous cement inside cancellous bone. For this purpose, we used SPH for porous flow modeling. Of particular importance is the capability of the model to predict the end shape that the cement assumes after a certain amount is injected inside a porous medium. We used an implicit numerical integration method to cope with the stability problems arising when modeling highly viscous materials. Hence, in incorporating the Navier-Stokes equations into the SPH formulation, we modified the standard viscosity model to make the formu-

lation computationally more efficient. We tested the model's simulation capabilities in two scenarios: Darcy flow simulation and modeling of bone cement injection in porous media. For the latter scenario, simulation results were compared with experimental data of injection of Polymethylmethacrylate (PMMA) bone cement inside surrogate porous bone models. The following sections describe the formulation and the validation simulations followed by the obtained results. [1]

5.2 Methods

5.2.1 Particle Fluid Model

SPH is a way of interpolating field quantities in discrete particle systems. For these systems, continuous quantities such as velocity or density fields are assumed to be known at some discrete locations (particles) and one can approximate their values in any other given point in space by employing the so-called "smoothing kernel" function W, as in Eq. 5.1 [113].

$$A(\mathbf{r}) = \sum_{j=1}^{N} m_j \frac{A_j}{\rho_j} W(\mathbf{r} - \mathbf{r}_j, h) \tag{5.1}$$

Here $A(\mathbf{r})$ is the field quantity value at location $\mathbf{r}$, N is the total number of particles in the domain, m is the mass of each particle, ρ is the density, W is the smoothing kernel and h is the kernel radius. The smoothing kernel function distributes, in a (small)

[1] This chapter is published as [122].

neighborhood, the field quantities around particles. It is shown that if the function is even as well as normalized, then Eq. 5.1 approximates the field quantities with second order accuracy [114]. Although the integral in Eq. 5.1 should be evaluated for all the particles, the kernel functions are usually designed to have finite support in order to reduce the computational load while maintaining accuracy. Figure 5.1 shows an example one-dimensional smoothing kernel.

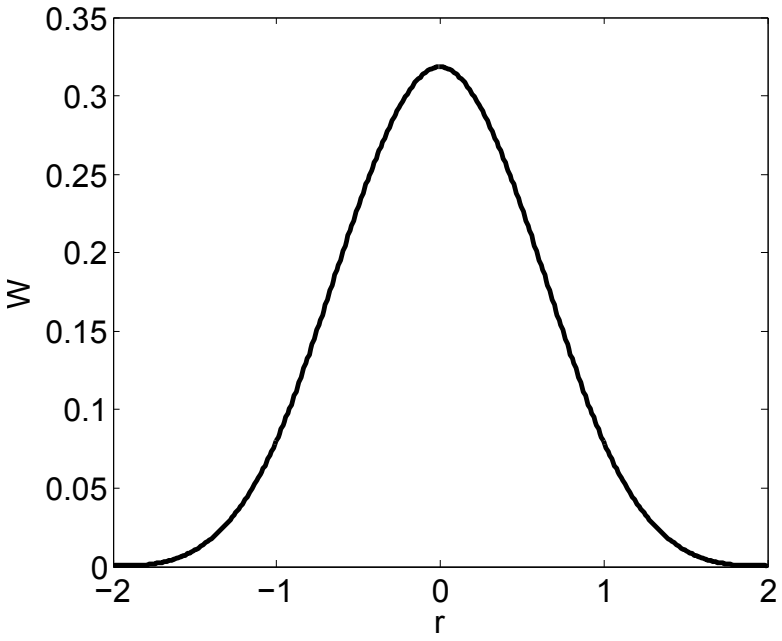

Figure 5.1: An example one-dimensional smoothing kernel function with $r = 1$ and support radius of $h = 2r$.

It is easy to generalize Eq. 5.1 for evaluating derivatives of field quantities as well. In most SPH simulations masses of particles are constant, leading to inherent conservation of mass, so one can evaluate each particle's density using Eq.5.2:

$$\rho_i(\mathbf{r}_i) = \sum_j m_j \frac{\rho_j}{\rho_j} W(\mathbf{r}_i - \mathbf{r}_j, h) = \sum_j m_j W(\mathbf{r}_i - \mathbf{r}_j, h) \tag{5.2}$$

To use the SPH formulation for modeling of fluid flow, the Navier-Stokes equations [123] can be used. The equations for a viscous, incompressible fluid can be written as Eq. 5.3.

$$\frac{\partial \mathbf{v}}{\partial t} + \mathbf{v}.\nabla\mathbf{v} = -\frac{1}{\rho}\nabla p + \frac{\mu}{\rho}\nabla^2\mathbf{v} + \mathbf{f} \tag{5.3}$$

where $\mathbf{v}$ is the velocity vector field, p is fluid pressure, μ is the viscosity and $\mathbf{f}$ is the vector of external body forces (force per unit mass (acceleration)) such as gravity. The left hand side of Eq. 5.3 can be simplified as in Eq. 5.4:

$$\frac{D\mathbf{v}}{Dt} = -\frac{1}{\rho}\nabla p + \frac{\mu}{\rho}\nabla^2\mathbf{v} + \mathbf{f} \tag{5.4}$$

and because of the Lagrangian nature of the particle models, i.e. the assumption that the particles move locally with the fluid flow, the term $\frac{D\mathbf{v}}{Dt}$ can be interpreted as the time rate of change of the velocity of particles. Once all the right hand side terms are evaluated for each particle, its position and velocity can be updated for the next time step in the numerical simulations.

Evaluating the pressure gradient using the standard SPH formula of Eq. 5.1 for derivatives results in non-symmetric pressure gradients [124]. Therefore, we used the symmetric pressure gradient (Eq. 5.5) proposed by Monaghan [124].

$$\mathbf{f}_i^p = -\frac{1}{\rho}\nabla p = -\sum_j m_j(\frac{p_i}{\rho_i^2} + \frac{p_j}{\rho_j^2})\nabla W(\mathbf{r}_i - \mathbf{r}_j, h) \tag{5.5}$$

where $\mathbf{f}^p$ is the pressure gradient force vector. Before Eq. 5.5 can be evaluated for each particle, pressure values must be known. This can be achieved by using an equation of state, in the form of Eq. 5.6 [120, 125].

$$p_i = c_s^2(\rho - \rho_0) \tag{5.6}$$

Using the actual speed of sound (c_s) in the fluids results in very stiff equations that limit the integration time step size prohibitively. Therefore, much smaller values are typically used so that volume is preserved within an acceptable range and computational speed is not compromised [126]. We used a value of $1\frac{m}{s}$—about two orders of magnitude larger than the usual fluid flow velocities that occur during cement injection.

To account for the energy loss due to viscosity, the approximation in Eq. 5.7 is usually employed [127, 128].

$$\mathbf{f}_i^\mu = \frac{\mu}{\rho}\nabla^2\mathbf{v}_i \approx \sum_j m_j \left(\frac{\mu_i + \mu_j}{\rho_i\rho_j \left\|\mathbf{r}_i - \mathbf{r}_j\right\|^2}\right)\left((\mathbf{r}_i - \mathbf{r}_j)\cdot\nabla W\left(\mathbf{r}_i - \mathbf{r}_j, h\right)\right)\left(\mathbf{v}_i - \mathbf{v}_j\right) \tag{5.7}$$

Here $\mathbf{f}^\mu$ is the viscosity force vector. However, as will be explained shortly, we modified Eq. 5.7 to model highly viscous fluids such as bone cement. If one employs a typical explicit numerical integration method, the stability criteria dictate prohibitively small

time step sizes for highly viscous fluids [126, 129, 130]. Working viscosity of bone cement ranges from 100 to $1000 Pa.s$ on average [107, 131], which is several orders of magnitude larger than the viscosity of water (0.001-0.01$Pa.s$) that is usually used in its SPH simulations [119, 120]. Therefore we used the implicit central difference method for integration, summarized in Eq. 5.8:

$$\begin{aligned} \mathbf{v}_i^t &\approx \frac{\mathbf{r}_i^{t+dt} - \mathbf{r}_i^{t-dt}}{2dt} \\ \mathbf{a}_i^t &\approx \frac{\mathbf{r}_i^{t+dt} - 2\mathbf{r}_i^t + \mathbf{r}_i^{t-dt}}{dt^2} \end{aligned} \tag{5.8}$$

where $t - dt$, t, and $t + dt$ represent the previous, current, and future states and $\mathbf{a}_i$ is the acceleration (left hand side of Eq. 5.4). This way the future position of each particle can be found as a function of its previous and current positions. Since the forces acting on the particles are functions of velocity as well as position, this is an implicit problem involving the solution to an equation of the form $M\mathbf{r}^{t+dt} = \mathbf{b}$ where M is a sparse 3N-by-3N matrix, $\mathbf{b}$ is a 3N-by-1 vector, and $\mathbf{r}^{t+dt}$ is the 3N-by-1 vector of positions at time $t + dt$ of all the particles. M is sparse because motion of each particle is affected only by a small number of neighboring particles. In general, solutions to these types of problems are computationally expensive. In the special case of velocity-dependent forces acting on each particle being functions of its own velocity only, matrix M becomes diagonal and the solution can be computed fast. Eq. 5.9 was used to satisfy this criterion,

$$\mathbf{f}_i^{\mu} = -C_f \frac{m_i \mu_i}{\rho_i^2 h^5} \mathbf{v}_i \tag{5.9}$$

where C_f can be adjusted to achieve the desired flow behavior. The viscous force can be interpreted as a force opposing the motion of particles, proportional to their velocity and viscosity. This approximation seems to yield reasonably accurate results for modeling of cement flow inside porous media.

The porous medium was modeled by fixing some of the fluid particles to represent the solid regions [119, 126, 127]. These fixed particles were treated as fluid particles for calculating moving particles' density and pressure, but their density and pressure as well as position and velocity (=zero) were kept fixed over time.

The choice of the kernel function is crucial to SPH simulations. We chose the cubic spline kernel for our density calculations [132]. Here we have $W\left(\left\|\mathbf{r}-\mathbf{r}_j\right\|, h\right) = w_1\left(\frac{\left\|\mathbf{r}-\mathbf{r}_j\right\|}{h}\right)$ with $w_1(q)$ being a kernel with support radius of $2h$ and given by Eq. 5.10:

$$w_1(q) = \frac{1}{\pi h^3} \begin{cases} 0 & 2 < q \\ \frac{1}{4}(2-q)^3 & 1 < q \leq 2 \\ 1 - \frac{3}{2}q^2 + \frac{3}{4}q^3 & q \leq 1 \end{cases} \tag{5.10}$$

The gradient of the cubic spline kernel vanishes at the origin which results in particles clumping together, if used for pressure gradient calculations [114]. Therefore, for pressure calculations, we chose a kernel with non-vanishing gradient as in Eq. 5.11 [133].

$$w_2(q) = \frac{15}{\pi (4h)^3} \begin{cases} 0 & 2 < q \\ (2-q)^3 & 0 < q \leq 2 \end{cases} \tag{5.11}$$

5.2.2 Darcy Flow Simulation

To test the validity of the model, we simulated one-dimensional flow of viscous fluids inside isotropic, randomly porous media and used Darcy's formula to calculate their permeability. Darcy's constitutive equation describes the flow of a viscous fluid through a porous environment. For a steady state, one dimensional flow under constant body force, Darcy's formula reduces to Eq. 5.12 [127]:

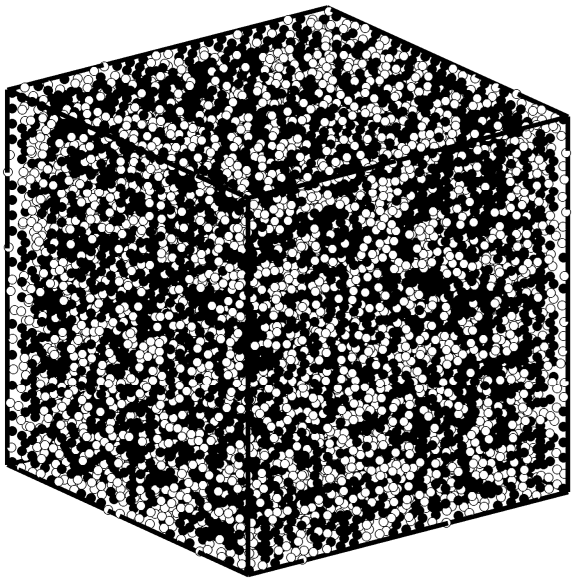

Figure 5.2: Initial particle arrangement for Darcy flow simulation. Black particles represent the porous medium (porosity of 0.5) and white particles represent the fluid.

$$k = -\frac{\mu}{\rho_0 F_B} \langle u \rangle = -\frac{\mu\epsilon}{\rho_0} \frac{\bar{u}}{F_B} \tag{5.12}$$

Here k is the permeability of the porous medium, ρ_0 is the density of the fluid at rest, ϵ is the porosity of the medium, and F_B is the body force acting on the fluid in the direction of flow. Also $\langle u \rangle$ and $\bar{u}$ represent Darcy velocity and the average flow velocity, respectively. To simulate such a flow, particles were initialized in a rectangular grid of the size 25X25X25 particles (Figure 5.2). A number of particles were randomly fixed to the grid, representing the solid regions. Porosity was determined by $1 - \frac{\#fixed\,particles}{\#all\,particles}$ and was varied between 0.5 to 0.9, in 0.1 steps. Particles were assumed to occupy a volume of d^3, with d being the initial particle spacing, and therefore were given a mass of $\rho_0 d^3$ with $\rho_0 = 1.18\,\frac{gr}{cm^3}$. Two initial particle spacings of 0.5 and $1mm$ and two viscosity values of 10 and $100Pa.s$ were simulated. For each setting, particles were initialized and a constant body force was applied to the system. The kernel radius was set to $h = \frac{d}{2}$. Periodic boundary conditions were applied to the model: if in each simulation time step any particle escaped the domain from one side, it was removed from the list and an identical particle was added to the opposite side with the same velocity and density [127]. Sufficient time was given to the simulation for the flow to reach steady state. To avoid edge effects, the average velocity of particles passing through a plane perpendicular to the mid section of the domain was calculated. The ratio of $\frac{\bar{u}}{F_B}$ was determined by the slope of the best-fit line between average velocity and body force. Permeability was then calculated using Eq. 5.12 and

it was converted to dimensionless permeability by employing the procedure described by Jiang et al. [127].

5.2.3 Foam Block Tests

5.2.3.1 Experiments

To further validate the model, we performed injection experiments in a setting similar to osteoporotic bone augmentations with PMMA bone cement, inspired by the experiments of Loeffel et al. [103]. The goal was to perform precisely controlled injections using our in-house cement injection device [134] and compare the results with the corresponding simulations. Eight porous foam blocks (Open Cell Blocks, Sawbones, Vashon, WA) were cut in blocks of approximately 65X65X40mm^3. Each block, representing cancellous bone, was tightly enclosed in a plexiglass shell of 5mm thickness, acting as the cortical shell. On each side of the shells we drilled a 3-mm vent hole, temporarily blocked the holes, and filled the entire combination with melted dairy butter representing the bone marrow [103]. The vent holes provided an escape path for the butter when pressed out by the cement during the injection. Each block was also equipped with eight 2-mm steel balls as registration landmarks. CT scans (Aquilion 64, Toshiba Medical Systems, Japan) were then acquired from the blocks with 0.5mm slice thickness and 0.47mm in-plane resolution and the blocks were refrigerated to maintain solidity of the dairy butter.

The day before each experiment, the blocks to be tested were removed from the refrigerator and left at room temperature for the butter to soften. At the time of experiments, we placed each block on a testing table in the field of view of an X-ray image intensifier (mobile C-arm (OEC9600, GE Healthcare, UK)) and opened the vent holes. To guide the injection device into the center of each block, we used an in-house navigation and tracking system [135]. To facilitate the navigation, each block was equipped with an extension that was used to mount a tracking rigid body (Figure 5.3). The registration was performed by first digitizing the steel balls and recording their coordinates in the tracking system frame. Then, knowing the corresponding coordinates in the CT volume frame, we found the transformation between the two coordinate systems. Using this resulting transformation, the navigation system identified the pre-determined center of the block as the target point of injection, in the tracking system coordinate frame. Spineplex radiopaque bone cement (Stryker Instruments, Mahwah, NJ) was prepared and a 5ml syringe was filled with the cement. A 9-cm, 11G cannula (Stryker Instruments, Mahwah, NJ) was attached to the syringe and the combination was mounted on the automatic injection device. After an initial wait period of ten minutes, cement viscosity was estimated by pressing out the cement with $0.05\frac{ml}{s}$ flow rate for 5 seconds and measuring the average syringe pressure in the last second (the plateau region). The wait time was determined based on our preliminary tests on the cement viscosity at a room temperature of $21°C$ (fixed for all the tests). Hagen-Poiseuille law (Eq. 5.13) was used to estimate the cement

viscosity [103]. The formula relates the pressure drop between two points in a viscous fluid flowing inside a tube to the viscosity and flow rate of the fluid and the dimensions of the tube.

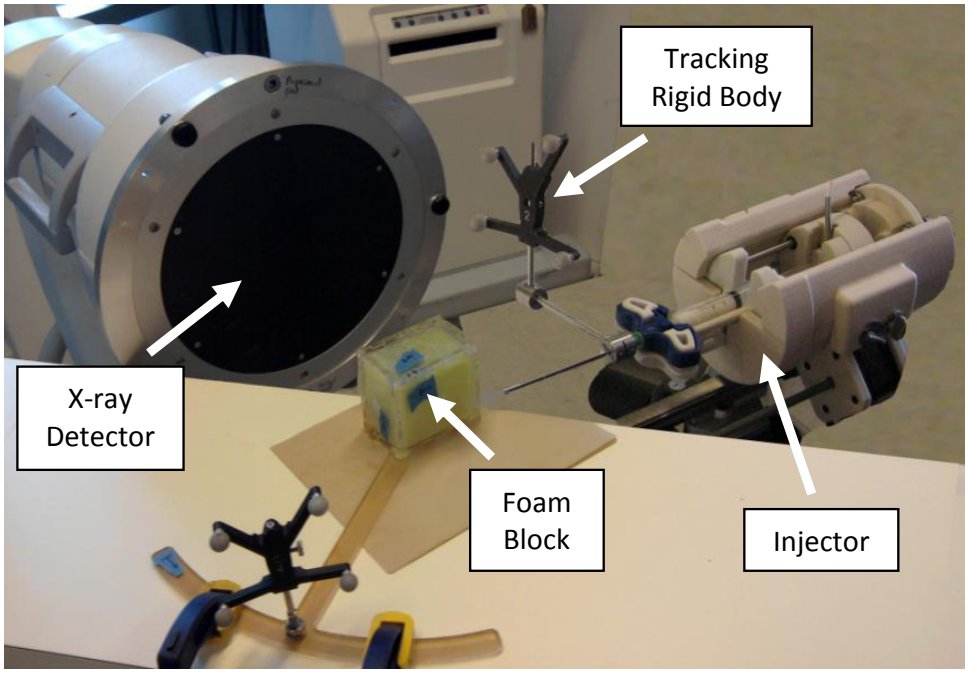

Figure 5.3: Experimental setup.

$$\mu = \frac{\pi D^4}{128LQ}\Delta P \tag{5.13}$$

Here D is the inner diameter of the cannula, L is the length of the cannula, Q is the flow rate of the cement and ΔP is the pressure drop accross the cannula.

Four target viscosity levels of 50, 100, 200 and $400 Pa.s$ were tested. For the two lower viscosity levels, the estimation was done once and the injection time was determined by interpolating the values that were obtained in our preliminary tests.

For the two higher viscosity levels, we performed an additional viscosity estimation, one minute after the first one, for better interpolation accuracy. At this point we guided the needle, using a second tracking rigid body attached to it, to the center of the porous block and the control system started the injection at the time that the viscosity was expected to have reached the desired value. At the same time, the control software started the recording of X-ray video sequence of the C-arm as well as the syringe pressure. An injection rate of $0.05\frac{ml}{s}$ was used until the entire syringe content was injected. Each viscosity level was tested twice, resulting in eight injections. To make the injections with the two higher viscosities possible, we replaced the $11G$ cannula with a 16-cm, $8G$ pipette (Scientific Commodities Inc., Lake Havasu, AZ), as the required pressure was larger.

After the tests, the blocks were scanned again and the resulting CT volumes were registered to those obtained before the tests using intensity-based affine transformations (Analyze, Mayo Clinic, Rochester, MN). The pre-injection CT volume was subtracted from the post-injection CT volume to identify the cement cloud and an isosurface was created from the difference volume to represent the surface of the injected cement. The isosurface was essentially a triangulated mesh that was fit to the surface of the volume composed of the voxels containing cement, and was created using standard functions (MATLAB R2012b, Mathworks, Natick, MA). Also the cement shape in the X-ray images was segmented by subtracting the first image (containing no cement) from the rest of the images in the video sequence.

5.2.3.2 Simulations

To simulate the injections, we employed the SPH method proposed in the previous sections. Pre-injection CT scan volumes of the blocks were loaded and a threshold mask was applied to determine the solid regions within each volume. For each scan, any voxel having a Hounsfield Unit (HU) value of greater than zero was assumed to represent a small solid region and a fixed particle was put at the center of that voxel. Assuming the fixed particles occupy the volume of the voxel V, each fixed particle was assigned a mass of $\rho_0 V$, with $\rho_0 = 1.18 \frac{gr}{cm^3}$ for bone cement [136], the same as the density of fluid particles injected later. Each voxel, based on CT scans acquired, had the dimensions 0.47X0.47X0.5mm^3. To reduce the calculations for an unnecessarily large number of fixed particles, a 40X40X40mm^3 volume located at the center of each block was taken into account. This volume, however, was large enough to ensure it contained the cement at all times. Figure 5.4 illustrates a sample arrangement of the fixed particles.

During simulations, fluid particles were added to the scene at the location of the cannula insertion in the corresponding experiments. The rate of adding fluid particles was determined based on their initial volume and the rate of injection. New fluid particles were assigned an initial velocity $v_0 = \frac{Q}{(\frac{\pi D^2}{4})}$. The states of the fluid particles (total number, positions and densities) were recorded at 1-second intervals, as well as at the end of each simulation. We then used that information to update the CT volumes as if actual CT scans were taken at the time of injections: for each voxel, we

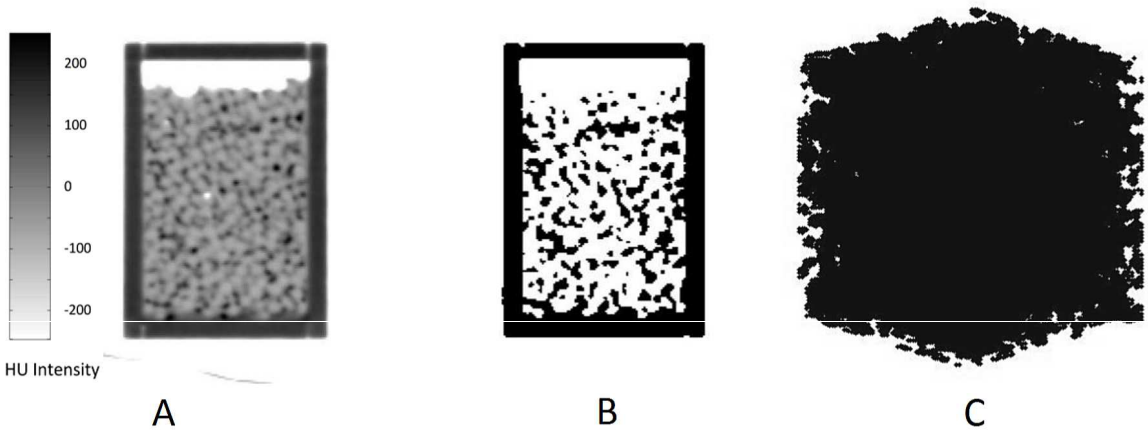

Figure 5.4: Sample original (A) and masked (B) CT slice and an example of fixed particles arrangement (C).

found the neighboring fluid particles and used Eq. 5.2 to determine the fluid density at the center of the voxel. We then increased the voxel HU intensity proportional to the calculated density. A kernel radius of $h = 2r$ was used here, where r is the initial radius of the fluid particles.

Similar to the procedure described before, the pre-injection image volume was subtracted from the simulated one to segment the simulated cement cloud and an isosurface was created. We compared the resulting isosurface with that created from the experimental data as follows [137]: in the isosurface pair, for each point belonging to one isosurface, the closest point belonging to the other isosurface was found and their distance was recorded. For the set of the distances, mean, maximum and standard deviation was calculated. Since the two isosurfaces are likely to contain different numbers of points, this comparison was performed both ways and the larger mean

was taken as the "error" between the two isosurfaces. We also calculated the mean spreading distance of the cement, similar to the 2D approach of Loeffel et al. [103]: for each voxel containing cement in the CT volume, the distance from its center to the location of injection was found and the mean among all the voxels was calculated. This was repeated for all the simulated and experimental volumes and the experiments were compared with the simulations. To compare the pressure profiles of simulations and experiments, we estimated the SPH pressure at several points in the vicinity of the simulated cannula tip (Eq. 5.6) and took the average as the injection pressure. Mean pressure in the first $0.5s$ of simulation was assumed as the "zero" pressure and was subtracted from the subsequent values. This was done to compensate for the erroneous pressure due to the small number of particles in the beginning of the simulations. Also, knowing the viscosity of the cement during the injection as well as the injection rate and cannula geometry, we estimated the pressure encountered by the cement upon exiting the cannula in the actual experiments. Pressure values were then normalized by the maximum value found in the eight experiments. We compared the temporal pressure profiles and the final values between the simulations and the experiments. Finally, we created Digitally Reconstructed Radiograph (DRR) images [42] from the simulated image volumes of the blocks during the SPH simulations. Similar to the X-ray images, we segmented the simulated cement in the DRRs by subtracting the first DRR image from the rest of the images. The resulting images were then compared to the segmented X-ray images.

To determine how fluid particle size affects the accuracy, we performed several of the aforementioned simulations for two sample extreme viscosity levels, changing the initial radius of the fluid particles. We chose values of 1.00, 0.75, 0.57, 0.50 and $0.45mm$ for the particles radius and performed the simulations and compared the results with the experimental data as described before. Particle size below which there was no significant improvement in the accuracy was used for the rest of the simulations to avoid unnecessarily costly computations.

5.3 Results

First we show the results of the benchmark simulations performed to compare the performance of the current model and literature data. Figure 5.5 shows the resulting Darcy velocity for various body forces applied to the fluid. The plot corresponds to the fluid with viscosity of $10Pa.s$ and initial particle spacing of $0.5mm$. Other viscosities and particle sizes showed a similar trend. The slope of the best line fit to the points was used to determine $\frac{\bar{u}}{F_B}$ in Eq. 5.12 for calculating permeability.

In Figure 5.6 permeability is plotted against porosity, both for the results of the current study and values from the literature [127, 138, 139]. Simulations closely follow the trend of the data from the literature. The agreement is better in the interval of 0.7-0.9 of porosity.

Figure 5.7 shows the effect of the particle size on the final cement cloud shape

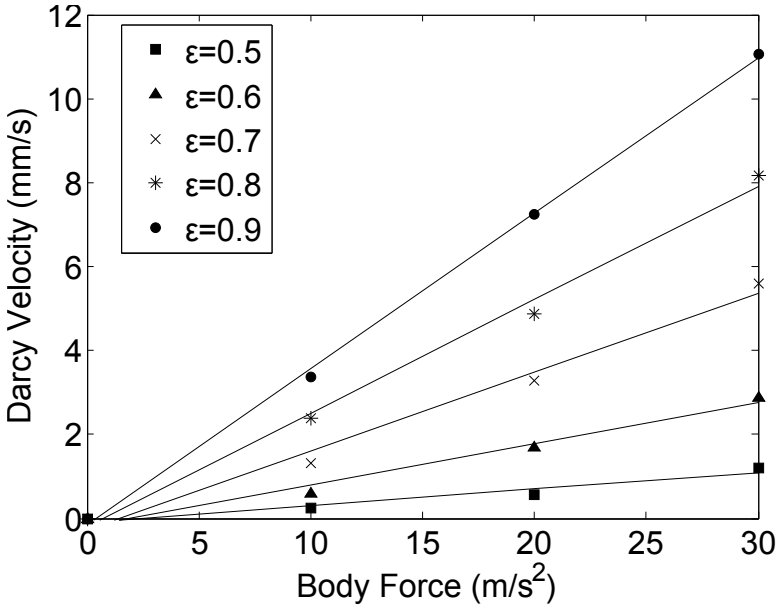

Figure 5.5: Representative steady-state Darcy velocity as a function of body force for various porosities.

for the foam block tests. The simulated isosurfaces are compared to the isosurfaces extracted from the post-operative CT image volumes acquired from the blocks. Reducing the radius of the particles below $0.57mm$ has almost no effect on the accuracy of the resulting cement cloud for either of the viscosity levels. Therefore this particle size was used for the rest of the simulations.

Figure 5.8 compares the simulated and real cement shapes for the eight experiments. Near-millimeter accuracy was achieved in all simulations. The average of all the mean errors is $1.04mm$. There is no evident trend of change in the error as the viscosity increases and this shows the consistency of the simulations for various viscosity levels.

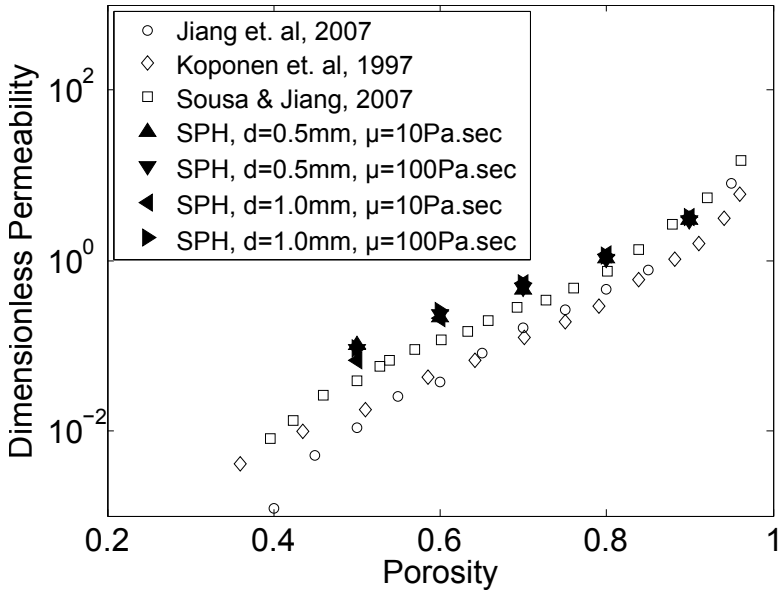

Figure 5.6: Dimensionless permeability vs. porosity.

Figure 5.9 shows comparisons between simulations and experimental values of the mean spreading distance and normalized end pressure. Strong correlations were found between simulated and experimental values. Spreading distance drops significantly when increasing the viscosity from 100 to $200Pa.s$, while pressure shows a leap when increasing from 200 to $400Pa.s$.

Figure 5.10 shows example pressure profiles for the two extreme viscosity cases of 50 and $400Pa.s$ and compares the trends observed in simulations and experiments. Simulated pressure profiles closely resemble those observed in the experiments. Same trends were seen for the other tests.

Sample slices of the post-operative and simulated CT volumes for two example injections with extreme viscosities are shown in Figure 5.11. The figure shows, qual-

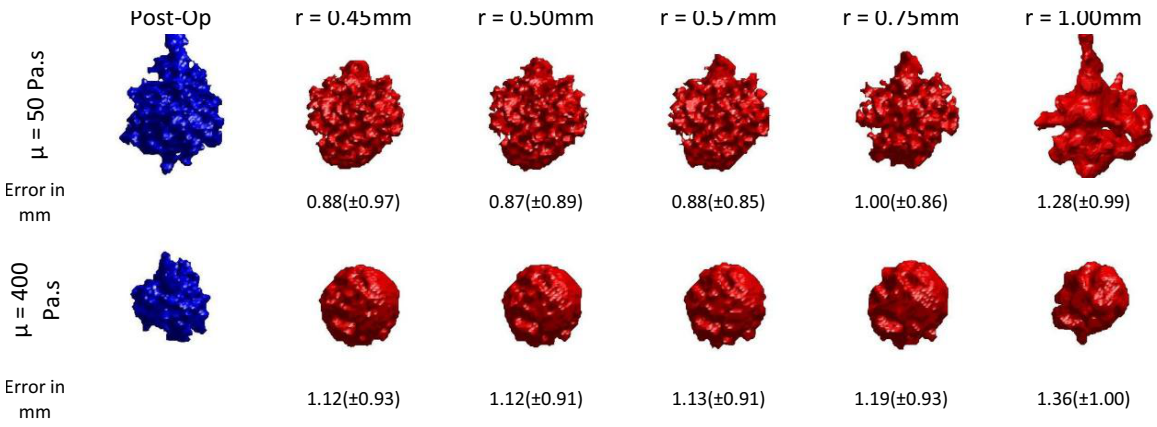

Figure 5.7: Effect of particle size on the accuracy of the cement cloud for two extreme viscosity levels of the foam block tests.

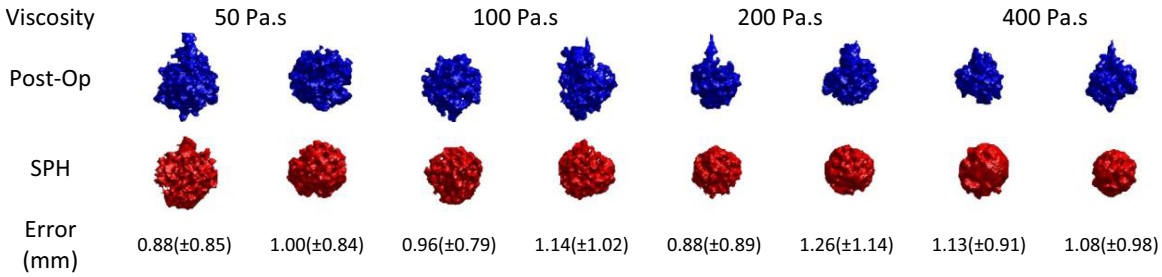

Figure 5.8: Comparison between isosurfaces of post-operative CTs and simulated image volumes for foam block tests.

itatively, the different spreading patterns of high and low viscosity cement inside the porous block. Cement with higher viscosity has created a compact shape, while the one with lower viscosity has more articulations and voids when spreading inside the porous foam block. These features were captured closely by the simulations.

Finally Figure 5.12 shows snapshots of the X-ray image video sequence captured during injections with the two viscosity extremes and compares those with DRR

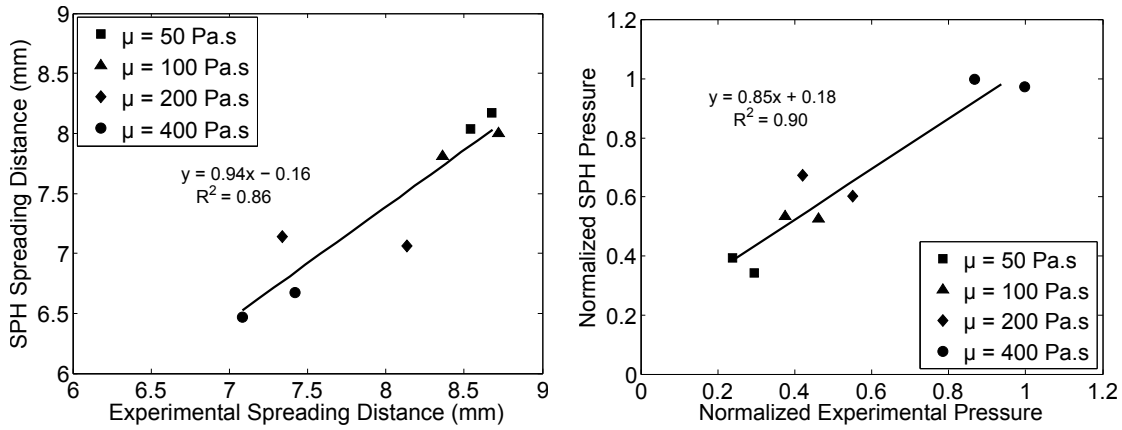

Figure 5.9: Comparison of mean cement spreading distance (left) and normalized outlet cement pressure (right) between foam block experiments and simulations.

images created from the corresponding simulated image volumes. Again, one can notice the difference between the two injections as the high viscosity cement creates a denser shape while the low viscosity injection, at equal volumes, tends to spread more and create a less compact shape inside the porous medium. The algorithm for creating the DRR images tends to smear out the edges of the cement shapes, as can be seen in the figure. Nonetheless, the simulations exhibit the same behavior as the real cement in terms of the area of spreading as a function of cement viscosity.

5.4 Discussion

Augmentation of osteoporotic femur using PMMA bone cement to prevent or reduce the risk of fracture has been suggested to be an alternative preventive treat-

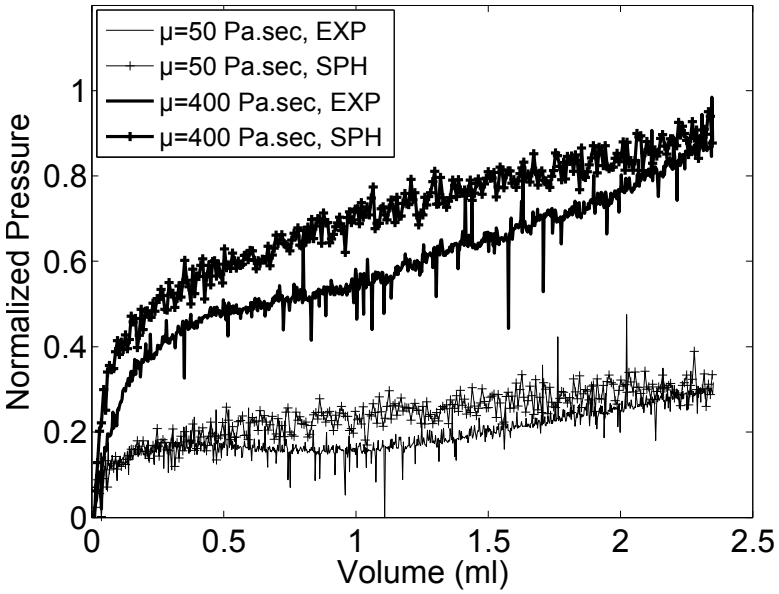

Figure 5.10: Normalized pressure over the course of injection for example viscosity extremes.

ment [2–4]. Because of the possible complications, however, the procedure requires precise planning and execution. Effective planning relies, among others, on an accurate method for predicting the diffusion of the cement through the porous medium of osteoporotic cancellous bone. Our goal was to develop a cement diffusion model and validate its efficacy through simulations and experiments. We chose the method of SPH as it has shown potential for modeling of flow of viscous fluids through porous media. Because of the extreme viscosities involved in injecting bone cement, we chose an implicit numerical integration which forced us to modify the usual approximate viscous force calculations typically performed in SPH simulations.

To validate the model, first we performed simplified one-dimensional porous flow

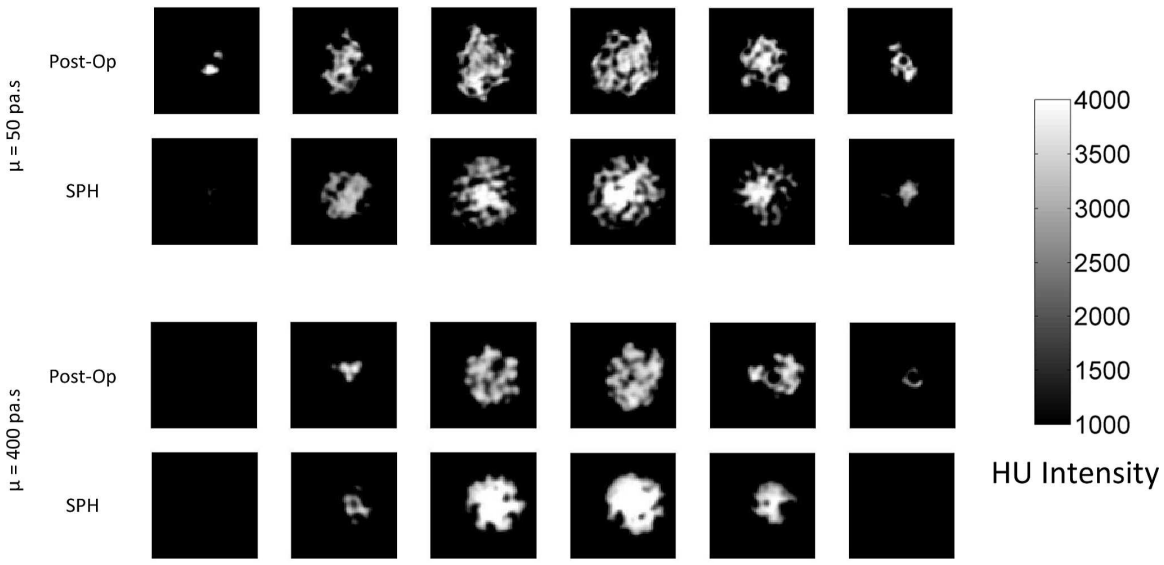

Figure 5.11: Sample slices taken at 5-*mm* intervals from the post-operative and simulated CT volumes.

simulations and compared the resulting dimensionless permeability values with those obtained in similar studies. Close agreement with the data gathered from the literature was observed. The agreement improved especially in the range of porosity between 70% and 90% which, reportedly, includes the range of cancellous bone porosity [131]. The results were independent of particle size and viscosity which is in agreement with the law of Darcy. However, direct comparison between the simulations and published experimental measurements of bone permeability were not possible for two main reasons: a) there is a wide spectrum of permeability values reported for the cancellous bone in the literature and b) converting those values to dimensionless permeability requires precise knowledge of trabecular structure and distribution for the corresponding experiments.

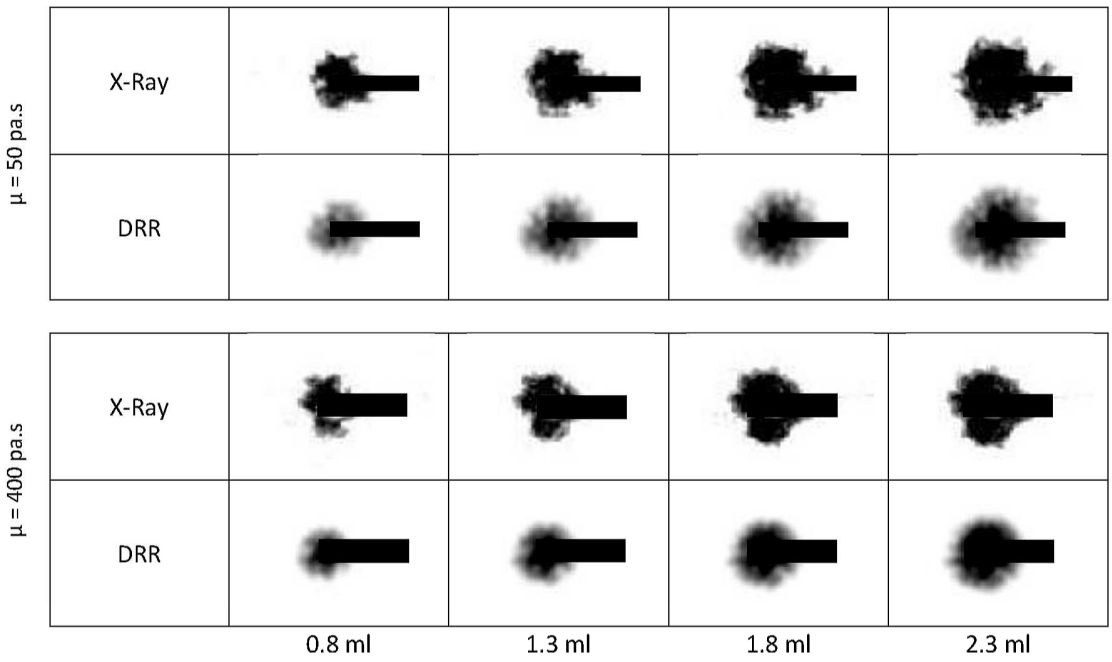

Figure 5.12: Segmented X-ray snapshots and the corresponding segmented DRR images for two extreme viscosity injections. The dark lines represent the cannulae.

For the above reasons, we performed an experimental set of validation tests using commercial porous foam blocks as surrogate cancellous bone tissue and injected medical PMMA cement inside those media in a controlled manner. Four viscosity levels were used and the simulations and experiments were compared together. We studied the sensitivity of the results to particles' initial size and chose the largest particle size that provided the best accuracy. Millimeter accuracy was obtained in reproducing the injected cement shape and there were also strong correlations between experiments and simulations for spreading distance and pressure values. Furthermore same temporal pressure profiles were seen in simulations and experiments.

As mentioned in Section 5.3, increasing the viscosity from 100 to $200 Pa.s$ affected the compactness of the final shape the most, while maximum pressure did not increase by a large factor before increasing the viscosity to $400 Pa.s$. This suggests that a viscosity of close to $200 Pa.s$ is ideal for injections inside porous media including osteoporotic cancellous bone, as the final shape will be compact enough while the required pressure will not be prohibitively large. In the 2D study of Loeffel et al. [103] such large increase in compactness was observed earlier when viscosity changed from 50 to $100 Pa.s$. Of note is that their results were averaged over a larger number of experiments with various porosities and injection rates. Also, there, viscosity was estimated with an injection rate of $0.1 \frac{ml}{s}$ over only 2 seconds, while our tests showed that a plateau in the pressure profile, while estimating the viscosity by pressing out cement, will not be achieved until about 5 seconds after the start of injection, especially for the viscosity levels of 200 and $400 Pa.s$. Therefore their reported values for viscosity might be underestimations. Furthermore, we used the same injection rate for both viscosity estimation and injection tests. In this way we eliminated, at the cannula level, the effect of shear rate-dependence of the viscosity [131] which could affect the viscosity measurements. We also note that the spreading distance values we found (7-9mm) as well as the values reported in the said study (7-10mm) fall within the same small range despite the difference between the dimensions of the two studies.

Our injection tests were performed using only one injection rate of $0.05 \frac{ml}{s}$, as our

hardware limitations prevented us from injecting higher viscosity cement with larger injection rates. However, the study of Loeffel et al. [103] showed that changes in injection rate, at least in the interval of 0.05-0.15$\frac{ml}{s}$, do not have a significant effect on the spread of the cement.

Several factors could contribute to the discrepancies between simulations and experiments. These include model simplifications such as shear rate-independence of the cement viscosity and the linear change of viscosity over time, while it is well documented that commercial PMMA cement exhibits a nonlinear dependence to both shear rate and time, usually captured using a "power law" [131]. The effect of these on accuracy is currently unknown to us. It is worth noting that the proposed model will be used in conjunction with Finite Element Analyses (FEA) to predict the effect of various hypothetical augmentation scenarios on mechanical properties of the bone. The sizes of the elements typically used in FEA are larger than the millimeter accuracy achieved in our simulations [24, 72] and, therefore, FEA accuracy is likely to dominate the overall planning results. This needs to be quantified as part of future studies.

The CT scans were acquired at the highest in-plane resolution possible, which was limited by the size of the blocks and the field of view of the scanning device. We expect that a finer CT resolution would increase the accuracy of the simulation results, noting that the trabecular structure, especially in osteoporotic specimens, is very finely spaced. However, increasing the number of voxels increases the number of

fixed particles as well, and that slows down the simulations drastically. For instance, having voxels with half the current edge lengths will require eight times more fixed particles. With the current resolution our simulations yielded reasonable accuracy and we believe the added computational cost of finer resolution CT would not be justified. Note that fine resolution CT (e.g. μCT) is not usually available in a clinical setting. One must also take into account that the proposed model is intended for use in pre-operative planning of bone augmentations and computational efficiency is of importance, if several simulations are to be performed in order to find the best plan (Chapter 6). It will, however, be instructive to compare the accuracy of our method using a range of CT resolutions from very fine to coarse.

In our simulations we did not take into account the presence of the bone marrow as a fluid that fills the "empty spaces" between the fixed particles and is pushed back by the injected cement. Some pilot simulations proved that taking into account such a fluid will have negligible effect on the end results. This, we hypothesize, is mainly due to the fact that bone marrow viscosity is orders of magnitude smaller than the viscosity of the cement ($< 0.2Pa.s$ for bone marrow [140, 141] vs. 50-$400Pa.s$ for cement in our study) and the interaction between the two fluid particles are minimal. It must be noted that, even without the marrow fluid, our simulations led to reasonable accuracy, therefore we opted to avoid the added computational load of the second fluid particles, because of the reasons discussed above.

The code written for the simulations was not optimized and was executed in a

serial manner. The speed of SPH calculations can be improved by parallelizing the code in an efficient way, exploiting the inherent nature of SPH equations [142].

Results of this study suggest that the chosen method of cement diffusion modeling is an appropriate candidate for our intended application of predicting cement diffusion into porous structure of cancellous bone. This study, to our knowledge, is the first one that quantitatively compares the results, in three dimensions, with those obtained in experiments.

5.5 Recapitulation of Contributions

A particle model based on the method of SPH was used to predict the cement diffusion pattern inside the porous medium of trabecular bone. An implicit numerical integration was used to cope with instabilities related to highly viscous bone cement modeling and viscosity formulation was modified to facilitate efficient simulations. One-dimensinoal Darcy flow was simulated and the results matched those found in the literature. Further validation was done by performing injection tests on trabecular bone surrogates and the corresponding simulations replicated the experimental patterns with relatively small errors. The model can be used to emulate cement injections in osteoporotic bones in order to optimize and plan the surgery.

Chapter 6

Planning of Femoroplasty: Modeling

6.1 Introduction

Femoroplasty has been introduced as a promising alternative to conventional treatments of osteoporosis, in order to reduce the risk of hip fracture in the elderly. Although successful in restoring the diminished mechanical strength of the femur, conventional gross filling of the proximal femur by acrylic PMMA bone cement poses the risk of thermal necrosis as well as stress concentration and / or cement leakage. Therefore cement volume must be kept at a minimum. Achieving substantial improvement in mechanical properties of the bone with limited cement injection calls for computer planning and controlled execution.

In the previous chapters we described the tools that we have developed for evaluation of the biomechanics of the femur, optimization of cement placement, and prediction of cement diffusion pattern inside osteoporotic femur under various conditions. In this chapter we describe how we combined the optimization and cement diffusion modeling methods to plan femoroplasty augmentations on cadaveric femur specimens. In doing so, we took into account the limitations and challenges of the surgical operation. More specifically, finite element optimization using the method of BESO provides a best case scenario for optimized cement pattern. Achieving the pattern in practice, however, is not necessarily possible as there are a number of limitations in placing the cement inside femur. Femoroplasty is intended to be performed as a minimally invasive procedure, therefore the number of injection paths must be kept at a minimum and the short time available to perform the surgery puts a limit on the number of injections within each path. As we describe in the following sections, we used the results of BESO as the goal and employed the particle diffusion model to match that goal in a realistic surgical scenario. This chapter describes the results of our simulations and their implications for successful femoroplasty. [1]

6.2 Methods

Seven pairs of fresh-frozen osteoporotic femur specimens (average neck T-score of -3.53), each pair from one cadaver (four males and three females), were acquired from

[1] A combination of this and the next chapter is presented as [143].

the Maryland Board of Anatomy. Average donors' age, height and weight at the time of death were 81 years, 172cm and 80kg, respectively (Table 6.1). All specimens were CT scanned (Aquilion 64 CT System, Toshiba America Medical Systems, Tustin, CA) at 0.5mm slice thickness intervals. Specimens were kept frozen at $-20°C$ after scanning for future testing, described in Chapter 7. Scans of three of the specimens were used for the simulations described in Chapter 4.

Table 6.1: Specimens' measurements. "Control" denotes the side kept as control and "Aug" denotes the side chosen for planning of augmentation.

Specimen Number	Age (years)	Gender	Weight (Kg)	Height (cm)	Neck T-Score	
					Control (side)	Aug (side)
1	76	M	75	175	-4.10 (L)	-3.90 (R)
2	83	M	127	188	-3.50 (R)	-3.30 (L)
3	68	M	70	175	-4.90 (L)	-4.30 (R)
4	93	F	73	163	-3.70 (R)	-3.70 (L)
5	85	F	66	160	-3.10 (L)	-3.10 (R)
6	87	M	91	183	-2.90 (L)	-2.90 (R)
7	74	F	59	160	-3.10 (R)	-2.90 (L)
Mean (±SD)	81 (±9)	-	80 (±23)	172 (±11)	-3.61 (±0.70)	-3.44 (±0.54)

Planning consisted of two phases: finite element optimization of bone cement placement based on the method of Bi-directional Evolutionary Structural Optimization (BESO), described in detail in Chapter 4, and matching the output pattern, in a local optimization manner, using cement diffusion modeling based on the method of Smoothed Particle Hydrodynamics (SPH) that was presented in Chapter 5.

6.2.1 Cement Placement and Geometry Optimization

To optimize cement pattern inside the femur, we used a modified version of the method of BESO [93] that was described in Chapter 4. We first used the CT scans obtained from the specimens to create finite element (FE) models, according to the procedure described in Chapter 3. From each pair of specimens, we chose one randomly for augmentation. We employed the "FULL" initial condition as that proved to outperform the "ZERO" starting point. The augmented models, as described before, were allowed to evolve until their predicted yield load for each specimen reduced to twice as large as its own non-augmented value. The volume of the cement and the list of the cemented elements were recorded at the end of the BESO simulations.

6.2.2 Matching Optimized Pattern Geometry

We simulated the cement injection procedure to match the ideally optimized cement pattern, while taking into consideration the constraints of intra-operative augmentation. The procedure was as follows:

The BESO algorithm identified the areas in the neck and trochanter in need of augmentation. We divided the proximal femur into three regions as shown in Figure. 6.1. SPH simulations were run at several locations within each region (four for regions 1 and 2, six for region 3). We examined more trial points in the trochanter,

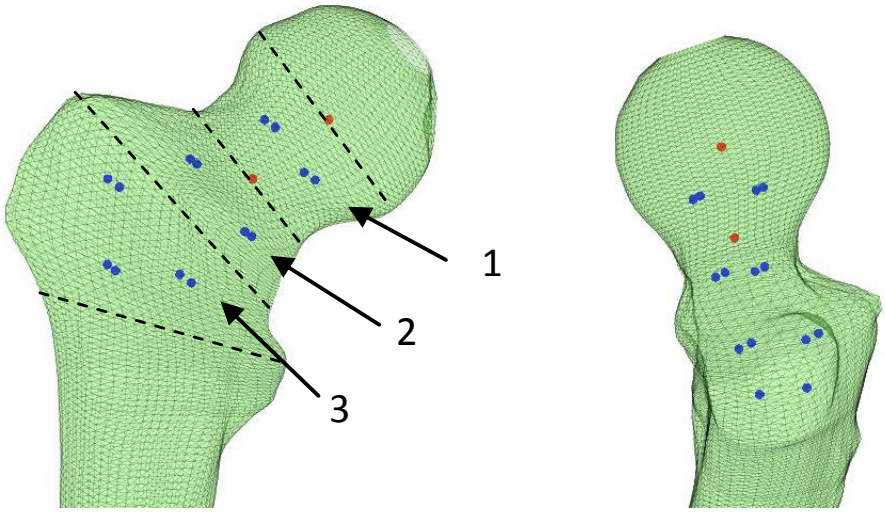

Figure 6.1: Trial points in blue and three regions of proximal femur for injection (1-3). Red dots represent head and neck center points.

because of its larger volume compared to the neck and the head. We also tried to keep the number of SPH simulations at a reasonable minimum since they are computationally costly. We used the SPH model described in Chapter 5.

CT volumes of the femora were used to create a porous model for the SPH simulations. Fixed particles were located at the center of the voxels with HU intensity higher than 200 and were given the volume of a voxel (Figure 6.2). This resulted in an average neck porosity of 90% for the osteoporotic specimens [103]. Fluid particles were then introduced into the model as the simulation progressed. Based on our preliminary experiments with bone cement injection inside porous media, described in Chapter 5, $3ml$ injections were simulated at each location with $0.05ml/s$ injection rate, resulting in a $60s$ injection time. Cement was assumed to have a viscosity of

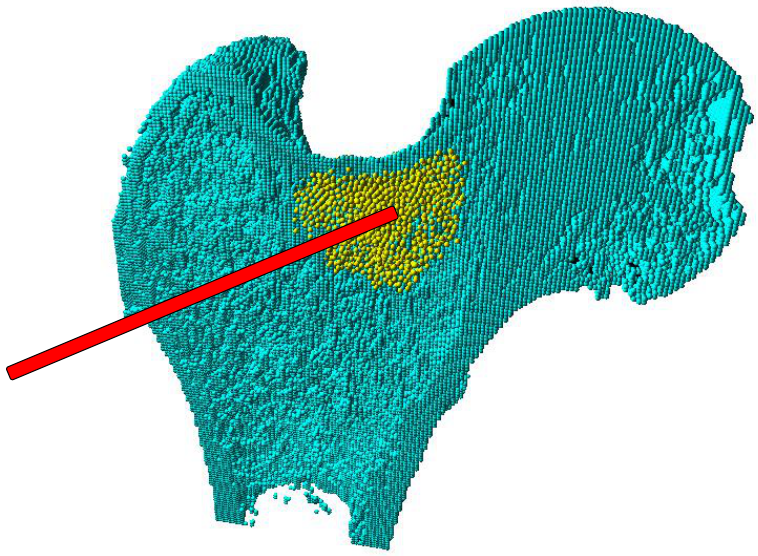

Figure 6.2: Sample cross section of fixed particle (cyan) and fluid particles (yellow) arrangements for SPH simulations. The red line represents the cannula path.

$200Pa.s$, which increased linearly with time to $270Pa.s$ after one minute. This was based on our preliminary experimentation with the PMMA bone cement (Chapter 5). A virtual drilled cannula path was started at the location of injection and directed along a path parallel to the vector connecting the femur head center to its neck center. Fixed particles in the cannula path were removed before each simulation to resemble the "escape" path around the cannula for the fluid particles. After each simulation, the particle information (location and density) were used to update the CT volume as described in Section 5.2.3.2: for each voxel, the fluid density was calculated at the center using the characteristic equation of SPH (Eq. 5.2) and the HU value of the voxel was increased linearly proportional to that value. The updated CT volume was fed back to the FE user interface. Cement distribution in the FE model was then de-

termined by subtracting the pre-injection CT model from the simulated post-injection one and by thresholding. The threshold was manually adjusted so that the volume determined by the FE model matched the simulated cement volume. The cemented element group was compared with the optimal cement pattern and the number of elements overlapping between the two was taken as the "match number" for each injection. After all of the injection simulations in each section (1, 2 or 3) were completed, the simulation with the largest match number was taken as the start point for the next set of simulations in the following bone section. This resulted in three injections overall for each specimen. The corresponding locations for these injections were then manually inspected to determine the drill path(s): If the third location was close to the line connecting the first two, a line was fitted to the set of the three points as the drill path and the projections of the points on the line were taken as the planned injection points. Otherwise, one drilled path was determined as the line connecting the first two points and another one by assuming a line passing through the superior part of the greater trochanter to the third point. If necessary, the injection path was adjusted to ensure it was safely away from the neck cortex. After the line(s) of injection were determined, SPH simulation was repeated for the final plan followed by FE analysis to determine the outcome of the plan. This planning procedure is summarized below. All plannings were performed on a PC equipped with a $3.2GHz$ dual core CPU and $8GB$ of RAM under 64-bit Windows7$^{\text{TM}}$ environment.

- Create the FE model of the bone and analyze the biomechanics prior to plan-

ning.

- Perform BESO simulation and record the final pattern of the cement inside the femur.
- Divide the femur into three regions—proximal neck, distal neck, and trochanter.
- Within each region, select the "test" points. For each point, simulate an injection of cement and use the resulting particle arrangement to update the CT volume and the FE model. Find the test point that overlaps most with the BESO pattern.
- Repeat the previous step for all the regions. For each region, use the updated CT of the previous region (corresponding to the best match point) to create the porous medium.
- Examine the three injection points to determine the line(s) of injection.

6.3 Results

All BESO optimizations converged to a solution and their results are summarized in Table 6.2. Results for Specimens #1-3 are taken from Section 4.3 of Chapter 4. Each BESO iteration took about 200 seconds, resulting in simulations times that varied between 7 minutes and 3 hours. The average optimum cement volume (that doubled the yield load of the models) was $13.4ml$. A strong linear correlation ($R^2 =$

Table 6.2: Summary of BESO optimization end results.

Specimen Number	# Iterations	Cement Volume (cm^3)	Final Yield Load (N)	Intact Yield Load (N)
1	19	11.8	4470	2250
2	12	20.5	6510	3420
3	2	26.2	7460	3905
4	41	5.6	3380	1670
5	36	10.8	4590	2290
6	55	6.3	3590	1485
7	17	12.3	4210	2180
Mean (±SD)	26 (±19)	13.4 (±7.5)	4887 (±1524)	2457 (±888)

0.98) was found between the intact yield load and required volume of the cement (Figure 6.3).

For specimens #1, #2, #3, #5, and #7, the following augmentation was inferred from the optimization for the applied loading conditions: reinforce the neck area by adding a "ring" of cement around the neck and reinforce the greater trochanter by placing cement in the supero-posterior and the lateral parts of the trochanter. An example cross section for such augmentation was shown in Figure 4.2 for better inside view of the pattern. For specimen #4 (left hand side of Figure 6.4), only the superior aspect of the neck and the supero-posterior aspect of the trochanter were augmented. For specimen #6, most of the cement was populated in the superior neck area and almost none of the greater trochanter was cemented (right hand side of Figure 6.4).

Based on SPH simulations and subsequent FE analyses, for specimens #4 and #6 two paths of injection were determined while one line was decided for the rest

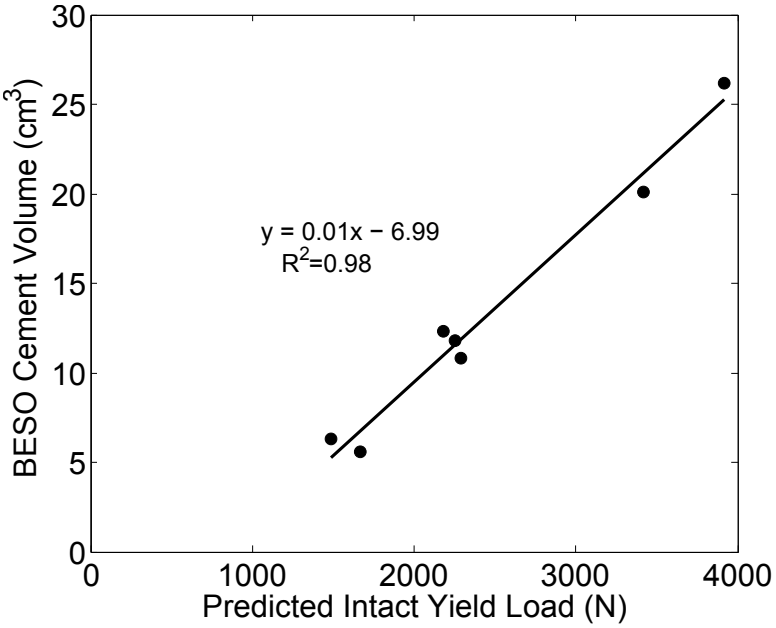

Figure 6.3: Correlation between the intact yield load of the augmented models and the volume required to increase the load by 100%.

of the specimens' models. For specimens #1, #2, #5, and #7 the line was directed from the supero-anterior aspect of the neck to the posterior of the greater trochanter. For specimen #3 the line was directed from the supero-posterior aspect of the neck to the posterior of the trochanter. The first line of injection in specimens #4 and #6 was directed from the superior aspect of the neck toward the lateral side of the trochanter. Figure 6.5 shows example planned injection paths.

Each SPH simulation involved about 110,000 fixed particles that represented the solid regions of the porous medium. 4,000 fluid particles were introduced as the PMMA cement during the injection simulation. This corresponded to 3 hours of computation time, on average. Therefore for each augmentation planning, about 42

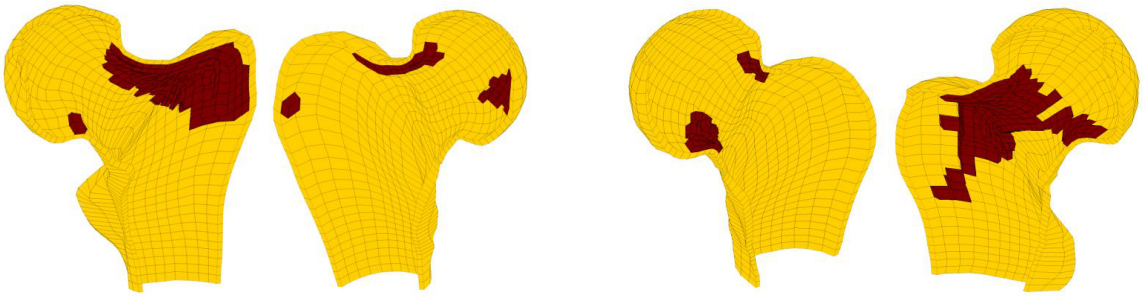

Figure 6.4: Cross sections of optimized models for specimens #4 (left) and #6 (right). Only the cemented and the outer most bone elements are shown for clarity.

hours of computation time was spent. For specimens #4 and #6, however, fewer points were tried based on the BESO and the more localized cement placement, and computation time for those specimens were reduced to 18 hours. The total planning time for each specimen, which includes the BESO simulation time, is presented in Table 6.3.

FE analyses on the models predicted an average yield load of $2343N$ for the control group while the average load for the models selected for augmentation was $2457N$ before augmentation. No difference was found between the two intact groups ($P = 0.379$). The load for augmented specimens increased to $3226N$ and the increase was significant compared to both the control group (+38%, $P = 0.002$) and the intact augmented group (+31%, $P = 0.008$). Table 6.3 summarizes these results.

A strong correlation ($R^2 = 0.86$) was found between the "degree of augmentation", here defined as the ratio of the planned load over the BESO optimized load, and the ratio of the planned cement injection ($9ml$) over the volume of cement suggested by

Table 6.3: Summary of the planning results. Approximate planning times consist of BESO simulations as well as SPH injections and manual operator times. *Percent increases in the means.

Specimen Number	Control Group Yield Load (N)	Augmented Group			Planning Time (hours)
		Augmented Yield Load (N)	%Increase Compared to Control	%Increase Compared to Self	
1	2105	2540	20.7	12.9	45
2	3300	3655	10.8	6.87	45
3	3495	4550	30.2	16.5	44
4	2215	3080	39.1	84.4	23
5	1890	2880	52.4	25.8	45
6	1320	3040	130	105	23
7	2075	2840	36.9	30.3	45
Mean (±SD)	2343 (±779)	3226 (±675)	37.7*	31.3*	39 (±11)

BESO. Figure 6.6 show this correlation.

6.4 Discussion

Femoroplasty can reduce the risk of fracture in the elderly with advanced degree of hip osteoporosis. However, the procedure is still in its research stages and mostly performed on cadaveric specimens, mainly because of its unknown complications including the risk of thermal necrosis caused by large quantities of cement injections, leakage of the cement, and premature fractures as a result of stress concentration. In this chapter, as a proof of concept, we showed that engineering tools can be used for

simulating the biomechanics of the femur for effective planning of femur augmentation. We first used an optimization technique to find the ideally optimum location for placement of the cement. However, there are numerous practical limitations that prevent the surgeon from achieving the ideal plan. Among the limitations are the need for a pre-drilled needle insertion path to inject the cement in the desired location, irregular dispersion pattern of cement into the porous cancellous bone, cortical weakening as a result of multiple drilled paths [5], limited volume available for each injection, limited number of possible injections as each injection limits the space available for the following cannula insertions and injections, etc. Therefore, we employed a particle-based model for simulating cement infiltration of the cancellous bone that we had developed earlier for realistic simulations of cement injection. Results showed that, by employing less than $10ml$ of PMMA bone cement, it is possible to increase the yield load of osteoporotic femora by more than 30%. This is comparable to the outcomes reported in earlier experimental studies of femoroplasty [2–4] where, instead, gross filling of the entire neck and trochanter areas was done using 40-50ml volumes of cement. Our study shows that it is possible, through subject-specific modeling and optimization, to limit the injection volume and potentially avoid the risk of thermal necrosis and stress concentration.

We focused on the fall to the side loading conditions in our study, as those are reportedly the main cause of hip fractures [98]. Also, taking into account that the impact loads due to falls to the side are greater compared to loads due to body

weight and that bone is more vulnerable in fall to the side loading condition [83], one can argue that reducing the risk of fall fracture also lowers the overall risk of injury. However, fractures can occur during normal daily activities such as walking and sitting as well as backward falling. Ideally, the planning should take into account a number of different loading conditions and try to minimize the overall risk.

We employed an ad-hoc procedure to match the BESO results using SPH simulations. To that end, as discussed before, we had to consider the constraints that the surgeon is facing at the time of surgery. Considering all those limitations, there are possibly a number of other methods of approaching the problem of pattern matching that could, potentially, reduce the time needed for planning. Furthermore, reducing SPH simulation times will allow examining more points in the design space and, therefore, improving the planning strategy.

In this study we only allowed a limited volume of cement for the second phase of planning but, as BESO suggested, some specimens needed volumes more than $20ml$ of cement to achieve the goal of augmentation. Performing multiple injections or larger volume injections pose challenges such as excessive pressure required for injecting high viscosity cement and / or leaking of cement into unwanted regions. Robotics technologies [144] can be employed to realize pre-drilling / milling of the target regions inside the bone so that cement can be delivered exactly as the optimized plan.

The relative amount of cement volume used correlated very well with the degree of augmentation in the augmented group. This puts further emphasis on the importance

of subject-specific planning as, for any desired augmentation outcome, different specimens require different volumes of cement augmentation. The volume needed depends, among others, on the size of the femur and the degree of osteoporosis. However, rough measures such as the average BMD or T-score do not contain enough detail information for making such decisions as the location and volume of the cement. FE modeling and optimization, on the other hand, takes into consideration the inhomogeneity and irregular geometry of the bone and can provide more detailed information about the regions of stress or strain concentration in need of reinforcement.

Although we showed the potential of planning femoroplasty, the framework developed in this work can be easily generalized to other types of orthopaedic surgeries where mechanical qualities of bones need augmentation through cement injection, including augmentation of vertebrae and distal radius bones, the most commonly broken bone in the arm,[2] as well as treatment of osteovascular necrosis for the femoral head.

6.5 Recapitulation of Contributions

A method was used to combine the results of BESO on cement placement inside osteoporotic femur FE models and predictions of the SPH model, developed in the previous chapters, to plan femoroplasty operations accordingly. In preparing the plans, surgical limitations including the limited number and volumes of cement available were taken into account. Results of plannings on seven pairs of femora suggested

[2] http://orthoinfo.aaos.org/topic.cfm?topic=a00412

that it is possible to increase the yield load of the femur specimens significantly by strategically placing a small volume of cement at the superior aspect of the neck and lateral and posterior aspects of the greater trochanter.

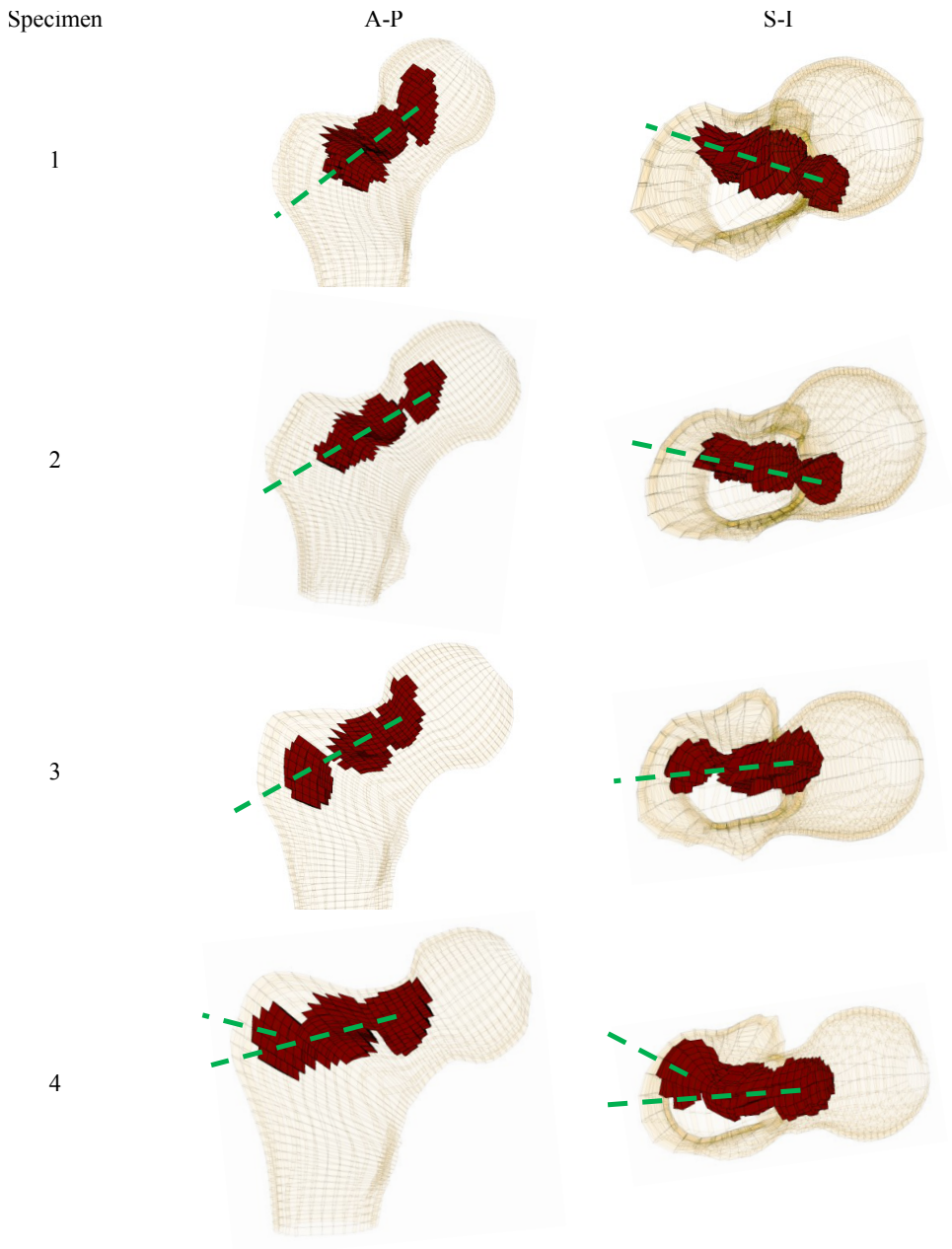

Figure 6.5: Planned paths of injection and placed cement elements for all the specimens. The dashed lines represent the paths of injection. Models' images are mirrored if necessary, either vertically or horizontally, for better comparison. A-P and S-I denote the anterior-posterior and superior-inferior views, respectively.

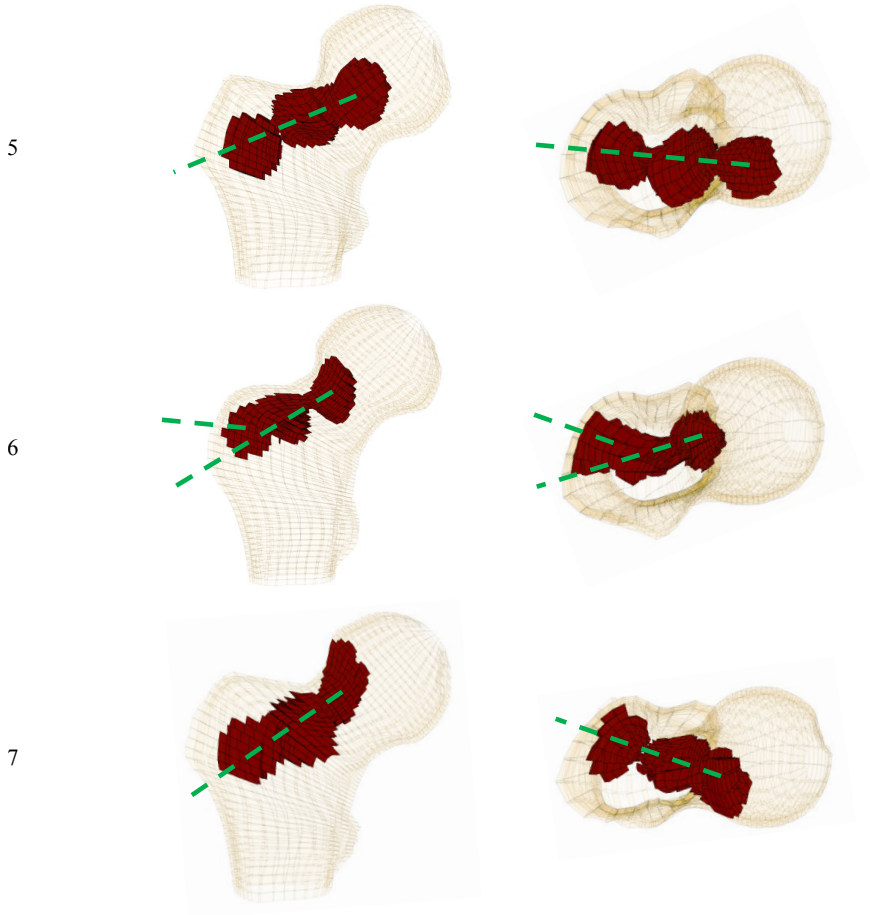

Figure 6.5: (Continued).

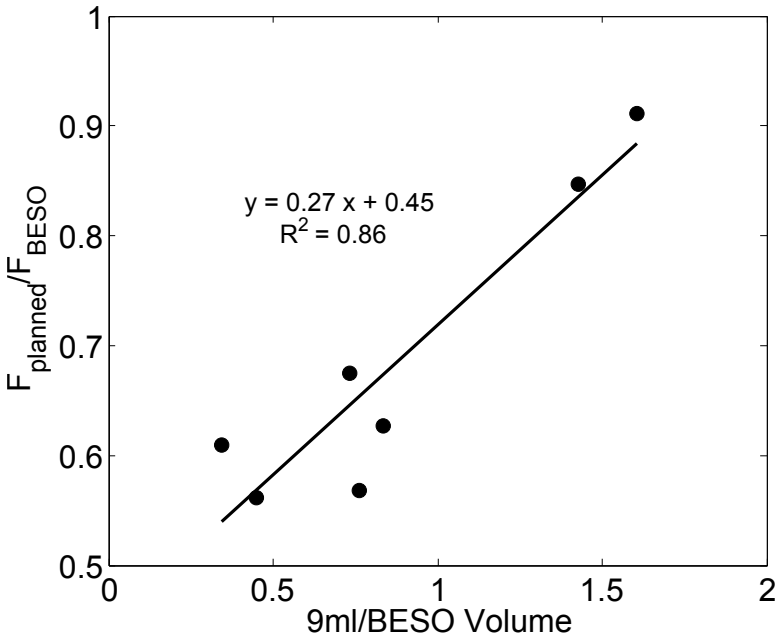

Figure 6.6: Degree of augmentation in the augmented group vs. relative volume of injection.

Chapter 7

Planning of Femoroplasty: Experimental Validation

7.1 Introduction

Femoroplasty is a potential therapeutic treatment for prevention of osteoporotic fractures in the hip [2–4]. It can provide near-term significant improvements to the mechanical properties of the femur bone and can be performed in a minimally-invasive manner for less hospitalization costs and reduced recovery time. However, because of the risks associated with the procedure of injection of acrylic bone cement including thermal necrosis, toxicity of the cement and embolism, it must be precisely planned and executed. In the previous chapter, we described our approach to computer-assisted planning of femoroplasty. In summary we showed that, while introducing

less than $10ml$ of bone cement into the femur (much less than the volumes used in previous experimental studies), it is possible to increase the yield load of the femur specimens significantly. Of course the improvement in the strength was only possible using computer planning. Simulation results and claims made in that chapter need to be validated through experiments, though. In this chapter we describe the experiments we performed on cadaveric femur specimens that were used for planning and compare the results with simulations. We are specifically interested in the augmentation in femora achievable through cement injection as well as the degree to which the simulations and experiments match.

7.2 Methods

7.2.1 Specimen Preparation and Registration

The seven pairs of osteoporotic femora were described in Section 6.2. One day before testing on each pair, they were taken out of the freezer and left at room temperature to thaw out. At the time of augmentation, the remainder of soft tissue was removed from the femora and a tracking rigid body with reflective markers (NDI, Waterloo, ON, Canada) was attached to the femur that was selected for augmentation. We used an in-house navigation system [135] to register the bone specimen in tracking system coordinate frame to its corresponding CT volume frame: first a surface model of the femur was created from its FE representation using a custom software

(MATLAB R2012b, Mathworks, Natick, MA) and three landmarks were identified on the model, i.e. tip of the femoral head, lateral point of the greater trochanter, and tip of the lesser trochanter. After preparation of tracking tools (pivot and axis calibrations), we identified the corresponding landmarks on the femur specimen by use of a tracking pointer tool. Rigid transformation between the two sets of points provided a rough registration between the tracking camera and the CT coordinates. We then picked some surface points on the femur by tracing it with the pointer tool and performed a point cloud-to-point cloud registration using the Iterative Closest Point (ICP) algorithm [145] to refine the registration. Figure 7.1 illustrates the injection setup and registration process.

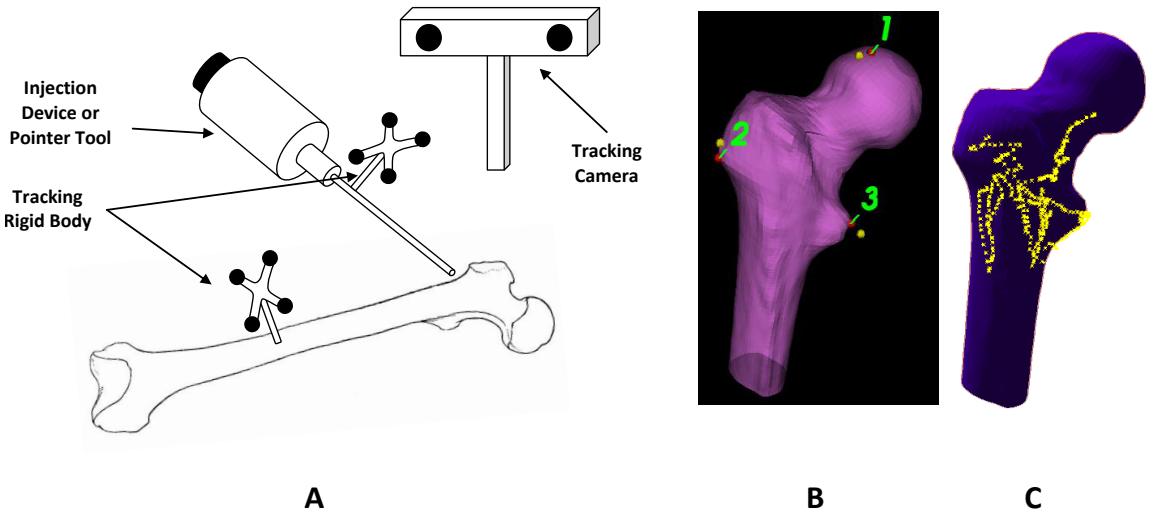

Figure 7.1: (A): Injection setup, (B): Initial registration using the transformation between the picked points (yellow dots) and pre-determined landmarks (numbered red dots), (C): ICP registration results using surface traced points (yellow).

7.2.2 Intra-Operative Augmentation and Mechanical Testing

After the registration, we used a cordless hand drill (DCD760, DeWalt Industrial Tool Co., Baltimore, MD), with a custom attachment for mounting the tracking rigid body, and the navigation system to drill the (first) injection path. The navigation system visually guided the user to the desired location for drilling. We then proceeded to cement preparation: five grams of radiopaque Spineplex (Stryker Instruments, Mahwah, NJ) bone cement powder was mixed with $4.5ml$ of the monomer liquid for about 60 seconds. A $5ml$ syringe was then filled with the cement and a $15cm$, $8G$ cannula (Scientific Commodities Inc., Lake Havasu, AZ) was attached to the syringe and mounted in our injection device [134]. After removing the air and a wait time of 12 minutes from the start of mixing, we estimated the cement viscosity at one minute intervals, as described in Section 5.2.3.1, until it approached the desired value of $200Pa.s$. We then quickly moved the injection system to the desired injection location inside the bone and the system injected, at the appropriate time, the syringe contents at a controlled rate of $0.05ml/s$. Augmentation images were captured using X-ray snapshots at the end of each injection. The procedure of drilling and injection was repeated for all of the planned injections. After augmentation, specimens were CT scanned again and then mechanically tested in a configuration simulating a fall to the side on the greater trochanter [2]. For each specimen, yield load was determined

as the first inflection point of the load-displacement curve obtained from the loading machine. Maximum load was also recorded. Yield and maximum energy were calculated as the area under the load-displacement curve up to the yield and maximum loads, respectively. We then obtained CT scans of the femora after the fracture in order to record the pattern of the fracture.

7.2.3 Data and Error Analysis

The post-injection, pre-fracture CT scans of the augmented specimens were registered to their preoperative counterparts using affine transformations based on mutual information using the 3D Slicer software [146]. FE analysis was performed on the augmented specimen models using those scans to determine the yield load and stiffness. We performed paired sample t-tests for differences in mean between control and augmented specimens, both for FE and measured data sets.

To determine how closely the plans were achieved in practice for augmented femora, we performed error analyses as follows. We assumed two sources of error, simulation and navigation, that cause the cement distribution to differ between experiments and plans. To quantify these error sources separately we first created isosurfaces of the injected and planned cement clouds. We then performed ICP registration between the vertices of the two isosurfaces to register the post-op CT-based cement cloud to the one created using the simulated planned CT volume. This resulted in three distance errors and three X-Y-Z Euler angle rotation errors, namely

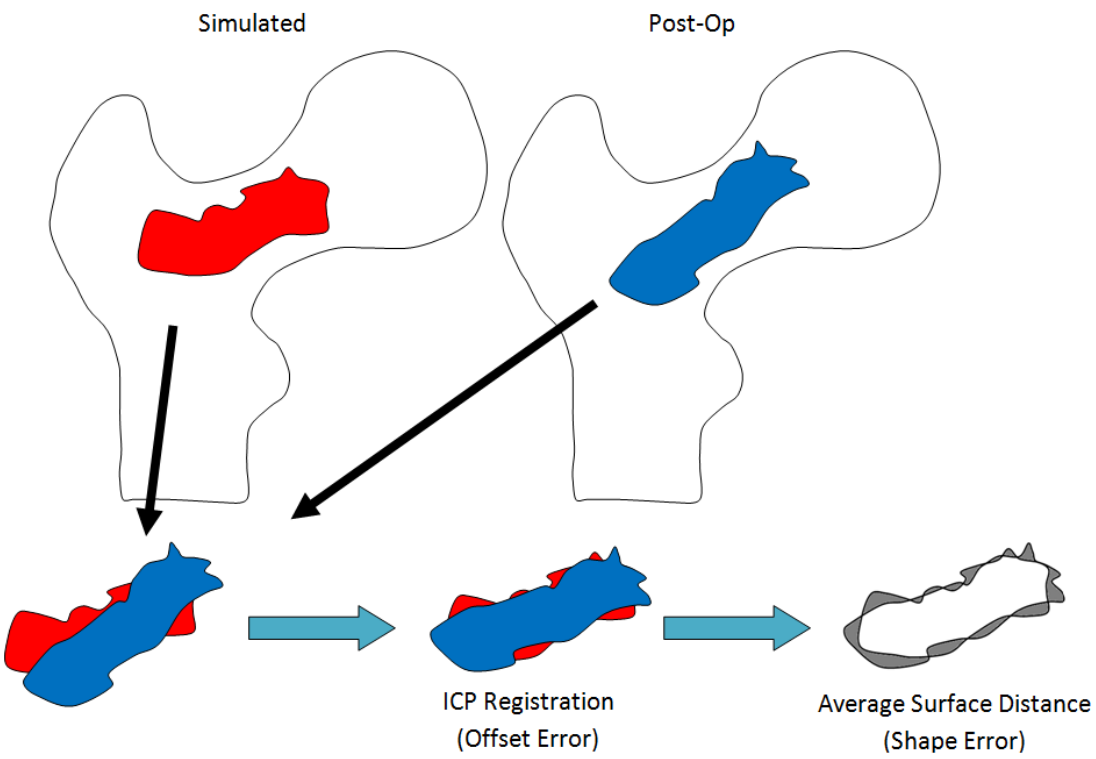

Figure 7.2: Qunatifying intra-operative (offset) and simulation (shape) errors.

ψ, θ and ϕ, representing the cumulative errors occurring in the placement of the cannula during augmentation. We then calculated the mean distance error between the registered isosurfaces by finding, for each vertex on one surface, the closest vertex on the other one and measuring their distance. Since the two surfaces (are likely to) contain different number of vertices, this was done both ways and the larger error was reported as the simulation error, representing the deviation of SPH diffusion simulations from experiments. Figure 7.2 illustrates the procedure.

7.3 Results

At the time of augmentation, for specimens #2 and #5, the first injection failed after about $1ml$ of cement injection, because of hardware malfunction. So we moved the first point of injection slightly toward the trochanter and repeated the injection. On average, $10.0(\pm 1.3)ml$ of cement was injected inside the femora.

Experiments showed that augmentation significantly increased the yield load by +32% ($3176N$ vs. $2410N$, $p = 0.002$), yield energy by +139% ($12.7N.m$ vs. $5.32N.m$, $p = 0.03$) and maximum energy by +96% ($17.8N.m$ vs. $9.09N.m$, $p = 0.003$) in the augmented specimens compared to the control group. There was also a near-significant increase in the maximum load by +25% ($3319N$ vs. $2660N$, $p = 0.06$). An example force-displacement curve for a pair of specimens is shown in Figure 7.3.

FE analyses predicted an average yield load of $2343N$ for the control specimens. For the augmented specimens, based on best plan models, FE predicted a mean load of $3226N$ (38% increase, $p = 0.002$), while FE analyses of post-operative CT scans predicted a mean load of $3076N$ (31% increase, $p < 0.001$). Figure 7.4 illustrates the augmentation outcome based on various measures and Figure 7.5 shows a scatter plot of the measured yield loads against their predicted values. We have summarized the results in Table 7.1.

Error analyses on the iso-surfaces of the cement yielded the following average error numbers for the ICP registration: the three Euler rotation angles were measured as $\psi = 5.53°$, $\theta = 5.74°$ and $\phi = 4.99°$ and the three distance errors were

Table 7.1: Results of femoroplasty. F_y and F_u represent yield and maximum loads in N, respectively and E_y and E_u denote yield and maximum energies in $N.m$, respectively.

Pair Number	Control					Augmented						
	Predicted	Measured				Predicted			Measured			
	Fy	Fy	Fu	Ey	Eu	Fy (Pre-Op)	Fy (Plan)	Fy (Post-Op)	Fy	Fu	Ey	Eu
1	2105	2460	2490	4.98	5.49	2250	2540	2655	2990	2990	10.9	10.9
2	3300	3180	3180	8.78	8.78	3420	3655	3850	4010	4190	14.9	17.8
3	3495	4170	5410	7.95	16.8	3905	4550	4520	4400	4470	29.9	35.2
4	2215	2100	2150	5.91	7.21	1670	3080	2470	3300	3500	12.7	17.2
5	1890	1340	1460	1.89	2.87	2290	2880	2875	2200	2280	5.38	6.68
6	1320	1200	1510	2.23	17.0	1485	3040	2350	1700	2170	3.66	25.0
7	2075	2420	2420	5.51	5.51	2180	2840	2815	3630	3630	11.5	11.5
Mean (±SD)	2343 (±779)	2410 (±1033)	2660 (±1350)	5.32 (±2.60)	9.09 (±5.63)	2457 (±888)	3226 (±675)	3076 (±803)	3176 (±964)	3319 (±887)	12.7 (±8.57)	17.8 (±9.71)

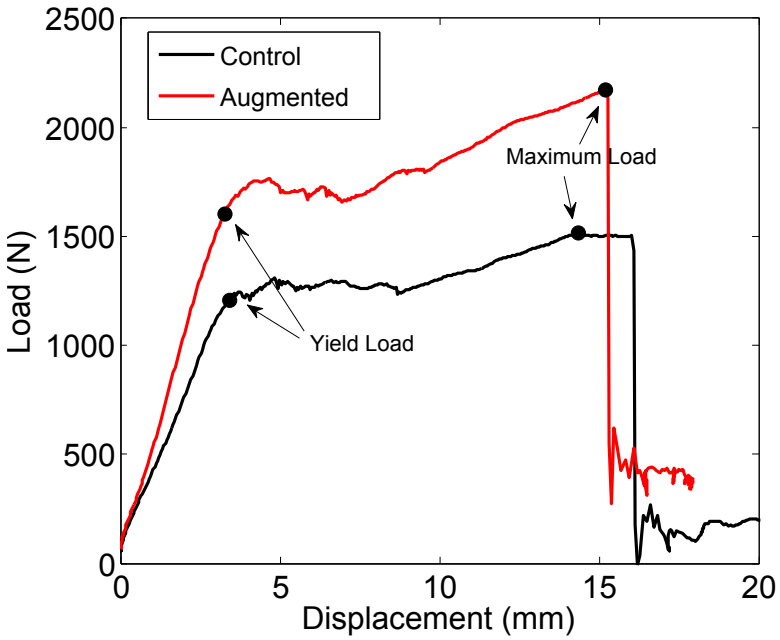

Figure 7.3: Representative force-displacement curves for a pair of specimens.

$\delta X = 2.69mm$, $\delta Y = 3.30mm$ and $\delta Z = 5.34mm$. The total distance error for the ICP registration averaged at $7.27mm$ for the seven specimens. These errors represent the intra-operative error of the injector placement and navigation. The average surface distance error between the two isosurfaces after ICP registration, representing simulations errors, was $1.79mm$. Figure 7.6 shows an example of segmented cement iso-surfaces before and after the ICP registration. Table 7.2 summarizes the individual errors for the specimens.

Table 7.2: Summary of errors. "Intra-Operative Error" denotes the average distance error between the surface model of the femur and the surface traced points after the initial registration during the surgery. Shape errors are defined between the post-operative and simulated cement isosurfaces. ICP errors denote the translations and rotations needed to register the post-operative isosurface to the corresponding simulated one. All distances are in *mm* and all the rotation angles are in degrees.

Specimen Number	Intra-Operative Error	Shape Error *Before* ICP Registration of Isosurfaces	ICP δx	ICP δy	ICP δz	ICP δd	ICP Ψ	ICP Θ	ICP Φ	Shape Error *After* ICP Registration of Isosurfaces
1	1.74	3.54	6.66	3.82	13.3	15.4	3.81	10.3	7.37	1.47
2	0.36	3.43	4.16	3.48	7.99	9.66	4.68	5.17	3.01	2.40
3	0.77	2.11	2.43	2.47	1.73	3.87	2.57	6.81	3.71	1.45
4	0.30	2.58	0.26	4.94	1.62	5.21	0.13	2.81	1.28	1.62
5	0.42	2.45	2.94	0.97	4.30	5.30	4.49	3.36	4.18	1.75
6	0.39	3.41	1.85	4.46	5.37	7.22	15.3	9.79	7.94	2.09
7	0.32	2.50	0.54	2.97	3.03	4.28	7.70	2.00	7.43	1.76
Mean (±SD)	0.61 (±0.52)	2.86 (±0.58)	2.69 (±2.21)	3.30 (±1.33)	5.34 (±4.17)	7.27 (±4.09)	5.53 (±4.88)	5.74 (±3.33)	4.99 ± (2.59)	1.79 (±0.34)

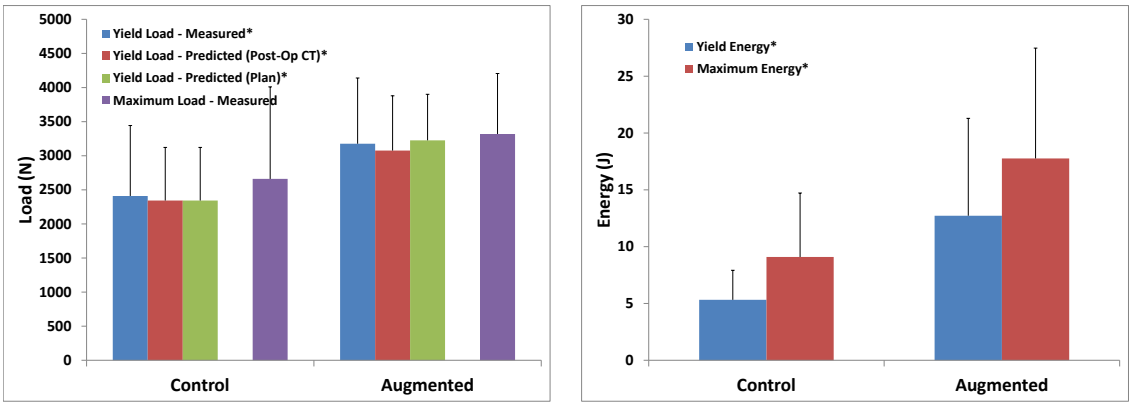

Figure 7.4: Bar plot representations of the effect of augmentation on yield and maximum load (left) and yield and maximum energy (right).

7.4 Discussion

We have developed a comprehensive framework for patient-specific pre-operative planning and execution of femoroplasty. Our goal was to keep the cement injection volume at a minimum to reduce the deleterious effects of its thermal curing and, in the mean time, achieve the best mechanical outcome. Our preliminary experiments on seven pairs of osteoporotic femora showed that we can achieve significant improvement in the mechanical properties of the specimens by injecting about $10ml$ of PMMA bone cement. This is far less than the amounts used in the gross filling technique (40-50ml) [2–4]. Yield load, yield energy and ultimate energy of fracture were all significantly increased as a result of planned femoroplasty.

In one pair (#3), the ultimate load of fracture in the augmented specimen was lower compared to its contralateral control femur. This resulted in an insignificant

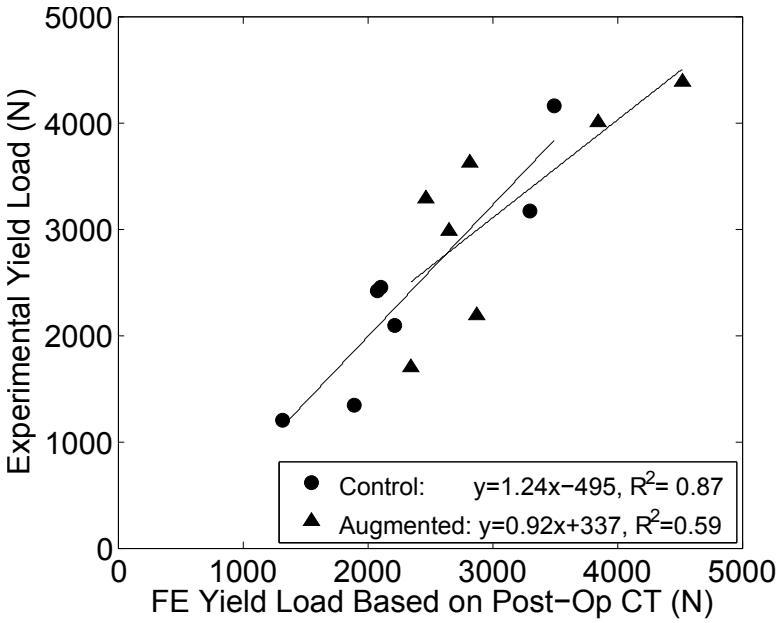

Figure 7.5: Measured vs. predicted yield loads.

increase in the ultimate load. We believe by adding more data to the pool, statistical inferences regarding the ultimate load and other mechanical measures can be improved.

Error analyses on the segmented cement shapes based on simulations and actual post-operative CT scans revealed relatively small errors ($< 6mm$ distance in each direction and $< 6^\circ$ angles on average) in cannula placement and navigation. This demonstrates the fidelity of our navigation system. We note again that the navigation system provided visual feedback to the user who manually moved the drill and subsequently the injector to the desired location and that human error constitutes a large portion of these error numbers. Another source of error would be the registration performed between the camera and the CT coordinate frames. Analyses also

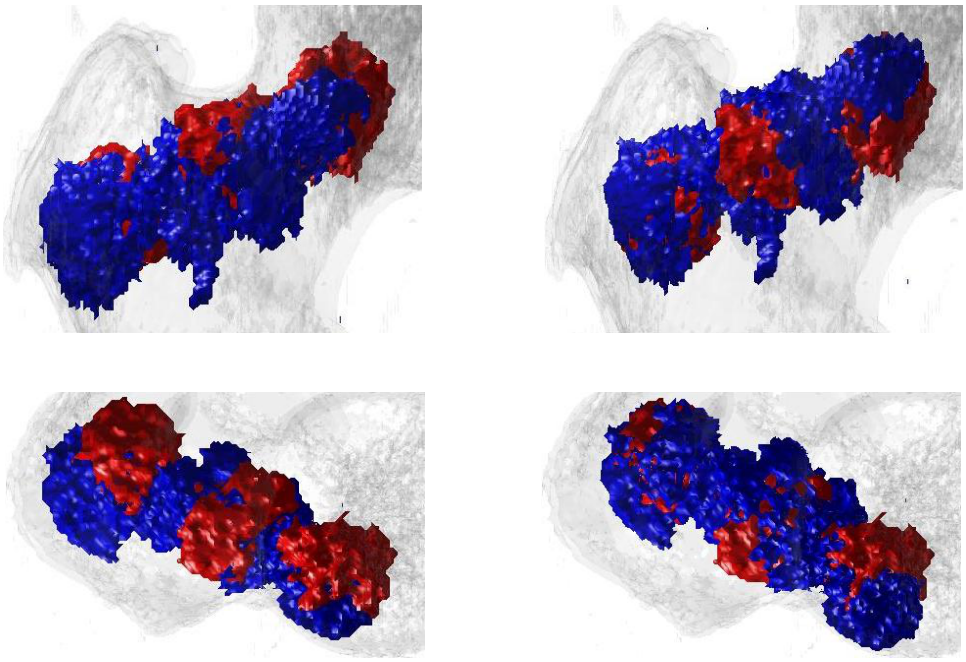

Figure 7.6: Comparison of cement isosurfaces before (left) and after (right) ICP registration. Red indicates the planned cement distribution while blue inidcates the cement cloud obtained from post-operative CT scan.

showed that there was $< 2mm$ shape difference between the simulated and actually injected cement clouds, further validating the diffusion simulation technique. The technique used to separate these two sources of error, however, provides us with an approximation of those errors. A way of more precisely determining the placement error would be to find the location of the tip of the cannula during the surgery using a few X-ray snapshots and 2D / 3D registration methods [147].

Yield loads predicted by the FE analyses according to the best plans closely followed those obtained using post-operative CT scans. Also there was good correlation between the experimental and FE predicted yield loads of the specimens and that

further validates our FE modeling approach.

We hypothesize that by keeping the injection volume to a minimum we managed to avoid thermal necrosis caused by exothermic curing process of the cement. This must be quantified in future tests by monitoring the surface and / or internal temperature of the bone tissue. Attaching temperature sensors to the surface of the femur is straightforward but measuring the internal temperature likely requires more sophisticated protocols and tools.

This chapter presented the first successful attempt for biomechanical planning and navigated execution of the femoroplasty according to the plan. We note that additional experiments are required to validate the approach more, prior to reaching our long-range goal of successful clinical application of femoroplasty as a routine procedure.

7.5 Recapitulation of Contributions

Experimental validation femoroplasty tests were performed on paired femur specimens, according to the plans found in the previous chapter. Femoroplasty was successful in increasing the yield load and energy as well as the maximum energy to failure in augmented samples compared to their control counterparts. This, to the author's knowledge, is the first successful attempt at performing plan-based augmentation of osteoporotic femora with limited volume of cement available.

Chapter 8

Conclusion

8.1 Summary

In this thesis we laid out the different components of a framework for pre-operative planning and post-operative assessment of femoral augmentation using PMMA bone cement. Bone biomechanics was evaluated using a customized FE analysis package that employs diagnostic CT scans for model generation and evaluation. Using the FE models we then optimized the cement placement inside the bone, which assumes an ideal scenario where there are no limitations in creating the desired shape and placing the cement in any location. We then used the idealized optimized pattern as a reference, in conjunction with a particle-based cement diffusion model, to plan the augmentation for cadaveric osteoporotic femur specimens. In doing so, we also took into account the realistic scenario of the surgery and its limitations and challenges.

Augmentation surgeries were performed based on the plans and taking advantage of our in-house navigation and injection systems to deliver the cement precisely according to the plans. Mechanical tests showed that, using only $10ml$ of PMMA cement, we could increase the yield and ultimate fracture loads by 32% and 25%, respectively. Yield energy was increased by a substantial margin of 139%, and the ultimate fracture energy was nearly doubled. These numbers are comparable to similar studies in the literature where, instead, gross filling of femur using more than $40ml$ of cement was employed (Table 2.1). By using a limited amount of strategically planted cement, we potentially reduced the risk of thermal necrosis. Also, because plannings were performed based on optimized patterns, we avoided creating regions of stress concentration as much as possible. The framework developed in this work can be easily extended to modeling and planning other types of orthopaedic operations where mechanical strength of bones need to be augmented through injection of acrylic bone cement (or other augmentation materials with similar mechanical properties) including vertebroplasty and distal radius augmentation.

8.2 Limitations and Future Work

The following is a list of major limitations and possible future directions toward our ultimate goal of making femoroplasty a clinical orthopaedic routine:

- Throughout this work we only took into account the falls to the side loading

conditions. While, as mentioned before, these constitute a major portion of traumatic falls, other loading conditions result in hip fractures in the elderly as well. Patients with advanced degrees of osteoporosis may suffer fractures even while walking normally or ascending / descending stairs. Muscle forces in those cases are enough to initiate a fracture. The optimizations, therefore we believe, can be improved by taking into account several loading conditions. This, of course, means more computational load which can be distributed among several workstations and / or CPU cores in a parallel fashion and then one can combine the individual results into one plan.

- Although we could increase the fracture loads and energies by relatively large margins and reduce the risk of fall fracture, it is not well known to what extent this risk reduction was. As discussed in Section 4.4, we are working on a patient-specific fall model to predict the peak loads that are exerted on an individual's hip and to plan the augmentation accordingly.

- We had a modest sample size of seven pairs of specimens. While, because these samples are paired, our statistical inferences had relatively high power, more samples will lead to better understanding of the nature of augmentations and stronger statistical results.

- Timing of the planning can be improved by using more powerful hardware and more efficient codes. Especially since we are aiming to incorporate the

planning into intra-operative assessment and augmentation strategy update, fast computations of FE and particle models are crucial.

- Internal and external temperature rises due to augmentation were not measured during our experimental tests. We limited the volume of the cement to avoid the deleterious effects of cement curing, as also observed by Sutter et al. [11], but to what extent this has been effective needs to be quantified in future experiments. Monitoring the surface temperature of the specimens is relatively straightforward, but measuring the internal temperature is more challenging and requires precisely planted temperature sensors. However, even with sensors inside the bone, only the temperature in the vicinity of the site of injection can be measured. One idea is to use heat generation models, usually solved using FE modeling, to predict the temperature rises [148–150]. The heat generation and transfer model can also be combined with the optimization and planning module for better outcome.

- Experiments were performed using a subset of the entire system (Section 2.5). While we have most of the components of the full system in place, further work is needed to put all the modules together and test the whole system, including intra-operative assessment of the progress of the surgery and real-time update of the plan.

- Currently an individual femur augmentation surgery time spans a few hours.

This includes the time to prepare the specimen, attach the rigid bodies, calibrate the pointer tools and the drill, perform registration, as well as the time needed for cement preparation and viscosity estimation etc. These times need to be reduced substantially for the system to be suitable for use in a clinical setting. Some of these tasks, e.g. registration and cement preparation, can potentially be performed in parallel. Also, with larger cement volumes per injection, the number of cement preparations and the corresponding viscosity wait times can be reduces. Larger volumes, however, require modifications to the injection system which currently supports only $5ml$ syringes. Larger volumes also correspond to longer injection times and higher viscosity values which demand larger syringe pressures. This poses a design problem that should be tackled in the future.

- To show the safety of the system, *in-vivo* tests on animal subjects have been suggested. These tests need further investigations and thorough considerations in order to ensure a safe and ethically sound procedure, especially taking into account the short amount of time available for live animal testings. These tests can also help investigate the long-term effects of femoroplasty including the risk of thermal necrosis and help us move closer towards the goal of its clinical application.

Appendix A

Dynamic Prediction of Femur Yield Load

A.1 Overview

As mentioned in Chapter 3, (pseudo) dynamic yield / fracture load prediction is an alternative to static analysis and scaling method of prediction. We argued that static analysis performs as well in predicting the onset of yielding for femur bones. To assess the difference between the two methods, the author conducted comparative simulations as described below.

A.2 Formulation

A finite element model of an osteoporotic femur was randomly chosen for this simulation. The static yield load prediction was performed as described in Chapter 3. For the (pseudo) dynamic load prediction, a series of static finite element analyses were performed where the load was gradually increased and the properties of the bone elements were updated at each step. For this purpose, at the end of each iteration, elements were evaluated based on their resulting maximum and minimum principal strains. If for each element the dominant strain (the one with the larger absolute value) exceeded the pre-determined yield strain, an elastic modulus of $1MPa$ and a Poisson's ratio of 0.499 was assigned to the element for the next iteration. Yield strains were set to 0.0299 for tension and 0.0427 for compression, as found in Chapter 3. The load started at $1000N$ and it was increased up to $2500N$, with $100N$ steps. At the end of each step, average femur head displacement and the volume and location of failed elements were recorded.

A.3 Results and Discussion

The static yield load prediction estimated a yield load of $2105N$ for the femur specimen, at which point 1% of the volume of the femur model had failed. Based on the load-displacement curve of the dynamic loading simulations (Figure A.1), the bone yielded at $2100N$. Figure A.2 shows the initiation and spread of the failed

elements up to the yield point, as found in the dynamic simulations. Slightly more (about 1.3%) of the volume of the femur had failed at the onset of yielding.

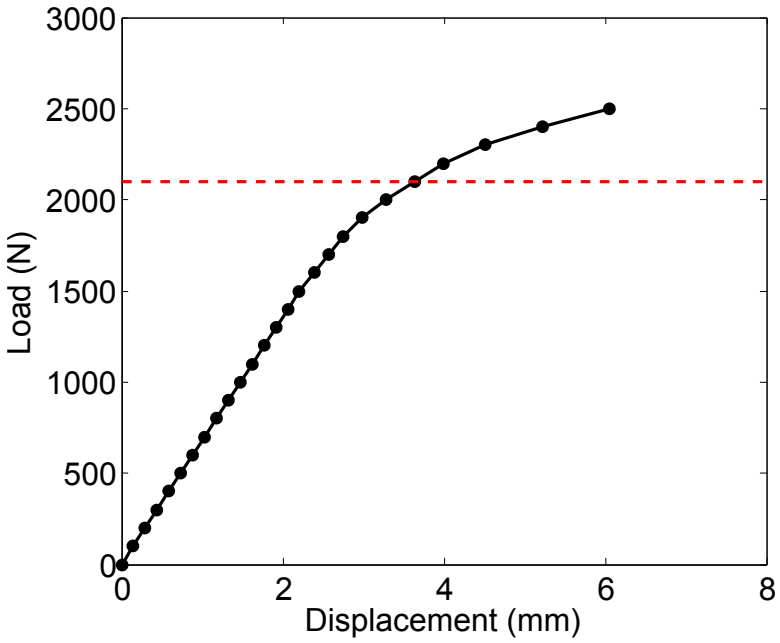

Figure A.1: Load vs. displacement for (pseudo) dynamic loading simulation. The red dashed line represents the onset of yielding.

Figure A.3 compares the predicted location of failure between the static and dynamic simulations. Both methods show the failure in the supero-posterior of the trochanter close to the neck and also superior part of the neck. There are little differences in the location of the failed elements between the two simulations. This supports the hypothesis that a static analysis and then scaling of the strains is sufficient for predicting of the onset of yielding for femur FE models.

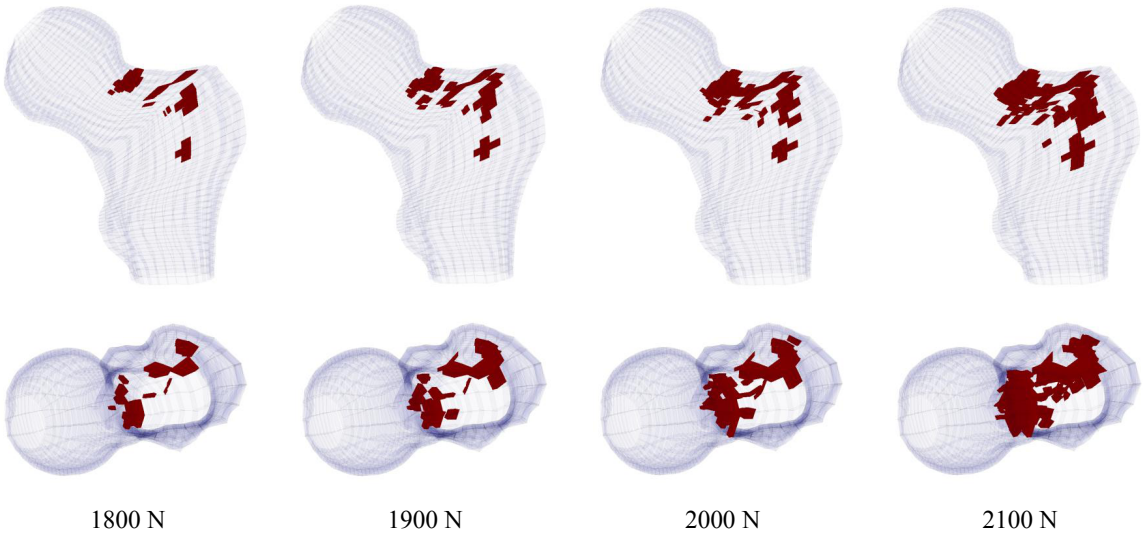

Figure A.2: Initiation and spread of failed elements in dynamic yield load simulation.

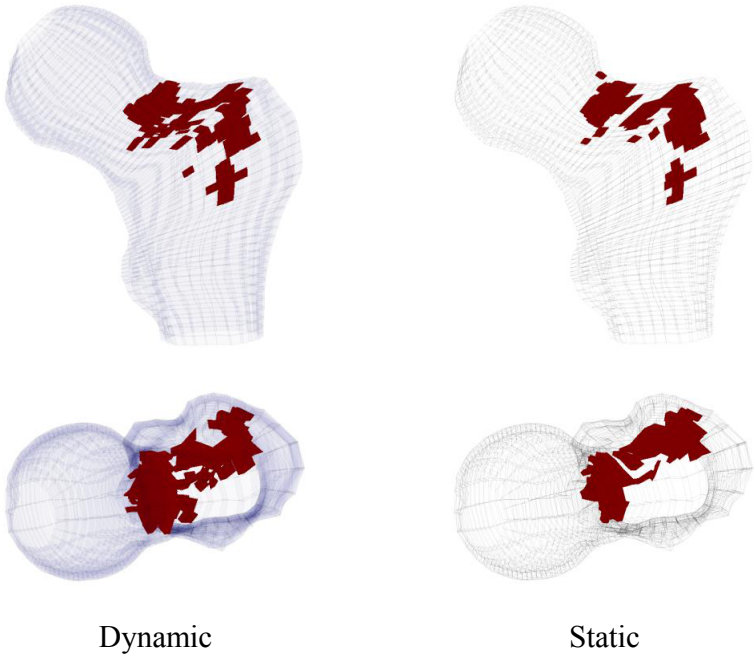

Figure A.3: Comparison between dynamic (left) and static (right) yield location predictions.

Bibliography

[1] J. Lane, L. Russell, and S. Khan, "Osteoporosis," *Clinical Orthopaedics and Related Research*, vol. 372, pp. 139–150, 2000.

[2] E. G. Sutter, S. C. Mears, and S. M. Belkoff, "A biomechanical evaluation of femoroplasty under simulated fall conditions," *Journal of Orthopaedic Trauma*, vol. 24, no. 2, pp. 95–99, 2010.

[3] P. F. Heini, T. Franz, C. Fankhauser, B. Gasser, and R. Ganz, "Femoroplasty—augmentation of mechanical properties in the osteoporotic proximal femur: a biomechanical investigation of PMMA reinforcement in cadaver bones," *Clinical Biomechanics*, vol. 19, pp. 506–512, 2004.

[4] J. Beckmann, S. Ferguson, M. Gebauer, C. Luering, B. Gasser, and P. Heini, "Femoroplasty—augmentation of the proximal femur with a composite bone cement—feasibility, biomechanical properties and osteosynthesis potential," *Medical Engineering & Physics*, vol. 29, pp. 755–764, 2007.

[5] J. Beckmann, R. Springorum, E. Vettorazzi, S. Bachmeier, C. Luring, M. Tin-

gart, K. Puschel, O. Stark, J. Grifka, T. Gehrke, M. Amling, and M. Gebauer, "Fracture prevention by femoroplasty—cement augmentation of the proximal femur," *Journal of Orthopaedic Research*, vol. 29, no. 11, pp. 1753–1758, 2011.

[6] K. Sun, "A finite element approach towards biomechanical optimization of prophylactic vertebroplasty," Ph.D. dissertation, Rice University, Houston, TX, May 2006.

[7] K. Sun and M. A. Liebschner, "Evolution of vertebroplasty: A biomechanical perspective," *Annals of Biomedical Engineering*, vol. 32, no. 1, pp. 77–91, 2004.

[8] P. F. Heini, U. Berlemann, M. Kaufmann, K. Lippuner, C. Fankhauser, and P. van Landuyt, "Augmentation of mechanical properties in osteoporotic vertebral bones—a biomechanical investigation of vertebroplasty efficacy with different bone cements," *European Spine Journal*, vol. 10, pp. 164–171, 2001.

[9] M. A. Liebschner, W. S. Rosenberg, and T. M. Keaveny, "Effects of bone cement volume and distribution on vertebral stiffness after vertebroplasty," *Spine*, vol. 26, no. 14, pp. 1547–1554, 2001.

[10] J. Teo, S. C. Wang, and S. H. Teoh, "Preliminary study on biomechanics of vertebroplasty," *Spine*, vol. 32, no. 12, pp. 1320–1328, 2007.

[11] E. G. Sutter, S. J. Wall, S. C. Mears, and S. M. Belkoff, "The effect of cement

placement on augmentation of the osteoporotic proximal femur," *Geriatric Orthopaedic Surgery & Rehabilitation*, vol. 1, no. 1, pp. 22–26, 2010.

[12] L. Fliri, A. Sermon, D. Wahnert, W. Schmoelz, M. Blauth, and M. Windolf, "Limited V-shaped cement augmentation of the proximal femur to prevent secondary hip fractures," *Journal of Biomaterials Applications*, vol. 28, no. 1, pp. 136–143, 2012.

[13] T. van der Steenhoven, W. Schaasberg, A. de Vries, E. Valstar, and R. Nelissen, "Elastomer femoroplasty prevents hip fracture displacement: In vitro biomechanical study comparing two minimal invasive femoroplasty techniques," *Clinical Biomechanics*, vol. 26, no. 5, pp. 464–469, 2011.

[14] M. J. Goldacre, S. E. Roberts, and D. Yeates, "Mortality after admission to hospital with fractured neck of femur: database study," *BMJ*, vol. 325, no. 7369, pp. 868–869, 2002.

[15] A. M. Schott, C. Cormier, D. Hans, F. Favier, E. Hausherr, P. Dargent-Molina, P. D. Delmas, C. Ribot, J. L. Sebert, G. Breart, and P. J. Meunier, "How hip and whole-body bone mineral density predict hip fracture in elderly women: The epidos prospective study," *Osteoporosis International*, vol. 8, no. 3, pp. 247–254, 1998.

[16] L. Bonnick, "Osteoporosis in men and women," *Clinical Cornerstone*, vol. 8, no. 1, pp. 28–39, 2006.

BIBLIOGRAPHY

[17] O. Johnell, J. Kanis, A. Oden, I. Sernbo, I. Redlund-Johnell, C. Petterson, C. Laet, and B. Jonsson, "Fracture risk following an osteoporotic fracture," *Osteoporosis International*, vol. 15, no. 3, pp. 175–179, 2004.

[18] A. Dinah, "Sequential hip fractures in elderly patients," *Injury*, vol. 33, pp. 393–394, 2002.

[19] J. Stevens and S. Olson, "Reducing falls and resulting hip fractures among older women," *MMWR Recommendations and Reports*, vol. 49, no. RR-2, pp. 3–12, 2000.

[20] WHO, "Assessment of fracture risk and its application to screening for postmenopausal osteoporosis. Report of a WHO study group," *World Health Organization technical report series*, vol. 843, pp. 1–129, 1994.

[21] C. Turner, "Bone strength: Current concepts," *Annals of the New York Academy of Sciences*, vol. 1068, pp. 429–446, 2006.

[22] C. Turner, "Biomechanics of bone: Determinants of skeletal fragility and bone quality," *Osteoporosis International*, vol. 13, pp. 97–104, 2002.

[23] M. R. Karagas, G. L. Lu-Yao, J. A. Barrett, M. L. Beach, and J. A. Baron, "Heterogeneity of hip fracture: Age, race, sex, and geographic patterns of femoral neck and trochanteric fractures among the US elderly," *American Journal of Epidemiology*, vol. 143, no. 7, pp. 677–682, 1996.

[24] D. Dragomir-Daescu, J. O. D. Buijs, S. McEligot, Y. Dai, R. C. Entwistle, C. Salas, L. J. M. III, K. E. Bennet, S. Khosla, and S. Amin, "Robust QCT/FEA models of proximal femur stiffness and fracture load during a sideways fall on the hip," *Annals of Biomedical Engineering*, vol. 39, no. 2, pp. 742–755, 2010.

[25] P. M. de Bakker, S. L. Manske, V. Ebacher, T. R. Oxland, P. A. Cripton, and P. Guy, "During sideways falls proximal femur fractures initiate in the superolateral cortex: Evidence from high-speed video of simulated fractures," *Journal of Biomechanics*, vol. 42, pp. 1917–1925, 2009.

[26] J. C. Lotz and W. C. Hayes, "The use of quantitative computed tomography to estimate risk of fracture of the hip from falls," *Journal of Bone and Joint Surgery*, vol. 72-A, pp. 689–700, 1990.

[27] L. Mortensen, P. Charles, P. Bekker, J. Digennaro, and C. Johnston, "Risedronate increases bone mass in an early postmenopausal population: two years of treatment plus one year of follow-up," *Journal of Clinical Endocrinology & Metabolism*, vol. 83, no. 2, pp. 396–402, 1998.

[28] S. Boonen, M. R. McClung, R. Eastell, G. El-Hajj Fuleihan, I. P. Barton, and P. Delmas, "Safety and efficacy of risedronate in reducing fracture risk in osteoporotic women aged 80 and older: Implications for the use of antiresorptive agents in the old and oldest old," *Journal of the American Geriatrics Society*, vol. 52, no. 11, pp. 1832–1839, 2004.

[29] C. H. Wilkins and S. J. Birge, "Prevention of osteoporotic fractures in the elderly," *The American journal of Medicine*, vol. 118, no. 11, pp. 1190–1195, 2004.

[30] T.-P. van Staa, J. Kanis, P. Geusens, A. Boonen, H. Leufkens, and C. Cooper, "The cost-effectiveness of bisphosphonates in postmenopausal women based on individual long-term fracture risks," *Value Health*, vol. 10, no. 5, pp. 348–357, 2007.

[31] M. Ishijima, Y. Sakamoto, M. Yamanaka, A. Tokita, K. Kitahara, H. Kaneko, and H. Kurosawa, "Minimum required vitamin D level for optimal increase in bone mineral density with alendronate treatment in osteoporotic women," *Calcified Tissue International*, vol. 85, no. 5, pp. 398–404, 2009.

[32] M. Audran, "Drug combination strategies for osteoporosis," *Joint Bone Spine*, vol. 73, no. 4, pp. 374–378, 2006.

[33] A. Courtney, E. Wachtel, E. Myers, and W. Hayes, "Effects of loading rate on strength of the proximal femur," *Calcified Tissue International*, vol. 55, pp. 53–58, 1994.

[34] C. Kessenich, "Nonpharmacological prevention of osteoporotic fractures," *Journal of Clinical Interventions in Aging*, vol. 2, no. 2, pp. 263–266, 2007.

[35] R. Plancarte-Sanchez, J. Guajardo-Rosas, O. Cerezo-Camacho, F. Chejne-

Gomez, F. Gomez-Garcia, A. Meneses-Garcia, C. Armas-Plancarte, G. Saldana-Ramirez, and R. Medina-Santillan, "Femoroplasty: A new option for femur metastasis," *Pain Practice*, vol. 13, no. 5, pp. 409–415, 2012.

[36] A. Polikeit, L. P. Nolte, and S. J. Ferguson, "The effect of cement augmentation on the load transfer in an osteoporotic functional spinal unit," *Spine*, vol. 28, no. 10, pp. 991–996, 2003.

[37] W.-G. Wang, C.-G. Wu, Y.-F. Gu, and M.-H. Li, "Percutaneous osteoplasty for the management of a femoral head metastasis: a case report," *Korean Journal of Radiology*, vol. 10, no. 6, pp. 641–644, 2009.

[38] K. Yamada, Y. Matsumoto, M. Kita, K. Yamamoto, W. Kohda, T. Kobayashi, and T. Takanaka, "Clinical outcome of percutaneous osteoplasty for pain caused by metastatic bone tumors in the pelvis and femur," *Journal of Anesthesia*, vol. 21, no. 2, pp. 277–281, 2007.

[39] E. J. Strauss, B. Pahk, F. J. Kummer, and K. Egol, "Calcium phosphate cement augmentation of the femoral neck defect created after dynamic hip screw removal," *Journal of Orthopaedic Trauma*, vol. 21, no. 5, pp. 295–300, 2007.

[40] T. S. Kaneko, H. B. Skinner, and J. H. Keyak, "Feasibility of a percutaneous technique for repairing proximal femora with simulated metastatic lesions," *Medical Engineering & Physics*, vol. 29, pp. 594–601, 2007.

BIBLIOGRAPHY

[41] M. Armand, R. Armiger, M. Kutzer, C. Brown, S. Mears, E. Sutton, P. Kazanzides, R. Taylor, Y. Otake, O. Sadowsky, and E. Basafa, "Image-guided, robotically assisted osteoporotic bone augmentation," *APL Technical Digest*, vol. 28, no. 3, pp. 216–217, 2010.

[42] Y. Otake, M. Armand, R. Armiger, M. Kutzer, E. Basafa, P. Kazanzides, and R. Taylor, "Intraoperative image-based multiview 2D/3D registration for image-guided orthopaedic surgery: Incorporation of fiducial-based C-arm tracking and GPU-acceleration," *Medical Imaging, IEEE Transactions on*, vol. 31, no. 4, pp. 948–962, april 2012.

[43] R. J. Murphy, "Development and enhancement of computer-assisted hip surgeries for periacetabular osteotomy and femoroacetabular impingement," Master's thesis, Johns Hopkins University, Baltimore, MD, May 2010.

[44] R. S. Armiger, "Development of a surgical guidance system for real-time biomechanical feedback during periacetabular osteotomy," Master's thesis, Johns Hopkins University, Baltimore, MD, May 2006.

[45] J. Lepisto, M. Armand, and R. Armiger, "Periacetabular osteotomy in adult hip dysplasia - developing a computer aided real-time biomechanical guiding system," *Suomen Orthopedia ja Traumatologia*, vol. 31, pp. 186–190, 2008.

[46] M. Armand, R. Armiger, G. Chintalapani, X. Liu, R. Szczepanowski, S. Feng, D. Minhas, R. Taylor, and J. Lepisto, "Computer-assisted hip osteotomy

surgery with realtime biomechanical feedback," in *Proceedings of the 5th Annual Meeting of CAOS-International*, 2005, pp. 8–15.

[47] M. Armand, J. Lepisto, A. Merkle, K. Tallroth, X. Liu, R. Taylor, and J. Wenz, "Computer-aided orthopedic surgery with near-real-time biomechanical feedback," *APL Technical Digest*, vol. 25, no. 3, pp. 242–252, 2004.

[48] M. Lengsfeld, J. Schmitt, P. Alter, J. Kaminsky, and R. Leppek, "Comparison of geometry-based and CT voxel-based finite element modelling and experimental validation," *Medical Engineering & Physics*, vol. 20, pp. 515–522, 1998.

[49] J. Keyak, J. Meagher, H. Skinner, and C. Mote, "Automated three-dimensional finite element modelling of bone: A new method," *Journal of Biomedical Engineering*, vol. 12, pp. 389–397, 1990.

[50] M. Gomez-Benito, J. Garcia-Aznar, and M. Doblare, "Finite element prediction of proximal femoral fracture patterns under different loads," *Journal of Biomedical Engineering*, vol. 127, pp. 9–14, 2005.

[51] M. Viceconti, L. Bellingeri, L. Cristofolini, and A. Toni, "A comparative study on different methods of automatic mesh generation of human femurs," *Medical Engineering & Physics*, vol. 20, pp. 1–10, 1998.

[52] A. Cifuentes and A. Kalbag, "A performance study of tetrahedral and hexa-

hedral elements in 3-D finite element structural analysis," *Finite Elements in Analysis and Design*, vol. 12, no. 3-4, pp. 313–318, 1992.

[53] A. Ramos and J. Simoes, "Tetrahedral versus hexahedral finite elements in numerical modelling of the proximal femur," *Medical Engineering & Physics*, vol. 28, no. 9, pp. 916–924, 2006.

[54] K. Volokh, H. Yoshida, A. Leali, J. Fetto, and E. Chao, "Prediction of femoral head collapse in osteonecrosis," *Journal of Biomedical Engineering*, vol. 128, pp. 467–470, 2006.

[55] A. Natali and E. Meroi, "A review of the biomechanical properties of bone as a material," *Journal of Biomedical Engineering*, vol. 11, pp. 266–276, 1989.

[56] J. W. Vahey, J. L. Lewis, and R. Vanderby, "Elastic moduli, yield stress, and ultimate stress of cancellous bone in the canine proximal femur," *Journal of Biomechanics*, vol. 20, no. 1, pp. 29–33, 1987.

[57] J. Rice, S. Cowin, and J. Bowman, "On the dependence of the elasticity and strength of cancellous bone on apparent density," *Journal of Biomechanics*, vol. 21, no. 2, pp. 155–168, 1988.

[58] M. Ciarelli, S. Goldstein, J. Kuhn, D. Cody, and M. Brown, "Evaluation of orthogonal mechanical properties and density of human trabecular bone from the

major metaphyseal regions with materials testing and computed tomography," *Journal of Orthopaedic Research*, vol. 9, pp. 674–682, 1991.

[59] J. Rho, M. Hobatho, and R. Ashman, "Relations of mechanical properties to density and CT numbers in human bone," *Medical Engineering & Physics*, vol. 17, no. 5, pp. 347–355, 1995.

[60] D. C. Wirtz, N. Schiffers, T. Pandorf, K. Radermacher, D. Weichert, and R. Forst, "Critical evaluation of known bone material properties to realize anisotropic fe-simulation of the proximal femur," *Journal of Biomechanics*, vol. 33, pp. 1325–1330, 2000.

[61] L. Lenaerts and G. H. van Lenthe, "Multi-level patient-specific modelling of the proximal femur. A promising tool to quantify the effect of osteoporosis treatment," *Philosophical Transactions of the Royal Society A*, vol. 367, no. 1895, pp. 2079–2093, 2009.

[62] L. Peng, J. Bai, X. Zeng, and Y. Zhou, "Comparison of isotropic and orthotropic material property assignments on femoral finite element models under two loading condition," *Medical Engineering & Physics*, vol. 28, pp. 227–233, 2006.

[63] V. Baca and Z. Horak, "Comparison of isotropic and orthotropic material property assignments on femoral finite element models under two loading condition (letter to the editor)," *Medical Engineering & Physics*, vol. 29, p. 935, 2007.

[64] J. H. Keyak and S. A. Rossi, "Prediction of femoral fracture load using finite element models: an examination of stress- and strain-based failure theories," *Journal of Biomechanics*, vol. 33, pp. 209–214, 2000.

[65] E. Schileo, F. Taddeia, L. Cristofolini, and M. Viceconti, "Subject-specific finite element models implementing a maximum principal strain criterion are able to estimate failure risk and fracture location on human femurs tested in vitro," *Journal of Biomechanics*, vol. 41, pp. 356–367, 2008.

[66] Z. Yosibash, D. Tal, and N. Trabelsi, "Predicting the yield of the proximal femur using high-order finite-element analysis with inhomogeneous orthotropic material properties," *Philosophical Transactions of the Royal Society A*, vol. 368, no. 1920, pp. 2707–2723, 2010.

[67] W. Pistoia, B. van Rietbergen, E.-M. Lochmuller, C. Lill, F. Eckstein, and P. Ruegsegger, "Estimation of distal radius failure load with micro-finite element analysis models based on three-dimensional peripheral quantitative computed tomography images," *Bone*, vol. 30, no. 6, pp. 842–848, 2002.

[68] J. H. Keyak, S. A. Rossi, K. A. Jones, and H. B. Skinner, "Prediction of femoral fracture load using automated finite element modeling," *Journal of Biomechanics*, vol. 31, pp. 125–133, 1998.

[69] J. Keyak, "Improved prediction of proximal femoral fracture load using nonlin-

ear finite element models," *Medical Engineering & Physics*, vol. 23, pp. 165–173, 2001.

[70] M. M. Juszczyka, L. Cristofolini, and M. Viceconti, "The human proximal femur behaves linearly elastic up to failure under physiological loading conditions," *Journal of Biomechanics*, vol. 44, pp. 2259–2266, 2011.

[71] S. Poelert, E. Valstar, H. Weinans, and A. A. Zadpoor, "Patient-specific finite element modeling of bones," *Proceedings of the Institution of Mechanical Engineers, Part H: Journal of Engineering in Medicine*, vol. 227, no. 4, pp. 464–478, 2012.

[72] E. Basafa, R. S. Armiger, M. D. Kutzer, S. M. Belkoff, S. C. Mears, and M. Armand, "Patient-specific finite element modeling for femoral bone augmentation," *Medical Engineering & Physics*, vol. 35, no. 6, pp. 860–865, 2013.

[73] G. Dhondt, *The finite element method of three-dimensional thermomechanical applications*. Chichester, West Sussex, England: John Wiley & Sons Ltd., 2004.

[74] G. van Lenthe, J. van den Bergh, A. Hermus, and R. Huiskes, "The prospects of estimating trabecular bone tissue properties from the combination of ultrasound, dual-energy x-ray absorptiometry, microcomputed tomography, and microfinite element analysis," *Journal of Bone and Mineral Research*, vol. 16, no. 3, pp. 550–555, 2001.

[75] E. F. Morgan, H. H. Bayraktar, and T. M. Keaveny, "Trabecular bone modulus-density relationships depend on anatomic site," *Journal of Biomechanics*, vol. 36, pp. 897–904, 2003.

[76] T. S. Keller, "Predicting the compressive mechanical behavior of bone," *Journal of Biomechanics*, vol. 22, no. 9, pp. 1159–1168, 1994.

[77] Z. Yosibash, R. Padan, L. Joskowicz, and C. Milgram, "A CT-based high-order finite element analysis of the human proximal femur compared to in-vitro experiments," *Journal of Biomedical Engineering*, vol. 129, pp. 297–309, 2007.

[78] Z. Yosibash, N. Trabelsi, and C. Milgrom, "Reliable simulations of the human proximal femur by high-order finite element analysis validated by experimental observations," *Journal of Biomechanics*, vol. 40, pp. 3688–3699, 2007.

[79] D. O'Brien, D. Boyd, S. Madigan, and S. Murphy, "Evaluation of a novel radiopacifiying agent on the physical properties of surgical spineplex," *Journal of Materials Science: Materials in Medicine*, vol. 21, pp. 53–58, 2010.

[80] G. Lewis, "Properties of acrylic bone cement: State of the art review," *Journal of Biomedical Materials Research*, vol. 38, no. 2, pp. 155–182, 1997.

[81] L. Rohl, E. Larsen, F. Linde, A. Odgaard, and J. Jorgensen, "Tensile and compressive properties of cancellous bone," *Journal of Biomechanics*, vol. 24, pp. 1143–1149, 1991.

[82] D. L. Kopperdahl and T. M. Keaveny, "Yield strain behavior of trabecular bone," *Journal of Biomechanics*, vol. 31, pp. 601–608, 1998.

[83] J. H. Keyak, H. B. Skinner, and J. A. Fleming, "Effect of force direction on femoral fracture load for two types of loading conditions," *Journal of Orthopaedic Research*, vol. 19, pp. 539–544, 2001.

[84] C. Ford, T. Keaveny, and W. Hayes, "The effect of impact direction on the structural capacity of the proximal femur during falls," *Journal of Bone and Mineral Research*, vol. 11, pp. 377–383, 1996.

[85] M. Bessho, I. Ohnishi, J. Matsuyama, T. Matsumoto, K. Imai, and K. Nakamura, "Prediction of strength and strain of the proximal femur by a CT-based finite element method," *Journal of Biomechanics*, vol. 40, pp. 1745–1753, 2007.

[86] R. Wilcox, "The biomechanics of vertebroplasty: A review," in *Proceedings of the Institution of Mechanical Engineers*, ser. Journal of Engineering in Medicine, vol. 218, no. 1, 2004, pp. 1–10.

[87] J. Luo, M. A. Adams, and P. Dolan, "Vertebroplasty and kyphoplasty can restore normal spine mechanics following osteoporotic vertebral fracture," *Journal of Osteoporosis*, vol. 2010, no. 2042-0064(Electronic), 2010.

[88] A. C. Jones, V. N. Wijayathunga, S. Rehman, and R. K. Wilcox, "Subject-specific models of the spine for the analysis of vertebroplasty," in *Patient-*

Specific Modeling in Tomorrow's Medicine, ser. Studies in Mechanobiology, Tissue Engineering and Biomaterials, A. Gefen, Ed. Springer Berlin Heidelberg, 2012, vol. 09, pp. 133–154.

[89] C. E. Tschirhart, J. A. Finkelstein, and C. M. Whyne, "Optimization of tumor volume reduction and cement augmentation in percutaneous vertebroplasty for prophylactic treatment of spinal metastases," *Journal of Spinal Disorders & Techniques*, vol. 19, no. 8, pp. 584–590, 2006.

[90] S. Belkoff, M. Maroney, D. Fenton, and J. Mathis, "An in vitro biomechanical evaluation of bone cements used in percutaneous vertebroplasty," *Bone*, vol. 25, no. 2, Supplement 1, pp. 23S–26S, 1999.

[91] Y. Xie and G. Steven, "A simple evolutionary procedure for structural optimization," *Computers & Structures*, vol. 49, pp. 885–896, 1993.

[92] O. Querin, G. Steven, and Y. Xie, "Evolutionary structural optimisation using an additive algorithm," *Finite Elements in Analysis and Design*, vol. 34, pp. 291–308, 2000.

[93] O. Querin, G. Steven, and Y. Xie, "Evolutionary structural optimisation (ESO) using a bidirectional algorithm," *Engineering Computations*, vol. 15, pp. 1031–1048, 1998.

[94] V. Young, O. Querin, and G. Steven, "3D and multiple load case bi-directional

evolutionary optimization (BESO)," *Structural Optimization*, vol. 18, pp. 183–192, 1999.

[95] P. Tanskanen, "The evolutionary structural optimization method: theoretical aspects," *Computer Methods in Applied Mechanics and Engineering*, vol. 191, pp. 5485–5498, 2002.

[96] D. N. Chu, Y. Xie, A. Hira, and G. Steven, "Evolutionary structural optimization for problems with stiffness constraints," *Finite Element Analysis and Design*, vol. 21, pp. 239–251, 1996.

[97] E. Basafa and M. Armand, "Cement placement optimization in femoral augmentation using an evolutionary algorithm," in *Proceedings of the ASME International Design Engineering Technical Conferences and Computers and Information in Engineering Conference (IDETC/CIE2013)*, ser. 2013 ASME/IEEE International Conference on Mechatronic and Embedded Systems and Applications, Parts A and B, 2013.

[98] J. Parkkari, P. Kannus, M. Palvanen, A. Natri, J. Vainio, H. Aho, I. Vuori, and M. Jarvinen, "Majority of hip fractures occur as a result of a fall and impact on the greater trochanter of the femur: A prospective controlled hip fracture study with 206 consecutive patients," *Calcified Tissue International*, vol. 65, pp. 183–187, 1999.

[99] T. Pinilla, K. Boardman, M. Bouxsein, E. Myers, and W. Hayes, "Impact

direction from a fall influences the failure load of the proximal femur as much as age-related bone loss," *Calcified Tissue International*, vol. 58, pp. 231–235, 1996.

[100] A. Courtney, E. Wachtel, E. Myers, and W. Hayes, "Age-related reductions in the strength of the femur tested in a fall-loading configuration," *The Journal of Bone & Joint Surgery*, vol. 77, pp. 387–395, 1995.

[101] J. Parkkari, P. Kannus, J. Heikkila, J. Poutala, A. Heinonen, H. Sievanen, and I. Vuori, "Impact experiments of an external hip protector in young volunteers," *Calcified Tissue International*, vol. 60, pp. 354–357, 1997.

[102] P. Kannus, J. Parkkari, and J. Poutala, "Comparison of force attenuation properties of four different hip protectors under simulated falling conditions in the elderly: An in vitro biomechanical study," *Bone*, vol. 25, pp. 229–235, 1999.

[103] M. Loeffel, S. J. Ferguson, L.-P. Nolte, and J. H. Kowal, "Experimental characterization of polymethylmethacrylate bone cement spreading as a function of viscosity, bone porosity, and flow rate," *Spine*, vol. 33, pp. 1352–1359, 2008.

[104] A. Beaudoin, W. Mihalko, and W. Krause, "Finite element modelling of polymethylmethacrylate flow through cancellous bone," *Journal of Biomechanics*, vol. 24, pp. 127–136, 1991.

[105] G. Baroud and F. Yahia, "A finite element rheological model for polymethyl-

methacrylate flow: analysis of the cement delivery in vertebroplasty," in *Proceedings of the Institution of Mechanical Engineers*, ser. Journal of Engineering in Medicine, vol. 218, no. 1, 2004, pp. 331–338.

[106] M. Bohner, B. Gasser, G. Baroud, and P. Heini, "Theoretical and experimental model to describe the injection of a polymethylmethacrylate cement into a porous structure," *Biomaterials*, vol. 24, pp. 2721–2730, 2003.

[107] Z. Lian, C. Chui, and S. Teoh, "A biomechanical model for real-time simulation of PMMA injection with haptics," *Computers in Biology and Medicine*, vol. 38, pp. 304–312, 2008.

[108] M. Liu, J. Chang, and H. Li, "Numerical modeling of injection flow of drug agents for controlled drug delivery," in *Engineering in Medicine and Biology Society, 2007. EMBS 2007. 29th Annual International Conference of the IEEE*, August 2007, pp. 1152–1155.

[109] S. Clavet, P. Beaudoin, and P. Poulin, "Particle-based viscoelastic fluid simulation," in *Proceedings of the 2005 ACM SIGGRAPH/Eurographics symposium on Computer animation*, ser. SCA '05. New York, NY, USA: ACM, 2005, pp. 219–228.

[110] Y. Zhu and R. Bridson, "Animating sand as a fluid," in *ACM SIGGRAPH 2005 Papers*, ser. SIGGRAPH '05. New York, NY, USA: ACM, 2005, pp. 965–972.

[111] K. Steele, D. Cline, P. K. Egbert, and J. Dinerstein, "Modeling and rendering viscous liquids," *Computer Animation and Virtual Worlds*, vol. 15, pp. 183–192, 2004.

[112] L. Lucy, "A numerical approach to the testing of the fission hypothesis," *Astronomical Journal*, vol. 82, pp. 1013–1024, 1977.

[113] R. Gingold and J. Monaghan, "Smoothed particle hydrodynamics - theory and application to non-spherical stars," *Monthly Notices of the Royal Astronomical Society*, vol. 181, pp. 375–389, 1977.

[114] M. Muller, D. Charypar, and M. Gross, "Particle-based fluid simulation for interactive applications," in *Proceedings of the 2003 ACM SIGGRAPH/Eurographics symposium on Computer animation*, ser. SCA '03. Eurographics Association, 2003, pp. 154–159.

[115] M. Becker and M. Teschner, "Weakly compressible SPH for free surface flows," in *Proceedings of the 2007 ACM SIGGRAPH/Eurographics symposium on Computer animation*, ser. SCA '07. Aire-la-Ville, Switzerland, Switzerland: Eurographics Association, 2007, pp. 209–217.

[116] A. Paiva, F. Petronetto, T. Lewiner, and G. Tavares, "Particle-based non-newtonian fluid animation for melting objects," in *Computer Graphics and Image Processing, 2006. SIBGRAPI '06. 19th Brazilian Symposium on*, October 2006, pp. 78–85.

[117] A. Paiva, F. Petronetto, T. Lewiner, and G. Tavares, "Particle-based viscoplastic fluid/solid simulation," *Computer-Aided Design*, vol. 41, pp. 306–314, 2009.

[118] T. Lenaerts, B. Adams, and P. Dutre, "Porous flow in particle-based fluid simulations," in *ACM SIGGRAPH 2008 papers*, ser. SIGGRAPH '08. New York, NY, USA: ACM, 2008, pp. 49:1–49:8.

[119] S. Ovaysi and M. Piri, "Direct pore-level modeling of incompressible fluid flow in porous media," *Journal of Computational Physics*, vol. 229, pp. 7456–7476, 2010.

[120] D. W. Holmes, J. R. Williams, , and P. Tilke, "Smooth particle hydrodynamics simulations of low reynolds number flows through porous media," *International Journal for Numerical and Analytical Methods in Geomechanics*, vol. 35, pp. 419–437, 2011.

[121] G. Pereira, M. Prakash, and P. Cleary, "SPH modelling of fluid at the grain level in a porous medium," *Applied Mathematical Modelling*, vol. 35, pp. 1666–1675, 2011.

[122] E. Basafa, R. Murphy, M. Kutzer, Y. Otake, and M. Armand, "A particle model for prediction of cement infiltration of cancellous bone in osteoporotic bone augmentation," *PLoS One*, vol. 8, no. 6, p. e67958, 2013.

[123] D. Pnueli and C. Gutfinger, *Fluid Mechanics*. New York: Cambridge University Press, 1997.

[124] J. Monaghan, "Smoothed particle hydrodynamics," *Annual Review of Astronomy and Astrophysics*, vol. 30, pp. 543–574, 1992.

[125] Z. Zhong, L. Chen, H. Cai, and Y. Cao, "Realistic simulation of multi-scale fluid-solid coupling," in *Computer-Aided Industrial Design and Conceptual Design, 2008. CAID/CD 2008. 9th International Conference on*, November 2008, pp. 523–528.

[126] Y. Zhu, P. Fox, and J. Morris, "A pore-scale numerical model for flow through porous media," *International Journal for Numerical and Analytical Methods in Geomechanics*, vol. 23, pp. 881–904, 1999.

[127] F. Jiang, M. S. Oliveira, and A. C. Sousa, "Mesoscale SPH modeling of fluid flow in isotropic porous media," *Computer Physics Communications*, vol. 176, pp. 471–480, 2007.

[128] A. M. Tartakovsky, P. Meakin, T. D. Scheibe, and B. D. Wood, "A smoothed particle hydrodynamics model for reactive transport and mineral precipitation in porous and fractured porous media," *Water Resources Research*, vol. 43, 2007.

[129] J. P. Morris, P. J. Fox, and Y. Zhu, "Modeling low Reynolds number incom-

pressible flows using SPH," *Journal of Computational Physics*, vol. 136, pp. 214–226, 1997.

[130] S. Shao and E. Y. Lo, "Incompressible SPH method for simulating newtonian and non-newtonian flows with a free surface," *Advances in Water Resources*, vol. 26, pp. 787–800, 2003.

[131] G. Baroud, J. Wu, M. Bohner, S. Sponagel, and T. Steffen, "How to determine the permeability for cement infiltration of osteoporotic cancellous bone," *Medical Engineering & Physics*, vol. 25, pp. 283–288, 2003.

[132] P. Randles and L. Libersky, "Smoothed particle hydrodynamics: Some recent improvements and applications," *Computer Methods in Applied Mechanics and Engineering*, vol. 139, pp. 375–408, 1996.

[133] M. Desbrun and M.-P. Gascuel, "Smoothed particles: A new paradigm for animating highly deformable bodies," in *In Computer Animation and Simulation 96 (Proceedings of EG Workshop on Animation and Simulation.* Springer-Verlag, 1996, pp. 61–76.

[134] M. D. Kutzer, E. Basafa, Y. Otake, and M. Armand, "An automatic injection device for precise cement delivery during osteoporotic bone augmentation," in *Proceedings of the ASME International Design Engineering Technical Conferences and Computers and Information in Engineering Conference*

(IDETC/CIE2011), ser. 2011 ASME/IEEE International Conference on Mechatronic and Embedded Systems and Applications, Parts A and B, vol. 3, 2011, pp. 821–827.

[135] Y. Otake, M. Armand, O. Sadowsky, M. Kutzer, R. Armiger, E. Basafa, P. Kazanzides, and R. Taylor, "Development of a navigation system for femoral augmentation using an intraoperative C-arm reconstruction," in *Proceedings of the 9th Annual Meeting of CAOS-International*, 2009, pp. 177–180.

[136] S. Saha and S. Pal, "Mechanical properties of bone cement: A review," *Journal of Biomedical Materials Research*, vol. 18, pp. 435–462, 1984.

[137] B. Lucas, Y. Otake, M. Armand, and R. Taylor, "An active contour method for bone cement reconstruction from C-arm X-ray images," *IEEE Transactions on Medical Imaging*, vol. 31, no. 4, pp. 860–869, april 2012.

[138] A. Koponen, M. Kataja, and J. Timonen, "Permeability and effective porosity of porous media," *Physical Review E*, vol. 56, pp. 3319–3325, 1997.

[139] A. C. Sousa, , and F. Jiang, "SPH as an inverse numerical tool for the prediction of diffusive properties in porous media," *Materials Science Forum*, vol. 553, pp. 171–189, 2007.

[140] J. Bryant, T. David, P. Gaskell, S. King, and G. Lond, "Rheology of bovine

bone marrow," *Proceedings of the Institution of Mechanical Engineers, Part H: Journal of Engineering in Medicine*, vol. 203, no. 2, pp. 71–75, 1989.

[141] Z. Zhong and O. Akkus, "Effects of age and shear rate on the rheological properties of human yellow bone marrow," *Biorheology*, vol. 48, pp. 89–97, 2011.

[142] A. Ferrari, M. Dumbser, E. F. Toro, and A. Armanini, "A new parallel SPH method for 3D free surface flows," in *High Performance Computing on Vector Systems 2009*, M. Resch, S. Roller, K. Benkert, M. Galle, W. Bez, and H. Kobayashi, Eds. Springer Berlin Heidelberg, 2010, pp. 179–188.

[143] E. Basafa, R. Murphy, M. Kutzer, Y. Otake, and M. Armand, "Computer assisted femoral augmentation—modeling and experimental validation," in *Proceedings of the ASME International Design Engineering Technical Conferences and Computers and Information in Engineering Conference (IDETC/CIE2013)*, ser. 2013 ASME/IEEE International Conference on Mechatronic and Embedded Systems and Applications, Parts A and B, 2013.

[144] M. Kutzer, S. Segreti, C. Brown, M. Armand, R. Taylor, and S. Mears, "Design of a new cable-driven manipulator with a large open lumen: Preliminary applications in the minimally-invasive removal of osteolysis," in *Robotics and Automation (ICRA), 2011 IEEE International Conference on*, 2011, pp. 2913–2920.

[145] P. Besl and N. McKay, "A method for registration of 3-D shapes," *IEEE Trans-*

actions on Pattern Analysis and Machine Intelligence, vol. 14, no. 2, pp. 239–256, 1992.

[146] S. Pieper, W. Lorensen, W. Schroeder, and R. Kikinis, "The NA-MIC kit: ITK, VTK, Pipelines, Grids and 3D Slicer as an open platform for the medical image computing community," in *Proceedings of the IEEE International Symposium on Biomedical Imaging*, 2006, pp. 698–701.

[147] Y. Otake, M. Armand, R. S. Armiger, M. Kutzer, E. Basafa, P. Kazanzides, and R. Taylor, "Intraoperative image-based multiview 2D/3D registration for image-guided orthopaedic surgery: Incorporation of fiducial-based C-arm tracking and GPU-acceleration," *IEEE Transactions on Medical Imaging*, vol. 31, no. 4, pp. 948–962, 2012.

[148] J. Okrajni, M. Plaza, and S. Ziemba, "Computer modelling of the heat flow in surgical cement during endoprosthesoplasty," *Journal of Achievements in Materials and Manufacturing Engineering*, vol. 20, pp. 311–314, 2007.

[149] M. Stanczyk, "Study on modelling of PMMA bone cement polymerisation," *Journal of Biomechanics*, vol. 38, pp. 1397–1403, 2005.

[150] M. Stanczyk and J. Telega, "Modelling of heat transfer in biomechanics - a review. Part II. orthopaedics," *Acta of Bioengineering and Biomechanics*, vol. 4, no. 2, pp. 3–31, 2002.

Vita

Ehsan Basafa received his B.Sc. in Mechanical Engineering and M.Sc. in Biomedical Engineering - Biomechanics from Sharif University of Technology, Tehran, Iran in 2005 and 2008, respectively. He then entered the Ph.D. program of Mechanical Engineering at Johns Hopkins University in the fall of 2008. His research interests include computer-assisted surgery, biomechanics, robotics, surgical simulation, and haptics. In 2011 he was nominated by Johns Hopkins University for the Howard Hughes Medical Institute's International Student Research Fellowship award and in 2013 he received the Creel Family Teaching Assistant award of Mechanical Engineering from Johns Hopkins University.

Following graduation, he will continue research in the area of computer-assisted orthopaedic surgery and robotics at the Laboratory for Computational Sensing & Robotics (LCSR) of Johns Hopkins University.